

Recent progress in perovskite solar cells: from device to commercialization

Xinhui Luo¹, Xuesong Lin¹, Feng Gao², Yang Zhao³, Xiaodong Li⁴, Liqing Zhan⁵,
Zexiong Qiu⁶, Jin Wang⁷, Cong Chen⁸, Lei Meng^{9*}, Xiaofeng Gao¹⁰, Yu Zhang¹¹,
Zijian Huang¹¹, Rundong Fan¹¹, Huifen Liu¹¹, Yanrun Chen¹¹, Xiaoxue Ren¹², Jiahong Tang¹³,
Chun-Hao Chen¹⁴, Dong Yang¹⁵, Yongguang Tu¹⁶, Xiao Liu^{18*}, Dongxue Liu^{19*}, Qing Zhao^{2*},
Jingbi You^{3*}, Junfeng Fang^{4*}, Yongzhen Wu^{5*}, Hongwei Han^{6*}, Xiaodan Zhang^{7*},
Dewei Zhao^{8*}, Fuzhi Huang^{10*}, Huanping Zhou^{11*}, Yongbo Yuan^{12*}, Qi Chen^{13*},
Zhaokui Wang^{14*}, Shengzhong (Frank) Liu^{15*}, Rui Zhu^{17*}, Jotaro Nakazaki²⁰,
Yongfang Li⁹ & Liyuan Han^{1*}

¹State Key Laboratory of Metal Matrix Composites, School of Material Science and Engineering, Shanghai Jiao Tong University, Shanghai 200240, China;

²State Key Lab for Mesoscopic Physics and Frontiers Science Center for Nano-optoelectronics, School of Physics, Peking University, Beijing 100871, China;

³Key Laboratory of Semiconductor Materials Science, Institute of Semiconductors, Chinese Academy of Sciences, Beijing 100083, China;

⁴School of Physics and Electronic Science, Engineering Research Center of Nanophotonics & Advanced Instrument, Ministry of Education, East China Normal University, Shanghai 200241, China;

⁵Key Laboratory for Advanced Materials and Institute of Fine Chemicals, School of Chemistry and Molecular Engineering, East China University of Science and Technology, Shanghai 200237, China;

⁶Wuhan National Laboratory for Optoelectronics, Huazhong University of Science and Technology, Wuhan 430074, China;

⁷Institute of Photoelectronic Thin Film Devices and Technology, Renewable Energy Conversion and Storage Center, Solar Energy Research Center, Nankai University, Tianjin 300350, China;

⁸College of Materials Science and Engineering & Engineering Research Center of Alternative Energy Materials & Devices, Ministry of Education, Sichuan University, Chengdu 610065, China;

⁹Beijing National Laboratory for Molecular Sciences, CAS Key Laboratory of Organic Solids, Institute of Chemistry, Chinese Academy of Sciences, Beijing 100190, China;

¹⁰State Key Laboratory of Advanced Technology for Materials Synthesis and Processing, Wuhan University of Technology, Wuhan 430070, China;

¹¹Beijing Key Laboratory for Theory and Technology of Advanced Battery Materials, Key Laboratory of Polymer Chemistry and Physics of Ministry of Education, School of Materials Science and Engineering, Peking University, Beijing 100871, China;

¹²School of Physics and Electronics, Hunan Key Laboratory of Nanophotonics and Devices, Central South University, Changsha 410083, China;

¹³Experimental Center for Advanced Materials, School of Materials Science and Engineering, Beijing Institute of Technology, Beijing 100081, China;

¹⁴Jiangsu Key Laboratory for Carbon-Based Functional Materials & Devices, Institute of Functional Nano & Soft Materials (FUNSOM), Soochow University, Suzhou 215123, China;

¹⁵Dalian National Laboratory for Clean Energy; iChEM, Dalian Institute of Chemical Physics, Chinese Academy of Sciences, Dalian 116023, China;

*Corresponding authors (email: han.liyuan@sjtu.edu.cn; zhaoping@pku.edu.cn; jyou@semi.ac.cn; jffang@phy.ecnu.edu.cn; wu.yongzhen@ecust.edu.cn; hongwei.han@mail.hust.edu.cn; xdzhang@nankai.edu.cn; dewei.zhao@scu.edu.cn; menglei@iccas.ac.cn; fuzhi.huang@whut.edu.cn; happy_zhou@pku.edu.cn; yuanyb@csu.edu.cn; qic@bit.edu.cn; zkwang@suda.edu.cn; szliu@dicp.ac.cn; iamzhurui@pku.edu.cn; liu_dongxue@ctg.com.cn; liu.xiao@mail.u-tokyo.ac.jp)

¹⁶Frontiers Science Center for Flexible Electronics, Xi'an Institute of Flexible Electronics (IFE) & Xi'an Institute of Biomedical Materials and Engineering, Northwestern Polytechnical University, Shaanxi 710072, China;

¹⁷State Key Laboratory for Artificial Microstructure and Mesoscopic Physics, School of Physics, Frontiers Science Center for Nano-optoelectronics & Collaborative Innovation Center of Quantum Matter, Peking University, Beijing 100871, China;

¹⁸Special Division of Environmental and Energy Science, Komaba Organization for Educational Excellence (KOMEX), College of Arts and Sciences, The University of Tokyo, Tokyo 153-8902, Japan;

¹⁹China Three Gorges Corporation, Institute of Science and Technology, Beijing 100038, China;

²⁰Research Center for Advanced Science and Technology (RCAST), The University of Tokyo, Tokyo 153-8904, Japan

Received September 13, 2022; accepted October 12, 2022; published online November 3, 2022

Perovskite solar cells (PSCs) are undergoing rapid development and the power conversion efficiency reaches 25.7% which attracts increasing attention on their commercialization recently. In this review, we summarized the recent progress of PSCs based on device structures, perovskite-based tandem cells, large-area modules, stability, applications and industrialization. Last, the challenges and perspectives are discussed, aiming at providing a thrust for the commercialization of PSCs in the near future.

perovskite solar cells, device engineering, stability, application

Citation: Luo X, Lin X, Gao F, Zhao Y, Li X, Zhan L, Qiu Z, Wang J, Chen C, Meng L, Gao X, Zhang Y, Huang Z, Fan R, Liu H, Chen Y, Ren X, Tang J, Chen CH, Yang D, Tu Y, Liu X, Liu D, Zhao Q, You J, Fang J, Wu Y, Han H, Zhang X, Zhao D, Huang F, Zhou H, Yuan Y, Chen Q, Wang Z, Liu S, Zhu R, Nakazaki J, Li Y, Han L. Recent progress in perovskite solar cells: from device to commercialization. *Sci China Chem*, 2022, 65: 2369–2416, <https://doi.org/10.1007/s11426-022-1426-x>

CONTENTS

1 Introduction	2371	5.1.1 Absorbers	2395
2 Device categories	2371	5.1.2 Passivators	2396
2.1 PSCs with n-i-p structure	2371	5.1.3 Carrier transport materials	2396
2.1.1 Perovskite layer	2372	5.1.4 Electrodes	2398
2.1.2 Interface	2374	5.2 Ion migration	2398
2.2 PSCs with p-i-n structure	2377	5.2.1 Irreversible performance decay	2398
2.2.1 Perovskite layer	2378	5.2.2 Interplay between ion migration and other decay mechanisms	2399
2.2.2 Interface	2378	5.3 Encapsulation	2400
2.3 Printable mesoscopic PSCs	2381	6 Application	2401
3 Tandems	2383	6.1 Indoor applications	2401
3.1 Perovskite/c-Si tandem solar cells	2383	6.1.1 Superiorities of PIPVs	2401
3.1.1 Spin coating	2383	6.1.2 Precise measurement of IPVVs	2402
3.1.2 Vacuum-based deposition	2385	6.1.3 Developments and opportunities of PIPVs	2402
3.1.3 Other deposition methods	2385	6.2 Flexible applications	2402
3.2 Perovskite/CIGS tandem solar cells	2386	6.2.1 Flexible transparent conductive electrodes	2403
3.3 All-perovskite tandem solar cells	2386	6.2.2 Flexible opaque electrodes	2404
3.3.1 Wide- E_g perovskite top subcells	2386	6.3 Space applications	2404
3.3.2 Low- E_g perovskite bottom subcells	2387	6.3.1 Extreme environment in space and specific requirements for space photovoltaics	2404
3.3.3 ICLs for all-perovskite TSCs	2387	6.3.2 Radiation resistance of PSCs	2404
3.3.4 All-perovskite TSCs	2388	6.3.3 Space flight experiments of PSCs	2405
3.4 Perovskite/organic tandem	2389	7 Industrialization	2406
4 Modules	2390	7.1 In Japan	2406
4.1 Large-area function layers deposition	2390	7.2 In China	2406
4.1.1 Perovskite layers	2390	7.3 In Europe	2406
4.1.2 ETL, HTL and electrodes	2392	7.4 Other countries	2407
4.2 Modules design and process	2394	8 Perspectives	2407
5 Stability	2395		
5.1 Functional layers	2395		

1 Introduction

Organic-inorganic hybrid perovskite solar cells (PSCs) have prompted a surge of research in academia and industry in recent years because of their ever-increasing efficiency, solution fabrication process, and low cost of raw materials. There are several device architectures of PSCs, as shown in Figure 1, including mesoporous structure, planar structure and inverted structure. Since the mesoporous PSC was derived from the dye-sensitized solar cells [1–3], it consists of a transparent electrode, a dense TiO_2 layer, a mesoporous TiO_2 layer, a perovskite layer, a hole transport layer, and a rear electrode (Figure 1b). When the mesoporous layer was removed, it becomes a planar structure (Figure 1c). The devices adopted these two configurations are called normal structural devices (n-i-p), and their mechanism of power generation is similar. The electrons and holes formed in the perovskite crystals under light illumination, and are respectively injected into the electron and the hole transport layer and move to the electrode to generate power.

On the other hand, an inverted structure (p-i-n) was proposed in reference to organic solar cells [4]. The inverted structure is composed of a transparent electrode, a hole transport layer (HTL), a perovskite layer, an electron transport layer (ETL), and a rear electrode on top, as shown in Figure 1d. The structure is analogous to that of organic thin-film solar cells, while the direction of electrons and holes is opposite to the normal ones and thus defined as the inverted structure. In the early stage, mesoporous structures were well studied. The normal structure is well studied because of its high efficiency, while research on inverted PSCs has been increasing in recent years due to their advantage of stability.

To further improve the power conversion efficiency (PCE) from the view of device engineering, exploiting various types of tandem devices to reduce the loss of excess kinetic energy and break the S-Q limit of single-junction cells is becoming the spotlight. The efficiency of perovskite/Si tandem devices is over 30% and the perovskite/perovskite tandem solar cells reaches 28%, with the development of the fabrication process, wide and narrow band gap perovskites and interconnecting layer [2,3]. In the meantime, up-scaling cell to module is an important task to promote the commercialization of PSCs. A mini-module with PCE of over 21% has been achieved [2,5], and a large module with $>800\text{ cm}^2$ showed a PCE of 17.9%. Besides efficiency, stability has also achieved a remarkable breakthrough recently [2]. By suppressing ion migration and increasing the robustness of perovskite absorbers, the small device of PSCs passed maximum power point (MPP) tracking for more than 9,000-h [6]. Perovskite mini-module passed the heating and moisture aging test, and MPP tracking for 1,000 h [7]. These advancements have so far demonstrated the promising potential

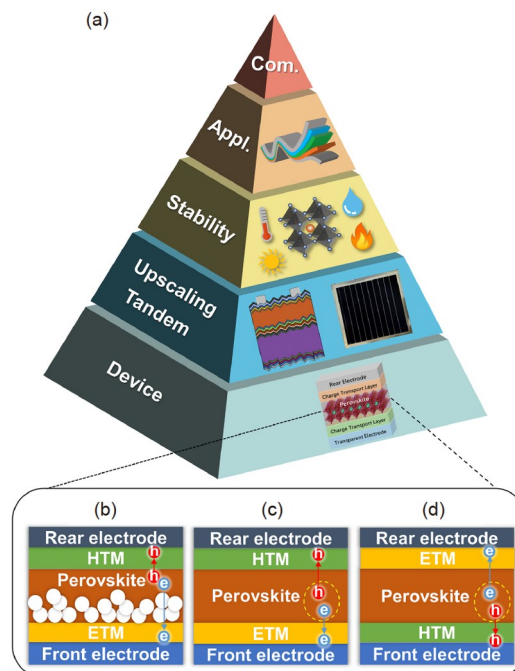


Figure 1 (a) Development route of PSCs: from device to commercialization. Schematic of device architectures (b) mesoporous PSCs, (c) planar structure, (d) inverted structure. Note that the applications and commercialization are abbreviated as Appl. and Com., respectively (color online).

of PSCs in diverse scenarios, including indoor photovoltaic, flexible/wearable devices, see-through devices, and outer space applications.

In this review, we summarize the recent development of PSCs in the last 5 years. As depicted in Figure 1a, this review is composed of the following contents: (1) device structure mainly including conventional and inverted structures; (2) the tandem structure of perovskite/silicon, perovskite/perovskite and perovskite/organic photovoltaic (OPV), (3) up-scaling to modules, (4) the stability issues in the perovskite in each functional layer, ion migration and encapsulation, (5) the potential application scenarios such as indoor photovoltaic (PV), flexible electronic and out-space application, (6) brief introduction of the current progress of perovskite industrialization. Finally, according to the current progress and existing problems, we share our perspective on most concerned issues in PSCs, in hope of giving some inspiration for the further development of PSCs.

2 Device categories

In this section, we will introduce the recent progress of the normal (n-i-p) and inverted (p-i-n) structure. In addition, we also introduce the carbon electrode-based structure which is derived from the n-i-p structure that can be fabricated by the all-printable method.

2.1 PSCs with n-i-p structure

2.1.1 Perovskite layer

(1) Seeding induced growth

As the light-absorbing layer, the crystal quality of the perovskite film largely dominates the photovoltaic performance of the solar cell device. Perovskite films are usually fabricated by solution spin-coating (including one-step and two-step methods), which often results in polycrystalline films. Therefore, the control of film morphology, including grain size, distribution, and voiding, is critical to crystal quality [8]. After years of development, the two-step method has gradually become a more favored method for the preparation of perovskite films due to its easier control of experimental conditions and relatively excellent reproducibility [9–13].

To better control film formation of the two-step method and improve film quality, Zhao *et al.* [14] proposed seeding induced growth method. Different from the traditional two-step deposition process, they first deposited PbI_2 film with submicron-sized Cs-containing perovskite seeds and then introduced mixed organic halide salts atop it. The seeds promote the reaction of the organic ammonium salts with PbI_2 during diffusion, which act as nuclei for the subsequent growth of the perovskite film (Figure 2a). When the organic salt was added dropwise onto the PbI_2 layer, the perovskite crystallization process started rapidly. Two crystal-growth-kinetic modes are manifested. One is random nucleation growth (red dashed circles) and the other is perovskite seed-assisted growth (white circles, Figure 2b, middle). It is clear that the rate of perovskite seed-assisted growth (PSG) is faster than random nucleation, thereby dominating the entire crystallization process (Figure 2b, right). Note that the grain

size can be finely tuned by the seed concentration and therefore the nucleation density. In this way, crystallization dynamics, grain size, and perovskite composition can be well controlled through the PSG method. Therefore, a PCE of 21.5% and better operational stability have been achieved.

To further increase the doping amount of cesium cations, Li *et al.* [13] developed a CsCl-enhanced PbI_2 precursor method. *In situ* confocal microscopy imaging showed that the introduced chloride successfully reduced the nucleation density and retarded the formation of perovskite (Figure 2c), resulting in a nearly two-fold increase in perovskite grain size and better film quality. Subsequently, a bromine-rich seed growth method was devised to alter perovskite seed composition and seed concentration by halogen engineering [15]. The bromine-rich seeds further expanded the perovskite grain size to 1.5 μm , exhibiting much more vertically columnar through-grains. Finally, the “bromine-rich” device exhibited excellent operational stability, maintaining over 80% of the initial PCE after 500 h of MPP tracking. Inspired by the above strategy, a series of all-inorganic perovskite seed crystals have also been developed, including $\delta\text{-CsPbI}_3$, CsPbBr_3 and RbPbI_3 [16–19]. Perovskite seeds have been shown to not only act as nucleation sites to regulate crystal growth, but also serve as stabilizers for formamidinium lead iodide (FAPbI_3) black phase [16,17]. Additionally, a pre-deposited perovskite array was also used as a template to induce a bottom-up crystallization (Figure 2d). The average grain size was $>3 \mu\text{m}$, contributing to PCEs of 25.1% [20].

Two-dimensional (2D) perovskites, in which the organic layer acts as a protective barrier to prevent moisture, have recently attracted increasing attention because of their significant robustness [21]. To take advantage of this feature, Luo *et al.* [22] introduced highly oriented two-dimensional

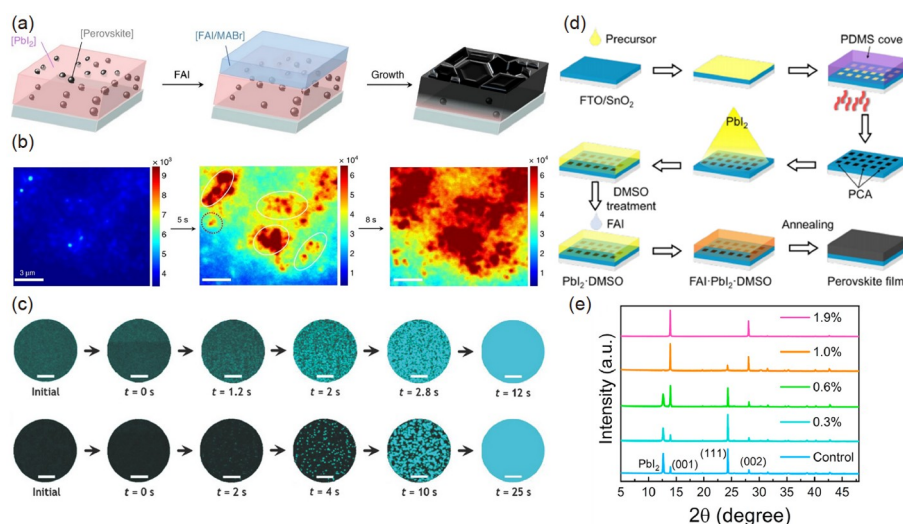


Figure 2 (a) Schematic of fabrication procedure of perovskite films using PSG [14]. (b) *In situ* PL microscopy reports real-time growth of perovskite from PSG [14]. (c) *In situ* perovskite growing process by CLSM for CsCl-enhanced PbI_2 precursor method. Scale bar: 10 μm [13]. (d) Schematic of fabrication procedure of perovskite crystal-array-assisted growth [20]. (e) X-ray diffraction patterns of perovskite films with varied seed concentrations [22] (color online).

Dion-Jacobson (2D DJ) phase perovskites as templates for the heteroepitaxial growth of 3D perovskite with the desired facet orientation and stacking mode. In this way, PSG provides a new feature: tailoring facet orientation for 3D perovskite *via* highly oriented 2D perovskite. As characterized by X-ray diffraction, the (001) and (002) facet orientations of 3D perovskite are significantly promoted with increasing 2D seed concentration, while the undesired (111) facet orientation and PbI_2 signals are suppressed (Figure 2e). Ultimately, the perovskite film exhibited a preferred orientation of the (001) family of planes with larger crystal grains. Interestingly, the 2D phase is distributed at the grain boundary of the 3D perovskite after the crystal growth process, resulting in band bending at the grain boundary to inhibit interface non-radiative recombination of carriers. The high-quality perovskite films resulted in an overall improvement in photovoltaic performance and stability, with a PCE of 23.95% and an ultrahigh *FF* of 0.847.

(2) Intermediate phase engineering

Perovskite films are typically prepared using a simple solution process such as spin coating in the lab. The technique of the solution process could usually be roughly divided into three steps: precursor, intermediate phase, and nucleation crystal growth. The precursor solutions often consist of PbI_2 (and organic salts in the one-step method) and polar solvents, among which the most commonly used solvents are dimethylformamide (DMF) and dimethyl sulfoxide (DMSO) [23]. Due to the strong coordination ability between polar solvents and PbI_2 , a relatively stable intermediate phase, such as $\text{PbI}_2\text{-DMSO-MA(FA)I}$, can be generated [24].

The intermediate phase directly affects the crystallization rate and crystal growth direction, so it is considered to be the key stage for the growth of high-quality FAPbI_3 perovskite films [24–26].

In 2021, Hui *et al.* [23] chose a common ionic liquid methylamine formate (MAFa) as the solvent for PbI_2 . PbI_2 dissolved in DMF:DMSO forms needle-like surface morphology after annealing, which provides multiple nucleation sites, causing the grains to shrink during growth and forming undesirable pinholes. On the contrary, MAFa as a solvent promotes the formation of uniform morphology and PbI_2 grains larger than $1\ \mu\text{m}$, laying the foundation for the subsequent vertical growth of perovskite grains. Through the strong interaction of C=O/Pb chelation and N-H/I hydrogen bonding with PbI_2 , MAFa not only promotes the vertical growth of PbI_2 relative to the substrate, but also inhibits the oxidation of iodide ions (Figure 3a). Therefore, PSCs with efficiencies as high as 24.1% were fabricated under the conditions of room temperature and high humidity, paving the way for industrial production. Ingeniously, Li *et al.* [27] developed liquid medium-assisted annealing to achieve uniform heating of perovskite films in all directions, blocking impurities in the atmosphere from affecting the crystallization process, and laying the foundation for all-weather repeatable industrialization.

In addition, some important developments have also been made in the study of the intermediate phase for the one-step method. In 2022, Wang *et al.* [28] introduced a green anti-solvent isobutanol (IBA) in a one-step method, which effectively inhibited the formation of δ -phase perovskite by

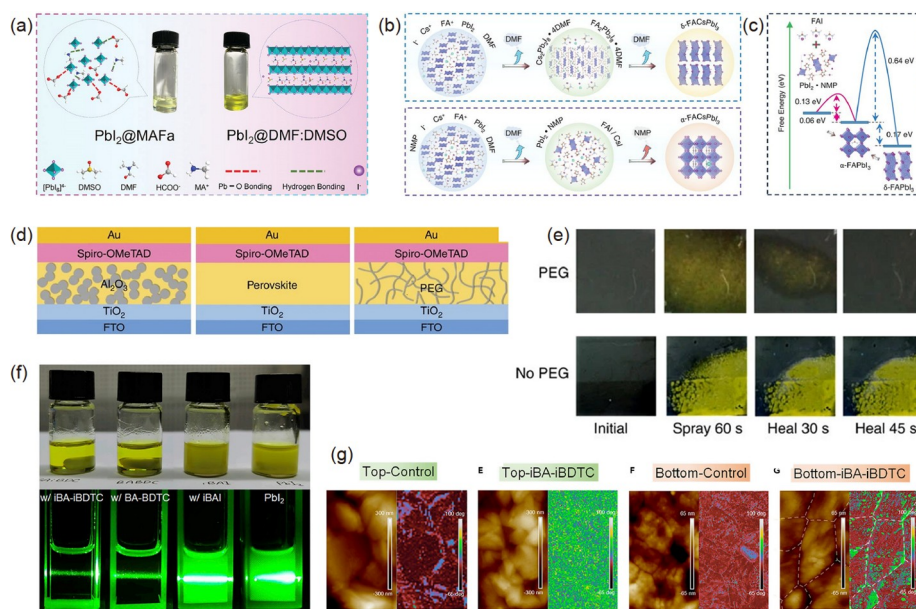


Figure 3 (a) Images of $\text{PbI}_2\text{@MAFa}$ and $\text{PbI}_2\text{@DMF:DMSO}$ solutions and schematic diagram of interactions in the solutions [23]. (b) Schematic diagram of crystal growth with or without NMP [30]. (c) Free-energy calculation for the formation of FAPbI_3 perovskites with or without NMP [30]. (d) Schematic diagram of a mesoporous-scaffold-structured and other PSCs [34]. (e) Photographs of perovskite films with and without PEG after water-spraying for 60 s and kept in ambient air in 45 s [34]. (f) Tyndall effect of PbI_2 solutions in DMF with different additives [35]. (g) AFM morphology and corresponding phase images of the top and bottom surfaces. Scale bar: 1 mm [35] (color online).

affecting the intermediate phase of DMSO with FA^+ , thereby fabricating a highly crystalline perovskite film with preferred (111) orientation. To achieve the phase transition below the thermodynamic phase transition temperature (100 °C), Lu *et al.* [29] created an SCN^- containing atmosphere during the annealing process to transform the δ -phase perovskite into the α -phase. SCN^- possesses the ability to facilitate the formation and stabilization of α -phase perovskite. More radically, Bu *et al.* [30] eliminated the antisolvent by completely replacing DMSO with *N*-methyl-2-pyrrolidone (NMP) in the one-step precursor. They found that PbI_2 tends to form a stable adduct with NMP instead of forming intermediate phases with DMF ($\text{Cs}_2\text{Pb}_3\text{I}_8$ -4DMF and $\text{FA}_2\text{Pb}_3\text{I}_8$ -4DMF) so that PbI_2 can serve as a template to react with embedded formamidinium iodide/cesium iodide (FAI/CsI) *in situ* to form methylamine-free perovskite (Figure 3b). Furthermore, the introduction of NMP can also significantly reduce the formation energy of α -phase perovskites and suppress the formation of δ -phase perovskites, thus enabling the conversion of α -phase perovskites with good photoelectric effect even at room temperature (Figure 3c). As a result, the unpackaged device with 23% efficiency and excellent long-term thermal stability (85 °C, ~80% of initial PCE after 500 h) was achieved.

(3) Multifunctional additives

Perovskite films typically form a wide range of defects due to solution processing and fast crystal growth at relatively low temperatures. Some of the defects tend to form shallow-level traps, such as I or MA vacancy defects, while others are potentially deep-level traps, such as undercoordinated species (halides and Pb^{2+}) and Pb-I antisite defects (PbI_3^-) [31]. Additives with specific structures, including inorganic salts, Lewis acids, Lewis bases, are added to the precursor solution to passivate specific defects while regulating the perovskite crystallization process [31–33]. In particular, multifunctional additives that can simultaneously passivate multiple defects and play additional roles have received particular attention in recent years.

The hydrolysis property makes the performance of PSCs unable to maintain for a long time, which is the main bottleneck hindering its development. Zhao *et al.* [34] introduced a long-chain molecule PEG into the perovskite precursor to act as a scaffold to help form a three-dimensional network, which strongly supports the perovskite grains (Figure 3d). Most strikingly, due to the hygroscopicity of the PEG scaffold and the strong intermolecular interaction between it and methylammonium lead iodide (MAPbI_3), self-healing perovskite devices were realized for the first time: after being damaged by water vapor, the device could quickly return to its original state and efficiency (Figure 3e).

In 2022, Li *et al.* [35] reported a multifunctional additive composed of organic ammonium cations (iBA^+) and dithiocarbamate anions (BDTC^-) to modulate the crystallization

and defects of FA-Cs perovskite films. Figure 3f shows the Tyndall effect based on light-colloid scattering by dissolving 1 M PbI_2 in DMF with different additives. The turbidity and light scattering of the precursor solutions are quite different, which means that there are Pb-I clusters with different sizes and disorders in different solutions. The precursor solution changed from turbid to clear and light scattering became weaker, implying that the size and disorder of the Pb-I clusters decreased. The clearest solution and weakest light scattering indicated that the interaction of BDTC^- with Pb^{2+} was stronger than that of other additives. The AFM phase images of the top and bottom surfaces of the perovskite film indicate that after perovskite film crystallization, iBA^+ penetrated deeply into the grain boundaries (Figure 3g), reaching the bottom surface and distributing around the grain boundaries. Under the synergistic effect of anions and cations, a PSC with an efficiency of 24.25% and excellent operational stability (90% of initial PCE after 500 h) has been achieved.

2.1.2 Interface

As the perovskite layer quality improved, the focus shifted to the optimization of the interfaces to improve the performance of PSCs.

Normal PSC (n-i-p) is stacked by the front electrode, ETL, perovskite light-absorbing layer, HTL, and the back electrode, which contains several key interfaces, including ETL/perovskite interface and perovskite/HTL interface. Notably, carrier extraction/injection, charge transfer/transport, and recombination are directly related to the interfaces. The interface is the place where defects are most easily formed, and these defects form non-radiative recombination centres. Non-radiative recombination induces open-circuit voltage (V_{OC}) loss in PSCs, as illustrated by the following equation [36]:

$$V_{\text{OC}} = V_{\text{OC,rad}} + \ln(\text{PLQE}) \times k_{\text{B}}T/q \quad (1)$$

where $V_{\text{OC,rad}}$ is the radiative (ideal) limit of the V_{OC} , and PLQE is the external photoluminescence quantum efficiency, k_{B} is Boltzmann constant, T is temperature, q is the elementary charge. PLQE is closely related to non-radiative recombination in solar cells. High PLQE means low non-radiative recombination and high V_{OC} of devices, according to Eq. (1). Therefore, interface engineering that can passivate deep defects and reduce non-radiative recombination is beneficial for V_{OC} increment. The performance of PSCs is sensitive to detrimental defects, which are prone to be accumulated at the interfaces and grain boundaries of bulk perovskite films. Moreover, the stability of devices is also highly sensitive to the interface.

The interface engineering not only effectively suppresses non-radiation recombination but also improves the performance of the PSCs by adjusting the energy level alignment between the charge transport layer and perovskite light-ab-

sorbing layer.

(1) Interface engineering at the ETL/perovskite interface

ETLs are defined as electron transport layers, electron collection, or extraction layers whose conduction band minimum (CBM) should be lower than that of a perovskite absorber. The PSC research started with TiO_2 as ETL in 2009, where a PSC was designed with Pt-coated FTO glass substrate and $\text{CH}_3\text{NH}_3\text{PbX}_3$ - TiO_2 photo-electrode, and exhibited the PCE of 3.81% and 3.13% for $\text{CH}_3\text{NH}_3\text{PbI}_3$ and $\text{CH}_3\text{NH}_3\text{PbBr}_3$ absorber, respectively [1]. Kim *et al.* [37] designed PSCs with mesoporous TiO_2 as ETL and delivered a maximum PCE of 9.7%. However, the requirement of high temperature for the growth of mesoporous TiO_2 -based devices gives birth to other potential ETLs, such as compact TiO_2 and SnO_2 owing to their compatibility for low-temperature deposition and easy preparation.

Tan *et al.* [38] reasoned that performance and stability loss in low-temperature planar PSCs could arise from imperfect interfaces and deep trap states present at the perovskite/ETL interface, which could potentially be addressed by passivating the interface between the ETL and the perovskite absorber. They devised chlorine-capped TiO_2 films processed at $<150^\circ\text{C}$ as the ETL (Figure 4a). They found that the interfacial Cl atoms on the TiO_2 can lead to strong electronic coupling and chemical binding, which suppress deep trap states at the perovskite interface and thus considerably reduce recombination at the TiO_2 /perovskite interface. As a result, they fabricated hysteresis-free planar PSCs with certified PCEs of 20.1% for small-area devices (0.049 cm^2) and 19.5% for large-area devices (1.1 cm^2). The PSCs exhibit excellent operational stability and retain 90% of their initial performance after 500 h of operating at their MPP.

In 2021, to improve the V_{OC} , a sparse array of nanoscale TiO_2 cylinders (nanorods) was used as ETL and ultrathin polymer passivation layers ([6,6]-phenyl- C_{61} -butyric acid methyl ester):(poly-methyl methacrylate (PCBM:PMMA)) were inserted between the ETL and perovskite interface by Peng *et al.* [39] (Figure 4b). The resulting nanopatterned ETL-perovskite interface could be effectively passivated by the ultrathin polymer PCBM:PMMA to achieve high V_{OC} that maintained outstanding charge collection and interfacial transport properties. This approach was demonstrated on a large-area (1 cm^2) cell with a certified PCE of 21.6% and an *FF* of 0.839. A champion small-area ($\sim 0.165\text{ cm}^2$) cell achieved a PCE of 23.17% with V_{OC} of 1.240 V and *FF* of 0.845.

With the development of PSCs, SnO_2 is always used as the ETL, due to the many advantages of SnO_2 , such as high electron mobility and good energy-level alignment with perovskite and electrodes [40].

Despite the excellence of SnO_2 , the SnO_2 layer does have a drawback: metal oxides contain surface hydroxyl groups,

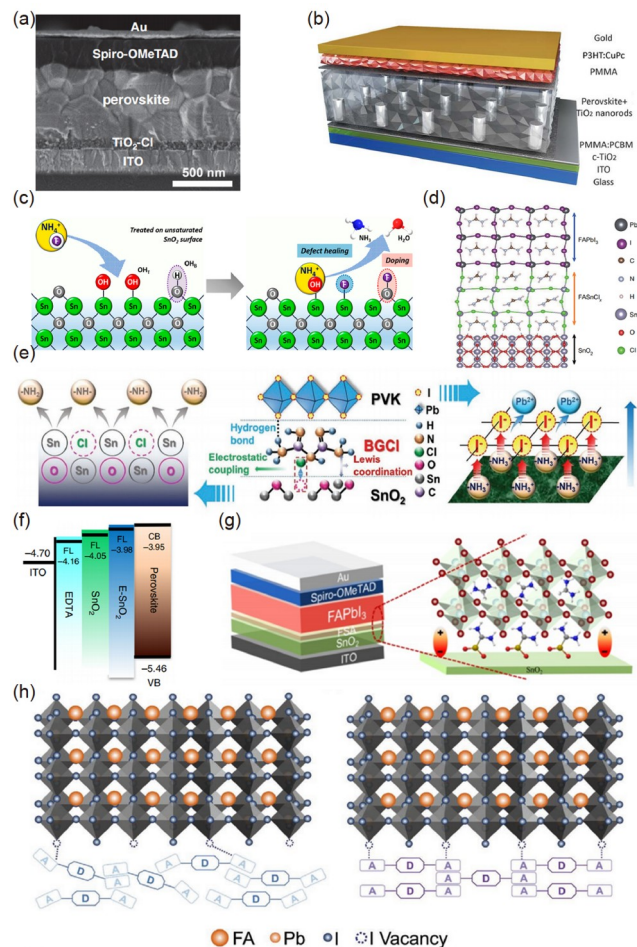


Figure 4 (a) Device structure and cross-sectional scanning electron microscopy (SEM) image of planar PSCs [38]. (b) Schematic of nanopatterned perovskite cell [39]. (c) Schematic illustration of NH_4F treatment on SnO_2 surface [42]. (d) Simulation of the formation of the interlayer between perovskite and SnO_2 [44]. (e) Schematic of the proposed modification mechanism of the BGCl at the ETL/PVK interface [45]. (f) Schematic illustration of Fermi level of EDTA, SnO_2 , and E- SnO_2 relative to the CBM of the perovskite layer. (g) Schematic structure of the FSA-FAPbI₃ based device and FSA induced dipole moment at the SnO_2 /perovskite interface [47]. (h) Schematic of passivation mechanism achieved by ITIC-Th and IT-CI [48] (color online).

and these generate trap states near the valence band [41]. To reduce defect sites and improve the performance of PSCs, Sargent *et al.* [42] used ammonium fluoride (NH_4F) to treat the surface of SnO_2 . They reported that an NH_4F surface treatment could eliminate hydroxyl groups from the SnO_2 surface and also dope it with fluorine ions (Figure 4c). The treated PSCs achieved a PCE of 23.2% in light of higher voltage than in relevant controls.

Besides, interfacial Cl atoms also lead to strong electronic coupling and chemical bonding at the ETL/perovskite planar junction [43]. Seok *et al.* [44] reported the formation of an interlayer between SnO_2 and perovskite light-absorbing layer, achieved by coupling Cl-bonded SnO_2 with a Cl-containing perovskite precursor. They reported the formation

of a coherent interlayer between a perovskite thin film and a Cl-bonded SnO_2 (Cl-bSO) electrode coated with a Cl-containing FAPbI_3 perovskite precursor (Cl-cPP) solution. From analytical characterizations, they inferred the formation of a crystalline FASnCl_x phase as an atomically coherent interlayer between the perovskite and SnO_2 (Figure 4d). This interlayer between the perovskite and ETL reduces the interfacial charge recombination loss and contact resistance, enabling the fabrication of a PSC with a PCE of 25.8%.

Similarly, a multifunctional interfacial material, biguanide hydrochloride (BGCl), was introduced between SnO_2 and perovskite to enhance electron extraction, as well as the crystal growth of the perovskite [45]. The BGCl can be chemically linked to the SnO_2 through Lewis coordination/electrostatic coupling and help to anchor the PbI_2 (Figure 4e). Better energetic alignment, reduced interfacial defects, and homogeneous perovskite crystallites were achieved, yielding an impressive certified PCE of 24.4%, with a V_{OC} of 1.19 V and an FF of 82.4%. More importantly, the unencapsulated device maintains 95% of its initial PCE after aging for over 500 h at 20 °C and 30% relative humidity in ambient conditions.

In addition, some important developments are made in the study of the ETL/perovskite interface to improve the performance of PSCs. In 2018, Liu *et al.* [46] used ethylenediaminetetraacetic acid (EDTA)-complexed SnO_2 as ETL. The Fermi level of EDTA-complexed SnO_2 is matched well with the CBM of perovskite, leading to high V_{OC} (Figure 4f). The PCE of planar-type PSCs with EDTA-complexed SnO_2 increases to 21.60% (certified at 21.52% by Newport) with negligible hysteresis. In 2022, Zhao *et al.* [47] introduced a zwitterion-functionalized SnO_2 as the ETL to induce the crystallization of high-quality black phase FAPbI_3 on such SnO_2 substrate. The SnO_2 ETL treated with the zwitterion, formamidinium sulfinic acid (FSA), can suppress the deep-level defects at the SnO_2 /perovskite interface and help rearrange the stack direction, orientation, and distribution of residual PbI_2 in perovskite layer, which reduces the side effect of the residual PbI_2 to the perovskite structure (Figure 4g).

Apart from the work on tailoring ETLs, interlayers are also studied for defect passivation. A planar structural molecule was designed and added to the precursor solution which sank to the ETL/perovskite interface during the annealing process (Figure 4h). As a result, a network well-matched with a perovskite lattice was formed. Contributing to the effective reduction of defect sites at the interfaces, the targeted device achieved a PCE of over 25% [48].

(2) Interface engineering at the perovskite/HTL interface

Solution-processed perovskite films are usually polycrystalline, which means they contain substantial structural disorders, such as grain boundary defects and crystallographic defects. The surface is the place where defects are most easily formed, and passivation of the surface defects is always

the most important task in any type of solar cell. In PSCs, several efficient surface passivation methods have been adopted to improve the performance of PSCs, such as two-dimensional (2D) perovskite [49–51], organic halide salt [52,53], lead oxysalt [54], and wide-bandgap halide [55,56].

2D halide perovskites have recently been recognized as a promising avenue in PSCs in terms of encouraging stability and defect passivation effect. In 2018, Wang *et al.* [49] reported an innovative facile solution method for *in situ* growth of 2D PEA_2PbI_4 capping layer to passivate surface defects, where by spin-coating a phenethylammonium iodide (PEAI) solution upon the 3D perovskite film, 2D perovskite PEA_2PbI_4 layer was formed by the following reaction of PEAI with excess PbI_2 (Figure 5a). Similarly, Ho-Baillie *et al.* [50] reported that using a mixture of bulky organic ammonium iodide (*iso*-butylammonium iodide, iBAI) and FAI enhances both PCE and stability. Through a combination of inactivation of the interfacial trap sites, and the formation of an interfacial energetic barrier, ionic transport is reduced (Figure 5b).

To further improve the performance of PSCs, You *et al.* [52] developed an organic halide salt, PEAI, for post-treatment of mixed perovskites to suppress the surface defects of perovskite polycrystalline films for efficient solar cells in 2019 (Figure 5c). Surprisingly, the organic halide salt, PEAI, rather than the 2D layered PEA_2PbI_4 perovskite proposed in many recent studies, serves as a much more effective passivation additive for a 3D perovskite. They carefully controlled the conversion process of PEAI to PEA_2PbI_4 in the actual devices and showed that the existence of PEAI instead of PEA_2PbI_4 leads to the best result of passivation. As a result, a 23.32%-certificated PCE has been achieved for the PSC. In addition, a V_{OC} as high as 1.18 V was achieved at the absorption threshold of 1.53 eV, which is 94.4% of the S-Q limit V_{OC} (1.25 V). In 2022, Yang *et al.* [53] also reported the heterointerface between the top perovskite surface and an HTL is often treated for defect passivation to improve PSC stability and performance. However, such surface treatments could also affect the heterointerface energetics and may induce a negative work function shift (*i.e.*, more n-type), which activates halide migration to aggravate PSC instability. To solve the above problems, they introduced an ion $[\text{TsO}]^-$, which has the strongest electron-withdrawing character, to replace the iodine ions in OAI to neutralize negative ΔW (Figure 5d). Therefore, despite the beneficial effects of surface passivation, this detrimental side effect limits the maximum stability improvement attainable for PSCs treated in these ways.

For silicon technology, surface structural defects are generally passivated by silicon oxide, silicon nitride, or aluminum oxide, which form strong covalent bonds to silicon. Therefore, Huang *et al.* [54] demonstrate a general passivation strategy for lead halide perovskites by forming a thin,

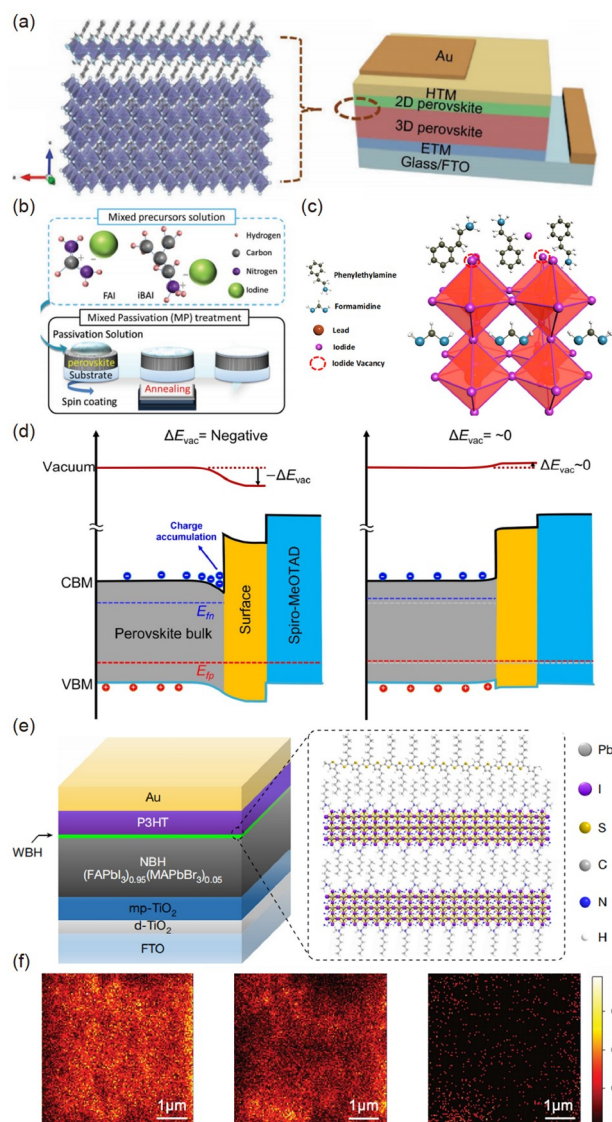


Figure 5 (a) Schematic illustrations of the crystal structure of 2D-3D perovskite films and the device architecture [49]. (b) Schematic of the MP passivation treatment method with FAI and IBAI [50]. (c) Possible passivation mechanism of the PEA layer for the perovskite film [52]. (d) Schematic interpretation of the heterointerface band alignments of the OAI-treated and OATsO-treated devices under illumination in open-circuit condition [53]. (e) Double-layered halide architecture of P3HT-based PSCs. Left, the structure of an n-i-p PSC is based on a DHA using P3HT as the hole-transport material. Right, schematic structure of the interface between the WBG perovskite and P3HT [55]. (f) Degradation mapping of TOF-SIMS signals of I in the HTLs for perovskite/spiro-OMeTAD, perovskite/GO/spiro-OMeTAD, and perovskite/CI-GO/spiro-OMeTAD, respectively [58] (color online).

compact inorganic lead oxysalt layer on the perovskite surface through *in situ* reaction with selected inorganic anions. The surface lead oxysalt layer formed strong chemical bonds with the perovskite and afforded much better resistance to many detrimental stimuli under ambient atmosphere and light irradiation. Its passivation effect enhanced the PSC efficiency and stability. An all-in-one strategy was reported, which integrated the passivation of perovskite layers with the

oxidation of 2,2',7,7'-tetrakis[*N,N*-di(4-methoxyphenyl)amino]9,9'-spirobi fluorene (spiro-OMeTAD). The ionic liquid 1-ethyl-3-methylimidazolium bis(trifluoromethylsulfonfyl) imide (EIm-TFSI) was used to replace the conventional oxidant lithium bis(trifluoromethanesulfonyl)imide (Li-TFSI). The oxidation products EIm was found to be able to spontaneously penetrate into the perovskite layer and functioned as passivator which readily reduced the defect density [57].

The typical HTLs used in n-i-p devices include spiro-OMeTAD, poly(3-hexylthiophene-2, 5-diyl) (P3HT), poly[bis-(4phenyl)(2,4,6-trimethylphenyl)amine] (PTAA). Spiro-OMeTAD is always used as the HTL of high-performance PSCs. There are also many excellent studies in order to improve the performance of P3HT-based and PTAA-based devices.

Seo *et al.* [55] proposed a device architecture for highly efficient PSCs that use P3HT as a HTL without any dopants. Despite the potential advantages of P3HT as an organic HTL in PSCs, the resulting devices have a low V_{OC} due to additional non-radiative recombination at the perovskite/P3HT interface. In order to solve this problem, they reported a thin layer of wide-bandgap (WBG) halide perovskite on top of the narrow-bandgap (NBG) light-absorbing layer by an *in-situ* reaction of *n*-hexyl trimethyl ammonium bromide on the perovskite surface to reduce recombination at the perovskite/P3HT interface (Figure 5e). The device has a certified PCE of 22.7%; exhibits good stability at 85% relative humidity without encapsulation; and upon encapsulation demonstrates long-term operational stability for 1,370 h under 1-sun illumination at room temperature, maintaining 95% of the initial efficiency.

Han *et al.* [58] reported a solution-processing strategy to construct strong chemical bonds of Pb–O and Pb–Cl by deposition of Cl-GO at the surface of perovskite films which can largely impede the loss of PSC, resulting in less damage to the organic HTL (PTAA) (Figure 5f). They fabricated PSCs with efficiencies approaching 21% on an aperture area of 1.02 cm². The PSC with stabilized heterostructure exhibited excellent operational stability, maintaining 90% of its initial value after aging under the maximum power point and 60 °C for 1,000 h. Meng *et al.* [59] used a quinoxaline-based D-A copolymer PBQ6 as a doping-free HTL instead of spiro-OMeTAD, and achieved PCE of 22.6% for the n-i-p PSCs with significantly improved stability.

2.2 PSCs with p-i-n structure

The first p-i-n PSCs were proposed by Wen *et al.* [4] despite the low efficiency of 3.9%. Soon, the efficiency was improved to over 15% even in a 1 cm² area by Han *et al.* [60] using a heavily doped inorganic charge transport layer (CTLs), greatly promoting the research interests. Li and

Fang *et al.* [61] further increased efficiency to 16.6% by using the non-doped polyelectrolytes (P3CT) hole transporting layer. Inverted PSCs were generally dominating perovskite-fullerene planar heterojunction, though other types like bulk and graded heterojunction have been reported. Inverted p-i-n PSCs owned advantages of simple processing, low temperature, easy flexibility, and low hysteresis, due to the absence of commonly used high-temperature sintered, potentially photocatalytic TiO_2 and doped organic transporting material in regular n-i-p devices. Besides, inverted PSCs were compatible with Si-based solar cells to fabricate perovskite/Si tandem devices. The PCE of inverted PSCs has been greatly improved over the past five years with the modifications of bulk and interface passivation. Figure 6 shows the efficiency roadmap of inverted PSCs. To date, the efficiency of small-area inverted PSCs has reached a certified record efficiency of 24.3% [62]. This part will summarize the main progress of inverted PSCs with focusing on device engineering, including perovskite bulk and interface designs.

2.2.1 Perovskite layer

In PSCs, perovskite film is the light absorber that plays a decisive role in photovoltaic performance. Uniform films with high crystallinity and low defect density are required to achieve high efficiency. A stable perovskite precursor solution is of first concern for high-quality perovskite films. Huang *et al.* [63] found that organic iodide perovskite precursors can be oxidized to I_2 , accompanied by I_3^- -induced charge traps in perovskite films. Aiming to this, they added benzylhydrazine hydrochloride (BHC) to reduce the detrimental I_2 back to I^- , and improved device efficiency to 23.2%. Besides, employing functional additives was a more widely used method to regulate perovskite films. For example, Wu *et al.* [64] proposed an additive engineering strategy by using methylammonium acetate (MAAc) and

thio-semicarbazide to simultaneously modulate the morphology and crystalline quality, realizing uniform MAPbI_3 films with large crystal size and low density of defects. The resulting PSCs exhibited a certified PCE of 19.19% with an aperture area of 1.025 cm^2 .

Apart from film regulation, deep-level defects in bulk perovskite would induce severe non-radiative carrier recombination, limiting device efficiency. Therefore, proper defect passivation in bulk is crucial for realizing high-performance PSCs. Fang and Li *et al.* [65,66] developed *in-situ* crosslinking methods to passivate defects at grain boundaries and further inhibit the ions migration in perovskite through introducing cross-linkable trimethylolpropane triacrylate additives, achieving ~20% efficiency with good stability. Recently, Zheng *et al.* [67] introduced a trace amount of long-chain alkylamine ligands (AALs) into the perovskite film to assemble on grain boundaries, resulting in a lower trap-state density across the higher energy region from 0.32 to 0.4 eV. As a result, the inverted devices with AALs achieved a certified PCE of 22.3% with a V_{OC} of 1.14 V. Gharibzadeh *et al.* [68] found that alkylammonium (PEACl) additive can self-assemble into 2D perovskite in perovskite films to passivate the grain boundaries and perovskite/ C_{60} interface, thus increasing devices efficiency to 22.7% with V_{OC} and FF up to 1.162 V and 83.2% respectively.

Ionic liquids were also widely used to passivate defects in inverted PSCs. For example, Lin *et al.* [69] incorporated 1-butyl-1-methylpiperidinium tetrafluoroborate ($[\text{BMP}]^+[\text{BF}_4]^-$) into inverted PSCs to suppress the deep trap states and compositional segregation in perovskite films during aggressive aging. As a result, over 20% efficiency and excellent stability were achieved in PSCs with ideal bandgap (1.66 eV) for subcell in perovskite/Si tandem devices. 1-butyl-3-methylimidazolium tetrafluoroborate (BMIMBF_4) was also reported in PSCs by Snaith and Gao *et al.* [70] to suppress ion migration in perovskite under illumination and heat, thus increasing device efficiency from 18.7% to 20%, along with remarkably improved long-term device stability.

2.2.2 Interface

(1) Top interface

Despite the greatly improved performance, one major challenge for inverted PSCs still lies in their low efficiency in comparison with regular devices. The perovskite/transporting layer interface should be one of the main reasons, especially the top perovskite interface. Huang *et al.* [71] found that trap densities in perovskite surface was 1–2 orders of magnitude larger than that in bulk perovskite. Neher *et al.* [72] further verified the non-radiative recombination pathways in inverted PSCs and found severe quasi-Fermi-level splitting losses (~80 mV) at perovskite/transporting layer interface caused by interfacial recombination, inducing inevitable V_{OC} loss of the devices.

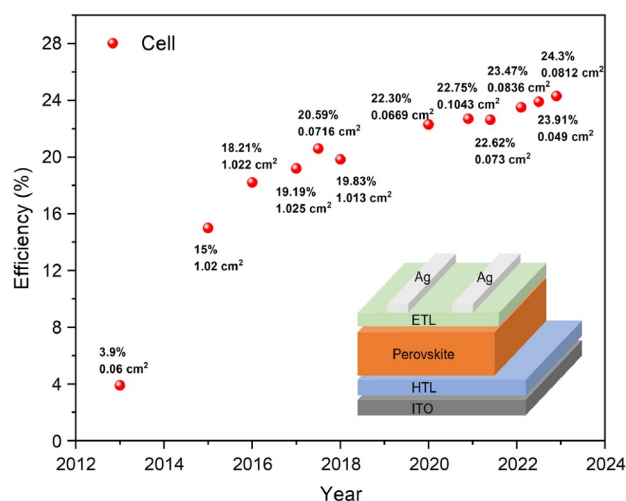


Figure 6 Efficiency evolution of inverted PSCs (color online).

To suppress the interfacial recombination, one method was to remove or regrow the defective surface. Given the soft nature of the perovskite surface, Huang *et al.* [73] proposed a physical method to peel-off the defective layer with adhesive tapes and improved the devices efficiency to 22%. Zhu *et al.* [74] developed a solution-processed secondary growth (SSG) technique to reduce nonradiative recombination in inverted PSCs. In this method, guanidinium bromide (GABr) was spin-coated on top of perovskite films to form a wider bandgap region near the surface (caused by the Br^- ions in GABr), reducing the electron-hole recombination at perovskite surface. In addition, SSG-processed perovskite tended to be more n-type, which will help to occupy the initial electron traps and thus reduce trap-assisted recombination. As a result, a high V_{OC} of 1.21 V was obtained in SSG-based inverted PSCs with efficiency approaching 21%.

Surface passivation was another widely adopted method to suppress interfacial recombination. Due to the ionic nature of perovskite materials, different charged defects existed on the perovskite surface, including positive, negative, and even neutral defects. Li *et al.* [75] developed an iodized fullerene derivative (PCBB-3N-3I) to passivate the positively charged defects through the binding between I^- ions in PCBB-3N-3I and under-coordinated Pb^{2+} on the perovskite surface. Such binding would promote the molecular arrangement of PCBB-3N-3I with a preferred molecular orientation. As a result, an interfacial dipole was formed at the perovskite interface to benefit electron extraction, leading to device efficiency increasing from 17.7% to 21.1%. Wenger *et al.* [76] proposed a simple oxidation passivation method to reduce the neutral Pb^0 defects in perovskite films. By directly using H_2O_2 as a post-treatment to oxidize Pb^0 to PbO , the devices efficiency was obviously improved to 19.2%. Jen *et al.* [77] designed a bifunctional molecule of piperazinium iodide with both R_2NH and R_2NH_2^+ groups, which would act as an electron donor and an electron acceptor to passivate different defects in perovskites. Besides, the surface residual stress and n-type properties can also be improved in perovskite films, leading to a high efficiency of 23.37% (certified 22.75%). Apart from organic passivators, Bakr *et al.* [78] adopted CsPbBrCl_2 quantum dots (QD) with oleic acid ligands as an anti-solvent suspension to passivate perovskite films. When QD met with wet perovskite films, it would decompose and leave elemental dopants in bulk perovskite and oleic acid ligands on perovskite surface. These Br or Cl elements worked as elemental passivation, while the ligands worked as molecular passivation due to the strong bonding between Pb atoms and the $-\text{COOH}$ groups. Based on the synergistic function, the devices efficiency was greatly improved from 18.3% to 21.5%.

Up to now, most inverted PSCs adopted the same passivating methods or materials that have been successfully applied to regular devices. Despite the great efficiency im-

provement, their performance was still inferior to those of regular devices. The main reason should lie in the requirement difference in energy level alignment and carriers transporting direction at perovskite surface in regular and inverted PSCs. Taking the perovskite top surface as an example, electrons were expected to transport upward in inverted PSCs, while they were expected to transport downward in regular devices. Therefore, it may be necessary for inverted PSCs to redesign their passivating materials or methods to obtain higher efficiency. Vaynzof *et al.* [79] proposed a dual interfacial modification method with PEAI insertion at both top and buried interface to fabricate efficient inverted PSCs with an efficiency of over 23%. Different from traditional 2D perovskite passivation, they found that the main function of PEAI at the buried interface was to optimize perovskite growth rather than defect passivation. The PEAI at the top surface can effectively passivate interfacial defects by PEAI itself, not 2D perovskite, since no 2D perovskite was detected at the perovskite surface. They thought that 2D perovskite may reduce electron extraction at the perovskite interface due to the high bandgap of 2D perovskite and thus a much low concentration of PEAI was adopted at the perovskite surface to obtain the best device performance. Sargent *et al.* [80] found that in 2D perovskite with $n=1$ or 2, quantum confinement would upshift the CBM, which was much higher than that of 3D perovskite (Figure 7a), thus inducing a large barrier for electron extraction in inverted PSCs. Based on this, they reported quantum-size-tuned 2D/3D perovskite heterostructures to fabricate efficient inverted PSCs using MAI and 2D ligand mixture in DMF and IPA mixed solution. Using this method, the 2D perovskite capping layer can be well tuned with $n \geq 3$, thus downshifting the CBM of 2D perovskite and reducing the electron extraction barrier. As a result, the efficiency of inverted PSCs can be further increased to 23.9% (certified). Given the fact that lower formation energy was needed to form 2D perovskite with a high n value, Azmi *et al.* [81] treated the 3D perovskite surface with oleylammonium iodide operating at room temperature to form higher-dimensionality 2D perovskite capping layer ($n \geq 2$), while traditional thermal treatment would form 2D perovskite with $n=1$ (Figure 7b). Compared with the thermal process, room temperature processed 2D perovskite exhibited much closer CBM to the C_{60} transport layer, thus reducing the energy loss during electron extraction. Using this tailored 2D/3D heterojunction, high efficiency of 24.3% was obtained in inverted PSCs.

Recently, from the point of interfacial heterojunction, Fang and Li *et al.* [82] constructed robust perovskite/PbS heterojunction (Figure 7c) through surface sulfidation (SST) of Pb-rich perovskite interface with hexamethyldisilathiane. After SST, perovskite surface tended to be more n-type with obviously upshifted Fermi level in comparison with bulk per-

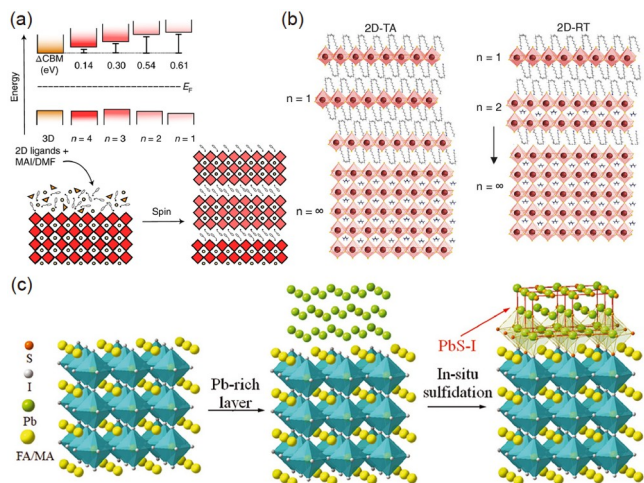


Figure 7 Recent strategies to fabricate high efficiency inverted PSCs using surface optimization. (a) Quantum-size-tuned 2D/3D perovskite heterostructures [80]. (b) Room temperature processed higher-dimensionality 2D perovskite capping layer [81]. (c) Surface sulfidation to construct perovskite/PbS heterojunction [82] (color online).

ovskite. As a result, electrons would flow to bulk perovskite from the surface spontaneously, generating an extra back-surface field pointing towards the ITO front electrode. Such an extra field was in the same direction as the built-in potential of inverted PSCs, thus promoting electron extraction and inhibiting holes transport toward the electrons transport layer. In addition, the S element can also passivate interfacial defects due to the strong binding between S and Pb. Using P3CT [61] as hole transporting layer and PCBM as the electron transporting layer, the resulting inverted PSCs exhibited a record efficiency of 24.3% (certified 23.5%) with excellent stability. Zhu *et al.* [62] reported efficient inverted PSCs by using ferrocenyl-bis-thiophene-2-carboxylate (FcTc_2) to modify the perovskite surface. FcTc_2 not only passivated defects with strong Pb–O bonds but also promoted interfacial electron transfer through the electron-rich and electron-delocalizable ferrocene units. As a result, high efficiency of 25.0% (certified 24.3%) can be obtained, which was the highest reported efficiency for inverted PSCs.

(2) Buried interface

Apart from the above-mentioned top interface, buried interfaces in PSCs are also crucial to device performance due to the high-density defects existing in the bottom interface, which would induce non-radiative recombination and limit device performance [83,84]. However, owing to their non-exposed feature, accessing buried interface is more difficult compared to that of the top perovskite surfaces. Zhu *et al.* [85] reported a lift-off method based on the solution-immersion process (Figure 8), and found that the sub-micro-scale extended imperfections and lead-halide inhomogeneities in the buried interface hindered the improvement of device performance. Huang *et al.* [86] developed a peeling-off method by epoxy encapsulant to characterize buried in-

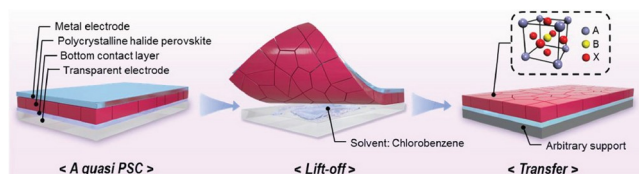


Figure 8 Schematic of the lift-off process with the solution-immersion method. The PTAA transporting layer in the lift-off process served as a sacrificial layer [85] (color online).

terfaces and found a high density of voids at the perovskite-substrate interfaces, which should be induced by the removal of DMSO during perovskite formation. Partial replacement of DMSO with solid-state carbonylhydrazide (CBH) reduced interfacial voids and increased device efficiency to 23.6%.

Up to now, PTAA [62] (highest efficiency of 25.0%), P3CT [82] (highest efficiency of 24.3%), and NiO_x were the most successful hole transporting layers for perovskite grown on the top of inverted PSCs. To passivate the buried PTAA/perovskite interface, Stollerfoht *et al.* [72] functionalized the PTAA layer with the interface compatibilizer poly[(9,9-bis(30((*N,N*-dimethyl)-*N*-ethylammonium)-propyl)-2,7-fluorene)-alt-2,7-(9,9-dioctylfluorene)] dibromide (PFN-P2). The amphiphilic properties of PFN-P2 improved the wetting of the perovskite film on the hydrophobic PTAA, thus greatly enhancing the fabrication yield of the cells without frequent pinhole formation. The triple cation perovskite deposited on PTAA/PFN-P2 showed a high average quasi-Fermi-level splitting (QFLS) of approximately 1.19 eV, which represented a significant enhancement of approximately 65 meV compared with the QFLS of the perovskite directly on PTAA. With a minimal loss in V_{OC} , the champion efficiency was improved to 21.6%. To suppress non-radiative recombination at interfaces and enhance charge selectivity from perovskite to HTL, Wu *et al.* [87] introduced a large alkylammonium interlayer (LAI) between PTAA and perovskite. As a result, the reduced surface recombination velocity (SRV) and trap state density (N_t) enable a substantially improved photovoltage from 1.12 to 1.21 V for the PSCs with an optical band gap (E_g) of 1.59 eV, leading to a champion PCE over 22%.

As to buried NiO_x /perovskite interface, it usually induced lower V_{OC} in PSCs than PTAA. Boyd *et al.* [88] found that the undercoordinated metal cation sites (Ni^{2+}) from NiO_x can act as Lewis electron acceptors that deprotonated cationic amines and oxidized iodide species, thus creating an extraction barrier to holes and resulting in a lower V_{OC} . With the use of excess A-site cation that acted to compensate for organic cation, the modified device yielded an increase in V_{OC} values to 1.15 V. Chen *et al.* [89] found that large organic cations (GUA) can bind strongly to undercoordinated oxygens in the NiO_x , serving as nuclei for GUA_2PbI_4 growth. As a result, the non-radiative recombination was effectively suppressed at the NiO_x /perovskite interface by 2D GUA_2 -

PbI₄, leading to a 65 mV increase of V_{OC} and a champion PCE of 22.9%.

Recently, self-assembled monolayers (SAMs) binding to the transparent conductive oxide (TCO) were also reported to replace traditional PTAA, NiO_x or P3CT [82,90] hole transporting layer and improve the buried perovskite interface [91], owing to their minimal parasitic absorption, low material consumption and great potential for conformal deposition on the rough substrate. For example, Wu *et al.* [92] proposed a novel anchoring-based co-assembly strategy that involved a synergistic co-adsorption of a hydrophilic ammonium salt CA-Br with hole-transporting triphenylamine derivatives to acquire wettable organic hole-extraction monolayers. A mini-module was firstly fabricated using SAMs and achieved a PCE of 12.67% for an aperture area of 36 cm².

The photovoltaic performance of p-i-n PSCs has been increasing fast in recent years. To further improve device efficiency, interfacial engineering, especially the energy level regulation at the perovskite/transporting layer interface should be greatly noticed to increase the QFLS of PSCs and promote charges extraction, thus inducing much higher V_{OC} . Besides, full passivation of potential defects should also be noted at both the bulk and surface of perovskite film, suppressing carrier recombination and improving device short-circuit current density J_{SC} and FF. Based on these achievements, we believe the single junction p-i-n devices would achieve comparable efficiencies of n-i-p PSCs. We also note that perovskite-based tandem devices were mostly fabricated using the p-i-n device structure, and thus the device engineering on both WBG and NBG inverted PSCs requires further contributions from this area.

2.3 Printable mesoscopic PSCs

Great success of in-lab cells inspires a wide range of interest in industrializing PSCs for cost-effective photovoltaic technologies. Industrial production needs to overcome additional challenges besides those which have been widely studied for lab PSCs. To meet the demands of industrialization, Han's group [93] firstly reported a printable mesoscopic perovskite solar cells (p-MPSCs) in 2013. p-MPSCs are composed of a triple mesoscopic layer of TiO₂/ZrO₂/carbon on the TCO substrate while perovskite is filled inside the pores, as shown in Figure 9a [94]. In this device configuration, TiO₂ serves as the ETL and extracts electrons, carbon serves the back electrode and extracts holes, ZrO₂ serves as the scaffold to load perovskite and the spacer to prevent direct contact between ETL and the back electrode, and perovskite serves as the light absorber and the hole transporter. The energy levels diagram of corresponding layers is shown in Figure 9b [94]. The hole-conductor-free character and the carbon electrode help reduce the cost of PSCs. Meanwhile, all functional

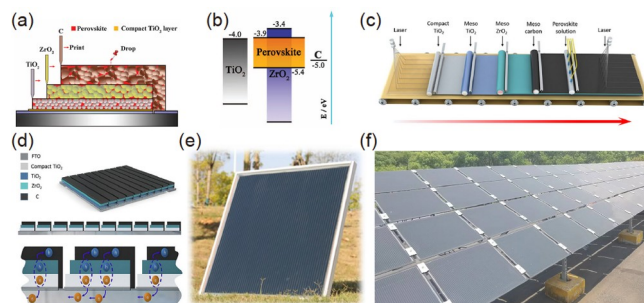


Figure 9 (a) Schematic structure of p-MPSCs. (b) Energy levels diagram of p-MPSCs [94]. (c) Schematic illustration of the production flow of p-MPSCs. (d) Interconnection scheme of printable mesoscopic perovskite solar modules [95]. (e) Printable mesoscopic perovskite solar module with the dimension of 60 cm by 60 cm [95]. (f) Stable perovskite PV system with 3,600-cm² printable mesoscopic perovskite solar modules [96] (color online).

layers including the back electrode in p-MPSCs are fabricated *via* solution-processed methods while evaporation is excluded (Figure 9c). The inexpensive components and the fully solution-processable character minimize the cost and make p-MPSC a great choice for low-cost photovoltaics.

Different from its analogues, scaling up p-MPSCs for large-area modules with similar scales as that of standard silicon panels to meet the basic requirement of real applications is not so challenging. To fabricate perovskite solar modules, large-area compact and dense perovskite films should be realized first. Perovskite films for present efficient PSCs are generally fabricated by spin coating while the spin coating is found to be not suitable for depositing large-area films. Blade coating and slot-die coating methods have been developed to substitute spin coating. The remaining concern is that the PCE of modules fabricated by these methods lagged behind that of the spin-coated ones since non-uniformity and pin holes are detrimental to the performance of PSCs, especially for modules. However, FTO is much rougher than ITO and how to deposit a thin and compact ETL on FTO to avoid direct contact between perovskite and the window electrode remains a concern. In p-MPSCs, there is no individual perovskite film since perovskite is indeed buried inside the pores and constructs a bulk composite layer with thick mesoscopic scaffolds of several micrometers [93]. The ETL in p-MPSCs is about hundreds of nanometers, which can fully cover the rough substrate. It is worth noticing that the back electrode in p-MPSCs is prepared before the filling of perovskite. In this case, the contact between perovskite and the carbon electrode can be well ensured during the growth of perovskite. Based on these special characteristics, p-MPSCs were upscaled with the dimension of 60-cm by 60-cm and a stable photovoltaic system was successfully launched with the 3,600-cm² modules for power generations (Figure 9d–f) [95,96].

p-MPSCs have demonstrated very encouraging stability

results while convincing stability is another requirement for PSCs to be industrialized (Figure 10a). The stability of PSCs is determined by all components in the device. Carbon has been widely regarded as a stable electrode material for PSCs since it will not migrate or react with perovskite in the device. The hole-conductor-free character makes p-MPSCs bear no additional stability concern induced by hole conductors. Light soaking heats the device and leads to the expansion of perovskite with a large thermal expansion coefficient while the mismatched expansion would induce interface degradation due to strain. The mesoscopic scaffold confines perovskite inside the pores and helps protect perovskite from such threats. Ion migration of perovskite restricts the long-term stability of PSCs under working conditions. The mesoscopic scaffold localizes perovskite in the nanoscale and obstructs ion migration. The grain boundaries and freely-formed interface in p-MPSCs can be further enhanced by proper additives to inhibit ion migration or species loss. P-MPSCs with 5-ammonium valeric acid (5-AVA) bifunctional molecule has demonstrated stability at a maximum power point of $55 \pm 5^\circ\text{C}$ for more than 13,000 h without obvious decay and meet key stability standards of IEC61215:2016. The proposed mechanism and test results are shown in Figure 10b, c [6]. It is also found that the thick scaffold of p-MPSCs may weaken the electric intensity inside the device and suppress ion migration, which makes p-MPSCs remarkably resilient against reverse-bias stress [97].

The challenge for p-MPSCs is that their PCE is not so high as those of conventional ones though their theoretical efficiency will be expected to exceed the efficiency of existing p-n junction photovoltaic devices. The special device configuration and fabrication flow make most methods for conventional PSCs not suitable for p-MPSCs although the key to improving device performance is always enhancing beneficial dynamic processes such as charge extraction and charge transport and suppressing undesired dynamic processes such as non-radiative recombination. Various methods have been developed and improved the PCE of p-MPSCs (Figure 10d). Controlling the crystallization of perovskite is fundamental for all kinds of PSCs. Since solvent in the thick scaffold of p-MPSCs cannot be removed as rapidly as requested for preparing compact and uniform perovskite films for conventional PSCs, different strategies have been developed. The additive of 5-AVA was firstly introduced to template the growth of MAPbI₃ with its carboxyl group adsorbed on the surface of the scaffolds or contacting each other at the grain boundaries and with its ammonium group grown in perovskite. This method realized full infiltration of perovskite and a certified PCE of 12.84% in 2014 [94]. Recently, a growth-dominated crystallization process was further developed to inhibit the nucleation process and promote the growth process of perovskite in the scaffold by

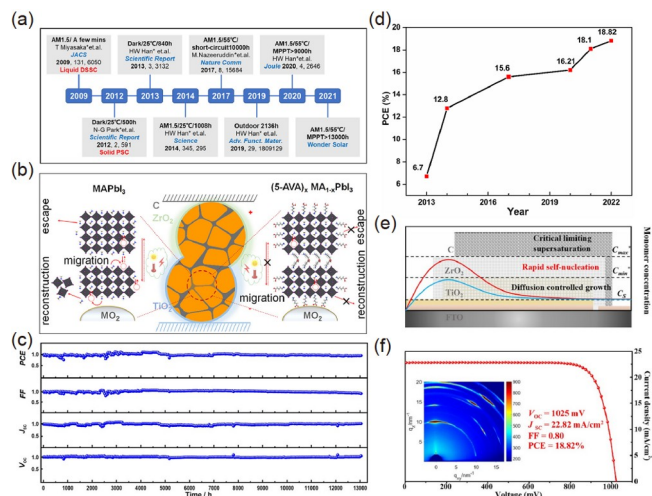


Figure 10 (a) Stability development chronology of p-MPSCs. (b) Proposed mechanism for enhancing the stability of p-MPSCs [6]. (c) Performance evolution of p-MPSCs aged at a maximum power point of $55 \pm 5^\circ\text{C}$. (d) PCE chart of p-MPSCs [93,94,98,100,110,111]. (e) Schematic of the growth-dominated crystallization process in the p-MPS [99]. (f) current density-voltage (J - V) curve of the corresponding champion p-MPSC with the PCE of 18.82%, inset is the GIWAXS map of perovskite in the mesoscopic scaffold [98] (color online).

adopting the solvent of *N*-methylformamide (NMF) and balancing the crystal growth process and the solvent removal process (Figure 10e). GIWAXS measurement distinguished that the obtained perovskite inside the non-ordered pores exhibited high orientation, indicating that perovskite experienced an enhanced growth process (Figure 10f). A champion PCE of 18.82% was successfully obtained *via* this method (Figure 10f) [98]. Additive engineering is an effective strategy for the PCE enhancement of p-MPSCs as conventional ones. Various additives have been attempted to modulate the crystallization [94,99], promote charge transport [100], passivate defects [101], optimize energy level alignment [102], and enhance charge extraction in p-MPSCs [103]. Meanwhile, progress has been also obtained by developing ETL and carbon electrodes for enhanced charge extraction and suppressed interface recombination [104,105].

In addition to the above p-MPSCs, there also exist some other similar ones, which also show good performance in efficiency and stability. Zhou *et al.* [106] developed a low-temperature fabrication routine for hole-conductor-free MPSCs. They used a TiO₂ nanoparticle-binding carbon electrode as the back electrode, and adopted the vacuum treatment to assist the infiltration and crystallization of the organic-inorganic hybrid perovskite. Finally, a >12% PCE and >220 days storage-stability were achieved. Hinsch *et al.* [107] reported a fill factor assessment in hole-conductor-free carbon electrode-based PSCs, and achieved a certified power conversion efficiency of 15.5%. Kim *et al.* [108] employed 2D-perovskite as an electron-blocking layer PSCs with

printable low-temperature carbon electrode, and achieved a PCE of 18.5%. To further improve the PCE of p-MPSCs towards that of conventional ones, optimizing the selectivity of charge extraction restricted by the absence of hole conductors is critical [109].

3 Tandems

The limited optical response of single-junction cells stems from the absorption of a small fraction of photons above the bandgap of the semiconductor material, while excess energy is lost through thermalization and lower energy photons cannot be utilized. Currently, perovskite materials with excellent optoelectronic properties and tunable bandgaps are entering two-terminal (2T) tandem solar cells (TSCs), in which the WBG cells at the top can efficiently utilize high-energy ultraviolet and blue-green visible light, and the NBG cells at the bottom, including semiconductor materials such as crystalline silicon (c-Si), copper indium gallium selenide (CIGS) and narrow- E_g organic semiconductors and PSC, can effectively utilize low-energy infrared light. Therefore, integrating these high-efficiency subcells with tandem technology can break the S-Q limit of traditional single-junction cells and achieve the maximum utilization of the solar spectrum [112]. In this section, recent research progress about 2T perovskite/c-Si, perovskite/CIGS, perovskite/perovskite (all-perovskite) and perovskite/organic monolithic TSCs is reviewed.

3.1 Perovskite/c-Si tandem solar cells

With a high market share ($\approx 95\%$), excellent module efficiencies, and long-term reliability, c-Si is an ideal candidate for a tandem integration with PSC, and the front-side structure of c-Si is of concern as it does not only affect the crystalline quality of the perovskite but also the light-harvesting of the cell. Several thin film deposition techniques, such as spin coating, blade coating, evaporation, slot-die coating, have been developed to achieve more efficient and area-scaled perovskite/c-Si TSCs (Figure 11), which undoubtedly drive the commercialization of tandems.

3.1.1 Spin coating

(1) n-i-p perovskite/front-polished c-Si tandems

Compatible with the existing relatively mature solution manufacturing process of single-junction PSCs, the spin coating has become the most commonly used method to prepare top PSCs on single-side-polished c-Si cells for TSCs. In 2015, Mailoa et al. [113] reported the first n-i-p perovskite-based TSC with a PCE of 13.7% on an active area of 1 cm^2 , opening up a pathway for a tandem field. Limited by the parasitic absorption of spiro-OMeTAD in the short wa-

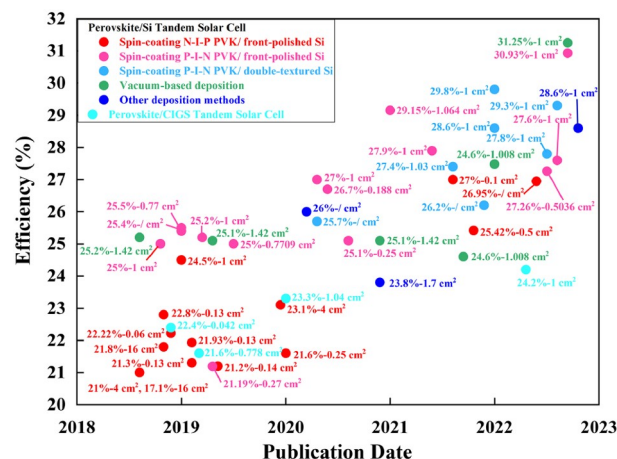


Figure 11 PCE evolution of perovskite/c-Si and perovskite/CIGS TSCs from 2018 to 2022 (color online).

velength (below 420 nm), the TSC based on n-i-p PSC develops slowly. In 2018, Sahli et al. [114] demonstrated a nanocrystalline Si recombination junction instead of TCO to reduce parasitic absorption and reflection losses, and the photocurrent of heterojunction cells increased by more than 1 mA cm^{-2} , resulting in a PCE of 22.7% at 0.25 cm^2 and 18% at 12.96 cm^2 . Qiu et al. [115] reported that 22.22% TSC can achieve current matching between subcells by optimizing the optoelectronic properties of the ETL and adjusting the bandgap and thickness of the perovskite absorber. Zhu et al. [116] also demonstrated 22.8% perovskite/c-Si TSC with appropriate light absorption and transmittance through solvent optimization. Zheng et al. [117] fabricated the first monolithic perovskite/c-Si TSC without an additional interfacial layer, the $\text{SnO}_2/\text{p}^{++}\text{Si}$ interface provides good vertical conduction between the top and bottom cells, enabling a PCE of 20.5% at 4 cm^2 and 17.1% at 16 cm^2 , the highest efficiency among TSCs larger than 1 cm^2 at that time. By using the new front top metal grid design, the steady-state efficiency of 21.8% was further achieved in the same group at 16 cm^2 [118]. During the same period, Shen et al. [119] reported a similar scheme using atomic layer deposition (ALD)-deposited TiO_2 instead of SnO_2 to achieve a PCE 24.1% for the passivating contact heterojunction tandems, demonstrating the broad applicability of the interlayer-free concept in perovskite/c-Si tandem design. Hou et al. [120] boosted perovskite/c-Si TSC from 19.38% to 21.93%, thanks to improved light absorption by introducing the light management antireflective foils made of polydimethylsiloxane polymer. Hou et al. [121] improved the perovskite film quality for top cells by Cs doping, combining the optimization of hydrogen-to-silane dilution ratio and substrate temperature during deposition of the intrinsic amorphous silicon (a-Si) layer, and the 21.3% perovskite/c-Si TSC with a high V_{OC} of 1.83 V was achieved. Bett et al. [122] applied the $\text{FA}_{1-x}\text{Cs}_x\text{Pb}(\text{I}_{1-y}\text{Br}_y)_3$ composition with 25% Cs and 20% Br

for efficient PSCs with a bandgap of 1.7 eV, and the corresponding perovskite/c-Si TSC PCE was increased to 21.6% (0.25-cm² active area) with a high V_{OC} of 1.85 V. To reduce the current output loss, Zheng *et al.* [123] added a downshifting material (Ba, Sr)₂SiO₄:Eu²⁺ micron phosphor to the antireflection film to convert near-ultraviolet light into visible light for perovskite absorption instead of parasitic absorption in the spiro-OMeTAD layer, boosting monolithic perovskite/c-Si TSC (4 cm²) efficiency from 20.1% to 23.0%, with improved ultra-violet (UV) stability and moisture resistance. In 2021, Chen *et al.* [124] developed a SnO₂-LiCl composite ETL for n-i-p perovskite/c-Si TSCs, in which LiCl passivated SnO₂ surface defects, increased the conductivity of SnO₂, and optimized the energy level alignment, resulting in a 1.68 eV perovskite-based TSC with an enhanced V_{OC} of 1.92 V and a PCE of 25.2%. Aydin *et al.* [125] developed C₆₀ anchored the a-NbO_x electron-selective layer on double-side textured silicon cells to enhance electron extraction, enabling efficient perovskite/c-Si TSC with a high PCE of 27% in the n-i-p configuration. Wang *et al.* [126] used adenosine triphosphate to convert the residual tensile strain in wide- E_g perovskite absorber into compressive strain, thereby mitigating light-induced ion migration and phase segregation, and achieved a PCE of 26.95% for n-i-p wide- E_g perovskite-based TSC.

(2) p-i-n perovskite/front-polished c-Si tandems

TSCs based on p-i-n PSCs have unlimited potential for further development, where the light-incidence surface is C₆₀ with less parasitic absorption compared to n-i-p type PSCs. Currently, the strategies to improve the PCE of perovskite/c-Si TSCs mainly focus on addressing optical loss, fill factor (FF) loss, current mismatch, and V_{OC} loss. To improve light harvesting, Jošt *et al.* [127] proposed the textured light management foil on the front side and Bush *et al.* [128] introduced a thin top transparent electrode with metal fingers, enabling a PCE of TSC over 25%. Kim *et al.* [129] developed p-i-n PSCs on p-type c-Si which is compatible with c-Si industry-standard high-temperature processes. Current matching was achieved by controlling the bandgap and thickness of perovskite, and the energy band alignment was adjusted to reduce V_{OC} loss by using PTAA as the HTL, resulting in a PCE of 21.19%. Chen *et al.* [130] improved the quality of perovskite grains through the synergistic effect of the MAI and MAH₂PO₂ additives, resulting in a PCE of 25.4% for perovskite/c-Si TSC. As reported by Köhnen *et al.* [131], through top contact and perovskite thickness optimization, the J_{SC} was increased to more than 19.5 mA cm⁻² enabling a TSC PCE of 26.0%. Mazzarella *et al.* [132] introduced the nanocrystalline silicon oxide as an interlayer between c-Si and PSCs, leading to an increased J_{SC} in the bottom cell, reaching a certified PCE of 25.2%. In 2020, the self-assembled methyl-substituted carbazole monolayer was proposed as the hole selection layer for PSCs. Due to rapid

hole extraction and minimal interface non-radiative recombination, the certified PCE reached 29.15% with the V_{OC} of up to 1.92 V [133]. Köhnen *et al.* [134] first fabricated PSCs on the industrial unpolished 100 μ m Czochralski c-Si, achieving a PCE of 27.9% for perovskite/c-Si TSC, which requires a perovskite bandgap higher than 1.7 eV for current matching. Recently, Wu *et al.* [135] reported a PSC on the industrial bottom c-Si cell with TOPCon structure for the first time and achieved a PCE of 27.6% of TSC at 1 cm². Undesirable photoinduced phase separation is prone to occur in the wide- E_g perovskites, especially when the Br fraction at the X-site is >20%. In 2020, Schulze *et al.* [136] developed MA-free and Cs-rich compositions for improving thermal and photostability of wide- E_g PSCs and also tuned the concentration of perovskite precursors to increase light absorption, reaching 25.1%-certified PCE with a FF of 80% for the TSC. Kim *et al.* [137] focused on the anionic components of phenethylammonium-based 2D additives, and the 2D/3D mixed wide- E_g perovskite was developed by using the mixture of thiocyanate and iodine, improving the light stability, and achieved a PCE of 26.7% for TSC. Xu *et al.* [138] reported a 27% TSC with an area of 1 cm², triple-halide alloys (chlorine, bromine, iodine) were incorporated into perovskite to enlarge the bandgap and alleviate the photo-induced phase separation of wide- E_g PSCs caused by excessive Br. Li *et al.* [139] also reported that adding 3 mol% CsPbCl₃ clusters to the perovskite precursor solution can expand the perovskite bandgap to 1.67 eV at Br content below 15%, thereby alleviating the photoinduced phase separation of wide- E_g perovskites. In combination with the additional 2 mol% CsCl to prevent redox reactions at the NiO_x/perovskite interface, the PCE of p-i-n perovskite/c-Si TSC was as high as 27.26%.

(3) p-i-n perovskite/double-textured c-Si tandems

Front-side polished c-Si bottom cells involve additional processing costs and high reflectance, and are usually paired with anti-reflection foils that might be compromised after encapsulating. To tackle these issues, industry-compatible double-sided textured c-Si is concerned, while higher quality spin-coated PSCs were desired. In 2020, Hou *et al.* [140] fabricated micron-thick PSCs by spin coating on textured c-Si with an average pyramid size of 2 μ m. The depletion width at the c-Si pyramid base was increased by threefold to improve charge collection, and the perovskite surface was passivated by self-limiting 1-butanethiol to obtain a long diffusion length and suppress phase separation, thus resulting in a certified PCE of 25.7%. Isikgor *et al.* [141] proposed a multifunctional passivation molecule, *i.e.*, phenformin hydrochloride, with electron-rich and electron-poor moieties that can simultaneously passivate cation and anion defects at grain boundaries and surfaces of perovskite, achieving a V_{OC} gain of 100 mV, and the PCE of the textured perovskite/c-Si TSC was boosted from 25.4% to 27.4%. Ruthenium-based

metal-organic dye molecules (N719) were reported to passivate the Ni^{3+} and O-dangling bond defects of NiO_x while forming a favorable energy alignment to enhance the hole extraction and transport from perovskites, which promotes the textured perovskite/c-Si TSC with a PCE up to 26.2% [142]. Zheng *et al.* [143] reported a photo-activated p-type PTAA doping with DPI-TPFB to enhance the hole extraction on textured c-Si, achieving a *FF* of 79.6% and a PCE of 27.8% for perovskite/c-Si TSCs. An evaporated MgF_x layer (~ 1 nm) was inserted at the perovskite/ C_{60} interface to reduce nonradiative recombination and facilitate charge extraction, achieving an ultra-high TSC PCE of 29.3% at $\sim 1 \text{ cm}^2$ [144]. In 2022, the researchers from Helmholtz-Zentrum Berlin (HZB) demonstrated a monolithic perovskite/c-Si TSC with an independently certified PCE of 29.80%, in which gentle sinusoidal nanotextured c-Si surface was formed to enable feasible light management without compromising the quality of perovskite films, and a reflector with a dielectric buffer layer was applied on the back side of the bottom c-Si cell to reduce parasitic absorption at near-infrared wavelengths [145]. Very recently, the researcher from École Polytechnique Fédérale de Lausanne (EPFL) broke the perovskite/c-Si TSC world record with a PCE of 31.25% [2].

In terms of the application scenarios, the outdoor performance of the TSC is concerned. Liu *et al.* [146] demonstrated a certified efficiency of 28.2% for a TSC over an area of about 1 cm^2 , enabled by defect passivation and suppressed phase segregation of the carbazole additive, and the encapsulated device maintained about 93% of their performances in a hot and humid outdoor environment over 43 days. De Bastiani *et al.* [147] studied the diurnal and long-term evolution of the encapsulated bifacial perovskite/c-Si TSCs in a hot and humid outdoor environment over six months. The results indicated that the degradation of device performance is due to the ion migration within the perovskite, while the interfacial modification is responsible for the reversible *FF* change, and the irreversible loss of the *FF* is associated with corrosion of the Ag metal top contact.

3.1.2 Vacuum-based deposition

The vacuum-based deposition is more tolerant to pyramid dimensions than spin-coating processes, favoring conformal and uniform film growth, and thus particularly attractive for efficient TSC processing. In 2018, Nogay *et al.* [148] proposed the conformal depositing perovskite absorbers on micrometer-scale c-Si pyramids by co-evaporation of CsBr and PbI_2 and subsequent spin-coating organic halide solutions to achieve optimal light management, yielding a PCE of 25.4% at reverse scans. Sahli *et al.* [149] used the same hybrid two-step deposition method to yield conformal perovskite absorber layers on textured c-Si bottom cells with a pyramid height of $\sim 5 \mu\text{m}$, and a nanocrystalline Si re-

combination junction was applied between the two subcells to provide a high resilience to shunts. A fully textured perovskite/c-Si TSC showed a PCE of 25.2%. Aydin *et al.* [150] fabricated 25% textured perovskite/c-Si TSC by evaporation combined with spin coating technique, followed by investigation of device stability in a hot and sunny outdoor climate. The results suggested that the optimal perovskite bandgap should be less than 1.68 eV at operational temperatures over 55°C , which features less phase stability. Li *et al.* [151] combined evaporation- and solution-processed techniques to conformally grow p-i-n perovskites on textured HJTs. The thermally evaporated CsBr thin layer was introduced to react with the residual PbI_2 at the buried perovskite interface to achieve favorable energy level alignment, achieving a TSC PCE of 27.48% with the long-term stability exceeding 10,000 h in nitrogen environment. Mao *et al.* [152] employed a NiO_x /2PACz hybrid HTL on fully textured, production-line compatible Si wafers to reduce shunt losses and match band alignment, achieving a 2T perovskite/Si TSC with a PCE of 28.84% at an active area of 1.2 cm^2 . The hybrid process is subjected to the insufficient reaction of organic and inorganic components, which still limits the application of large-area perovskite/c-Si TSC. In 2021, Roß *et al.* [153] first reported a monolithic fully textured perovskite/c-Si TSC based on one-step co-evaporation of the $\text{MA}_{0.5}\text{FA}_{0.63}\text{PbI}_{3.13}$ perovskite absorber, achieving a PCE of 24.6%. However, all-evaporation perovskite-based TSC was barely reported, which is likely attributed to complex components and instability of perovskite from process-induced damages.

3.1.3 Other deposition methods

Compared with vacuum-based deposition, blade coating and slot-die coating are more suitable for large-scale perovskite film deposition, although only a few reports involve tandem structures. Subbiah *et al.* [154] used slot-die coating to fabricate perovskite on textured c-Si bottom cells. Several strategies, including a low-boiling point mixture instead of only DMF for rapid solvent evaporation, the additive L- α -phosphatidylcholine for good wettability of the ink on PTAA, and perovskite surface defect passivation of cysteine hydrochloride, enabling the TSC with a PCE of 23.8%. In 2020, Chen *et al.* [155] first fabricated a conformal HTL and a thick perovskite layer on a double-textured HJT cell with sub-micrometer pyramids by a nitrogen-assisted blading process, combined with a textured light scattering layer on top to reduce light reflectance, leading to a 26% PCE of perovskite/c-Si TSC. Recently, this group fabricated μm -thick wide- E_g perovskite films on textured c-Si bottom cells with an average pyramid size of $0.43 \mu\text{m}$ by a blade coating method, and the incorporation of trimethylphenylammonium tribromide contributed to the high-quality thick perovskite films by suppressing the deep traps induced by iodide in-

terstitials and increasing the carrier collection distance, resulting in a PCE of up to 28.6% and a V_{OC} of 1.92 V for perovskite/c-Si TSC [156].

3.2 Perovskite/CIGS tandem solar cells

CIGS with tunable bandgap up to ~ 1.1 eV are suitable as bottom cells in tandem structures, despite relatively lower efficiency than that of perovskite/c-Si TSC (Figure 11). Perovskite/CIGS TSC can be used in flexible photovoltaic modules and satellite technology in space due to advantages of portability and radiation resistance, which has the impetus for further development.

Todorov *et al.* [157] reported the first monolithic perovskite/CIGS TSC with a PCE of 10.9% in 2015. ITO was used as the interconnection layer to connect solution-processed CIGS cells with p-i-n PSCs and ZnO was removed to alleviate perovskite instability. Possibly due to the small market share of CIGS and the challenge of depositing perovskites on rough CIGS cell surfaces, perovskite/CIGS TSC development is sluggish. Until 2018, Han *et al.* [158] made remarkable progress, raising the PCE of perovskite/CIGS TSC to 22.4%, which was promoted by specially depositing thickened 300 nm ITO on the rough surface of CIGS for localizing shunting and subjected by chemical mechanical polishing to facilitate subsequent perovskite deposition. Nevertheless, the additional cost of the polishing process cannot be ignored. To address surface roughness of CIGS, Jošt *et al.* [159] employed a ~ 10 nm NiO_x layer by ALD to form a conformal coating on CIGS cells, compatible with perovskite processes without polishing, combined with a PTAA layer to assist carrier transport, achieving a steady-state PCE of 21.6% at 0.8 cm^2 . Al-Ashouri *et al.* [160] employed self-assembled monolayers MeO-2PACz on top of ZnO-capped rough CIGS subcells to obtain a conformal coating, yielding a certified PCE of 23.3% on 1 cm^2 area. In 2020, the same group further reported a new certified record efficiency of 24.2% with a high V_{OC} value of 1.77 V for perovskite/CIGS TSC, which was enabled by a Me-4PACz monolayer as the hole transport layer, a wide 1.68 eV bandgap perovskite with PEAi dopant and LiF passivation interlayer [161].

3.3 All-perovskite tandem solar cells

All-perovskite TSCs show great potential due to the ultra-high efficiency, ease of low-temperature fabrication processes, compatibility with flexible substrates, and low cost [2,162]. The realization of all-perovskite TSCs highly relies on the broad bandgap tunability of perovskites, *e.g.*, wide- E_g (~ 1.7 – 1.8 eV) perovskite as top subcell absorber and narrow- E_g (~ 1.2 – 1.3 eV) perovskite as bottom subcell absorber [163]. In recent years, all-perovskite TSCs have been re-

markably developed and achieved high efficiencies of 28.0% (certified) and 26.1% for 2T and four-terminal (4T) configurations, respectively [2,164]. Such great progress has benefited from the following sections: (i) compositional and interfacial engineering of wide- E_g perovskites and devices; (ii) fabrication of highly efficient narrow- E_g PSCs with high J_{SC} ; (iii) employment of effective interconnection layers (ICLs).

3.3.1 Wide- E_g perovskite top subcells

Wide- E_g perovskites (~ 1.7 – 1.8 eV) typically contain high Br content, which accelerates the crystallization rate of perovskites, thus leading to small grains and a high density of defects at the grain boundaries. However, large V_{OC} deficits (defined as $E_g/q \cdot V_{OC}$) for wide- E_g PSCs are not only attributed to the nonradiative recombination in the bulk and at the interface but also to photoinduced phase segregation and mismatched energy levels between wide- E_g perovskites and CTLs. Many efforts such as compositional engineering, interfacial engineering, and dimensional engineering, have been devoted to improving the V_{OC} and stability of wide- E_g PSCs.

Paetzold's group [165] adopted *n*-butylammonium bromide (BABr) post-treatment on the surface of 1.72-eV $\text{FA}_{0.83}\text{Cs}_{0.17}\text{Pb}(\text{I}_{0.6}\text{Br}_{0.4})_3$ perovskites to create a 2D/3D perovskite heterostructure interface, which mitigated the non-radiative recombination, leading to an impressive V_{OC} of 1.31 V (Figure 12a). Therefore, the elimination of interfacial defects is beneficial to the V_{OC} improvement of wide- E_g PSCs. Chen *et al.* [166] utilized guanidine bromide (GABr) to treat the surface of 1.75-eV $\text{FA}_{0.8}\text{Cs}_{0.2}\text{Pb}(\text{I}_{0.7}\text{Br}_{0.3})_3$ perovskite, and the main junction dominated at the perovskite/ C_{60} interface effectively decreased the dark current (Figure 12b). A V_{OC} deficit of 510 mV was obtained with decent stability, which verified the efficacy of interfacial passivation to increase the V_{OC} .

Additionally, a proper CTL with matched energy levels with those of wide- E_g perovskites could reduce the V_{OC} loss. Tan's group [167] reported an *in-situ* cross-linked small molecule N_4,N_4' -di(naphthalen-1-yl)- N_4,N_4' -bis(4-vinylphenyl)biphenyl-4,4'-diamine (VNPB) instead of PTAA as HTL in 1.77-eV PSCs (Figure 12c). Compared with the valence band maximum (VBM) of PTAA, the deeper VBM of -5.3 eV for VNPB is more conducive to the hole extraction and transport from the perovskite layer, which thus obtained a higher V_{OC} of 1.23 V. Very recently, a new HTL combination of a mixed composition of MeO-2PACZ and 2PACZ on NiO was also fabricated to achieve a PCE of 16.2% with a V_{OC} of 1.22 V for ~ 1.75 eV wide bandgap PSCs [168].

More importantly, the suppression of phase segregation mainly depends on the compositional engineering of wide- E_g perovskites. Recently, Wen *et al.* [169] lowered the Br content of wide- E_g (~ 1.8 eV) perovskites by alloying dimethylammonium (DMA) and chloride (Cl) into the perovskites.

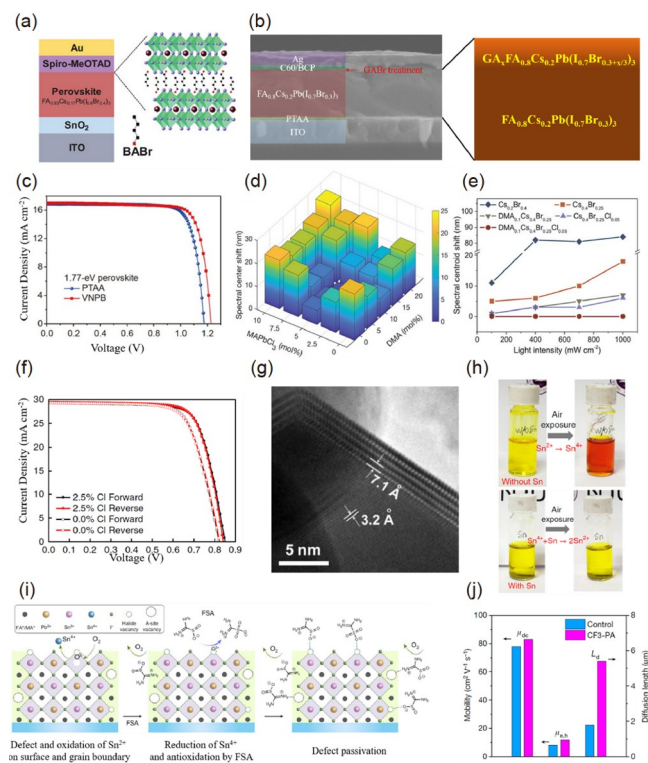


Figure 12 (a) Device structure with BAPr treatment [165]. (b) Cross-sectional SEM image with GABr treatment [166]. (c) J - V curves based on different HTLs [167]. Shift of PL spectral centroids of (d) $\text{DMA}_x\text{Cs}_{0.4}\text{Br}_{0.25}\text{Cl}_{1-x}$ perovskite films, and (e) $\text{DMA}_x\text{Cs}_{0.4}\text{Br}_{0.25}\text{Cl}_{1-x}$ and $\text{Cs}_{0.2}\text{Br}_{0.4}$ films [169]. (f) J - V curves of the best-performing PSCs for 0.0% and 2.5% Cl-doped absorbers [170]. (g) HRTEM image of the grain boundary region of perovskite with 7% GASCN additive [171]. (h) Photographs show the ease of oxidation of Sn^{2+} to Sn^{4+} in ambient air and the facile reduction of Sn^{4+} to Sn^{2+} by metallic Sn powders [172]. (i) Schematic illustration of anti-oxidation and defect passivation at grain surfaces of narrow- E_g perovskite films [173]. (j) Mobilities and diffusion lengths of the CF_3 -PA and control narrow- E_g perovskite films [162] (color online).

The lattice strain and trap densities were simultaneously minimized, and meanwhile, the phase stability was improved (Figure 12d, e), which confirmed the phase segregation could be effectively inhibited *via* compositional engineering.

3.3.2 Low- E_g perovskite bottom subcells

The bowing effect in mixed Sn-Pb perovskites makes the E_g as low as approximately 1.2 eV, which is suitable to absorb the near-infrared NIR light as a bottom subcell absorber [174]. However, numerous defects in the bulk and at the surface as well as the easy oxidation of Sn^{2+} to Sn^{4+} hinder the performance improvement of all-perovskite TSCs. Thus far, many strategies have been proposed to address these issues *via* defect passivation at the surface and in the bulk, modulation of the crystallization process, and inhibition of Sn^{2+} oxidation.

Zhao *et al.* [170] employed a bulk-passivation strategy *via* Cl incorporation to enlarge grain size and reduce electronic disorder in the perovskite film. The champion device with

2.5% Cl showed an improved PCE of 18.4% (Figure 12f), which was ascribed to increased mobility and suppressed nonradiative recombination. To obtain high-quality thick narrow- E_g perovskite absorbers, Zhu *et al.* [171] introduced guanidinium thiocyanate (GASCN) into the perovskite precursor, which dramatically improved the structural and optoelectronic properties of 1.25-eV Sn-Pb perovskite films. A 2D perovskite formed at the grain boundaries passivated the defects at grain boundaries and surfaces (Figure 12g), leading to prolonged carrier lifetimes of over 1 μs for the ~ 1 μm -thick perovskite film. Consequently, a PCE of >20% was achieved for $(\text{FASnI}_3)_{0.6}(\text{MAPbI}_3)_{0.4}$ PSCs. The efficiency was further elevated to 22.1% by additive engineering of mixed bulky organic cations [175].

Suppressing Sn^{2+} oxidation to Sn^{4+} is another helpful way to boost the efficiency and stability of narrow- E_g PSCs. Tan's group [172] developed a comproportionation reaction utilizing Sn powers and oxidized Sn^{4+} to produce the desired Sn^{2+} in the precursor (Figure 12h), which could effectively enhance the carrier diffusion length in narrow- E_g perovskites to 3 μm . Further, a strong reductive surface-anchoring zwitterionic antioxidant was added to the perovskite precursor to inhibit Sn^{2+} oxidation and passivate defects at the grain surfaces (Figure 12i), which enables simultaneous enhancements in the film uniformity, device efficiency and stability [173]. Additionally, they used 4-trifluoromethylphenylammonium passivator to passivate more defects adsorbed on the surface-defective sites *via* a strong perovskite surface-passivator interaction (Figure 12j) [162]. As a result, the carrier diffusion length in the perovskites with a thickness of ~ 1.2 μm reached over 5 μm , which enabled a PCE of over 22% for narrow- E_g PSCs.

Recently, Zhao's group [176] developed a universal close space annealing (CSA) strategy compatible with perovskites with various compositions and bandgaps to control the crystallization process of perovskites by slowing down the solvent releasing process in the intermediate film, and got the residual solvents involved into the grain growth process during annealing.

3.3.3 ICLs for all-perovskite TSCs

ICLs play a pivotal role in electrically and optically connecting both subcells to construct all-perovskite TSCs. The primary requirements for effective ICLs with high transmittance, appropriate electrical conductivity, and full protection of the underlying top subcell are highly met. As shown in Figure 13a, bathocuproine (BCP)/Ag/MoO_x/ITO/PEDOT:PSS ICL was employed [170], in which ITO prevented aqueous PEDOT:PSS and organic solvents from penetrating the existing layers. BCP/ITO/PEDOT:PSS could act well as an ICL to solve the possible instability caused by the ultrathin Ag [171].

ALD processed SnO₂ was adopted to replace the BCP

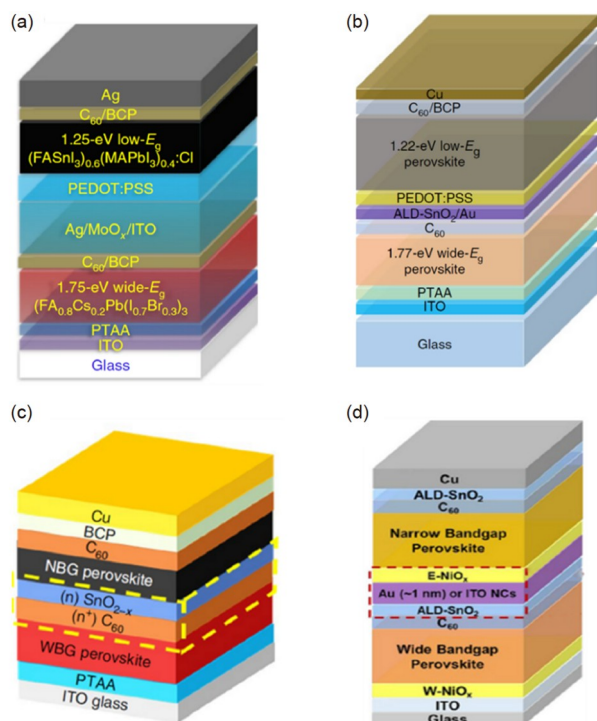


Figure 13 Device structures of 2T all-perovskite TSCs with different ICLs: (a) BCP/Ag (1 nm)/MoO_x/ITO/PEDOT:PSS [170], (b) ALD-SnO₂/Au/PEDOT:PSS [63], (c) C₆₀/SnO_{1.76} [177], (d) ALD SnO₂/Au or ITO/E-NiO_x [178].

layer to more effectively prevent the damages caused by sputtering and the solvents. Sputtered TCOs have also suffered low NIR transmittance. Therefore, the SnO₂/Au (1 nm)/PEDOT:PSS ICL was further developed (Figure 13b), in which Au acted as the recombination center. Huang's group [177] demonstrated a simplified C₆₀/SnO_{1.76} ICL *via* removing both ITO and PEDOT:PSS for all-perovskite TSCs (Figure 13c), which they attributed to the ambipolar transport property of SnO_{1.76} simultaneously working as ETL and HTL for top and bottom subcells, respectively. In addition, the replacement of PEDOT:PSS with NiO_x deposited by e-beam evaporation further lowered the damage of solvents and improved the stability of TSCs (Figure 13d) [178].

3.3.4 All-perovskite TSCs

Benefiting from the rapid development of wide-E_g perovskite, narrow-E_g perovskite, and ICLs, all-perovskite TSCs have made great progress. Yan and Zhu *et al.* [171,179,180] achieved a PCE of over 25% for 4T all-perovskite TSCs by tuning the bandgap selection for both subcells and improving the film quality of both perovskite absorbers. A PCE of 26.01% was further obtained with the guidance of simulation [164], which is the highest value for 4T all-perovskite TSCs to date.

The fabrication of 2T all-perovskite tandems is more complicated than that of 4T all-perovskite tandems, leading

to slow progress in 2T all-perovskite tandems in the early stage before 2017. In 2018, Zhao *et al.* [170] first achieved an efficiency of ~21% for a 2T all-perovskite TSC with a 1.75-eV FA_{0.8}Cs_{0.2}Pb(I_{0.7}Br_{0.3})₃ top subcell and a 1.25-eV (FASnI₃)_{0.6}(MAPbI₃)_{0.4} bottom subcell. The PCE was further raised to 23.1% by adopting GASCN additive in (FASnI₃)_{0.6}(MAPbI₃)_{0.4} precursor to enhance the carrier lifetime and employing BCP/ITO/PEDOT:PSS ICL to improve the stability [171]. Tan's group [162,172,173] exploited a series of reductants and passivators, such as Sn powers, formamidine sulfinic acid, and 4-trifluoromethyl-phenylammonium, to inhibit the oxidation of Sn²⁺ and passivate the surface defects of narrow-E_g perovskite films, which greatly prolonged the carrier diffusion length to several microns. Thus, a certified stabilized PCE of 26.4% was obtained for a 2T all-perovskite TSC with a 0.049 cm² active area. Very recently, the highest certified PCEs of 2T all-perovskite TSCs with active areas of ~0.049 and ~1.0 cm² have been 28.0% and 26.4%, respectively (Figure 14a) [2]. Moreover, a mini-module of the all-perovskite tandem solar cell with an aperture area of 20 cm² with a certified 21.7% was also achieved [182]. In addition, flexible 2T all-perovskite tandems and tandem module have been demonstrated [168,182,183].

Although great progress of all-perovskite TSCs has been made, some critical issues and concerns should be addressed to approach their theoretical efficiency of over 40% [181] and commercialization in the near future (Figure 14b). Therefore, continuing efforts should be devoted in the following aspects. For wide-E_g perovskite top subcells, the suppression of phase segregation with suitable additives in the precursor, the selection of CTLs with matched energy levels, and interfacial passivation with functional molecules can facilitate high V_{OC} and excellent operational stability. For narrow-E_g perovskite bottom subcells, the inhibition of Sn²⁺ oxidation in the Sn-Pb perovskite films with antioxidants and reductants and the growth of thick (>1 μm) narrow-E_g perovskite absorbers with diverse surface passivators can prolong the carrier diffusion length and thus greatly improve the NIR spectral response. ICLs delivering the minimized optical and electrical losses should be designed and deposited. These accomplishments could promote the realization of ultrahigh-efficiency and stable all-perovskite TSCs. Scaling up fabrication techniques of the devices including doctor-

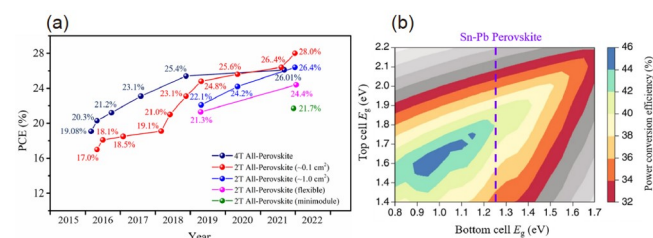


Figure 14 (a) Efficiency progress of all-perovskite TSCs; (b) theoretical simulation of perovskite-based TSCs [181] (color online).

blading, slot-die, and vacuum deposition for all functional layers should be meanwhile developed, in terms of commercial applications of all-perovskite TSCs.

3.4 Perovskite/organic tandem

Recently, perovskite/organic TSC has quickly drawn much attention and the main reason is the recently boosted PCE, which is benefitted from the developed NBG small molecule acceptor materials in organic solar cells (OSCs). The NIR absorbing organic photovoltaic materials provide excellent candidates for the rear cell active layers in TSCs. Moreover, in perovskite/organic TSCs, the short-wavelength UV light could be filtered by the perovskite front cell and the UV damage to the organic rear cell could be effectively mitigated. In order to achieve higher PCE of the perovskite/organic TSCs, the bandgap of WBG perovskite in front cell and NBG organic photovoltaic materials in the rear cell should be around 1.75 and 1.15 eV, respectively, according to the simulation (Figure 15a) [184]. Therefore, for further improving the performance of the perovskite/organic TSCs, the key points should be: (1) the reduction of the non-radiative charge recombination loss and the increase of the V_{OC} in the WBG perovskite front cell; and (2) the broadening of absorption spectral wavelength range and the improvement of photocurrent in the NBG organic rear cell.

Previously, many studies have demonstrated the possibility of perovskite/organic TSCs through device engineering. Liu *et al.* [185] combined a thin perovskite layer with an organic rear cell showing a similar optical absorption to boost light absorption. However, due to the significantly overlapped absorption range of perovskite and fullerene-based OSCs as shown in Figure 15b, the perovskite/organic TSCs showed very limited advantages. After the emergence of narrow bandgap small molecule acceptors (SMAs), the selection of organic donor:acceptor bulk-heterojunction (BHJ) rear cells became relatively abundant than before. For example, Aqoma *et al.* [186] matched the optical absorption of front cell based on CsPbI_2Br and rear cell based on PTB7-Th:IEICO-4F BHJ as the active materials, and a stabilized PCE of 18.04% was achieved. Li *et al.* [187] developed a perovskite/organic TSC with the phenethylammonium bromide passivated WBG perovskite (1.74 eV) as front cell and organic BHJ active layer of PBDB-T:SN6IC-4F (1.30 eV) as rear cell, which offered PCE of 15.13% (13.61% for flexible devices).

In 2019, the discovery of A-DA'D-A structured SMA Y6 significantly boosted the PCE of OSCs, and the NIR-absorbing property of Y6 also provides new opportunities for perovskite/organic TSCs. For instance, Xie *et al.* [188] demonstrated monolithic perovskite/organic TSCs with the WBG CsPbI_2Br perovskite as the front cell, and the NBG organic photovoltaic BHJ system of PM6:Y6 or PTB7-Th:

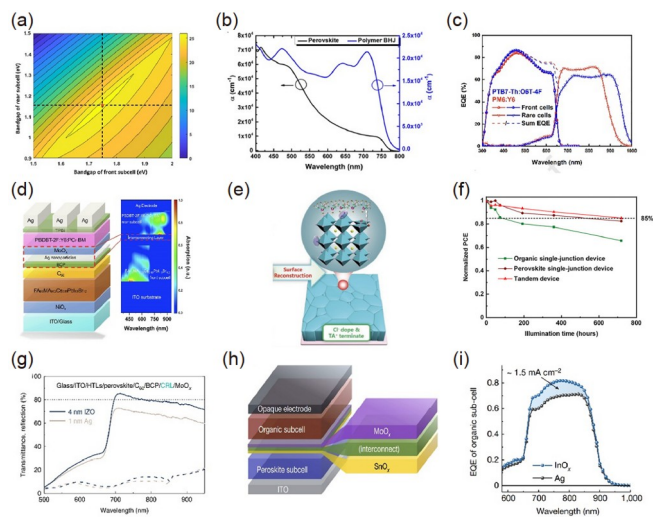


Figure 15 (a) Simulated optimal bandgap matching of the two subcells in the two-terminal monolithic perovskite/organic TSCs [184]. (b) UV-visible absorption of the modified MAPbI_3 -perovskite and $\text{PCE10:PC}_{71}\text{BM}$ BHJ film [185]. (c) External quantum efficiency (EQE) spectra of the corresponding TSCs [188]. (d) Device structure of the perovskite/organic TSC with organic rear cell based on $\text{PBDBT-2F:Y6:PC}_{71}\text{BM}$ [189]. (e) Schematic illustration of the TACl and IPA treatment [191]. (f) UV light soaking degradation test of the TSC devices [184]. (g) The transmittance spectra of the perovskite subcells with 4 nm IZO-based and 1 nm Ag-based ICLs [192]. (h) Schematic of perovskite/organic TSCs with InO_x or Ag as ICL and (i) EQE spectra of the corresponding TSCs [193] (color online).

O6T-4F as the rear cell. Eventually, through the optimization of the devices, the PM6:Y6 based TSCs exhibited PCE of 18.38% (Figure 15c). Chen *et al.* [189] built a semi-empirical device model for perovskite/organic TSCs and estimated the practical PCE limit of different combinations of perovskite materials and organic photovoltaic materials. Taking the model analysis into consideration, a ternary blend system of $\text{PBDBT-2F:Y6:PC}_{71}\text{BM}$ was selected as the rear cell and a wide bandgap $\text{FA}_{0.8}\text{MA}_{0.02}\text{Cs}_{0.18}\text{PbI}_{1.8}\text{Br}_{1.2}$ with E_g of 1.77 eV as the front cell. Eventually, the achieved p-i-n monolithic perovskite/organic TSCs showed a PCE of 20.6% with a certified value of 19.54% (Figure 15d). Later on, Xie *et al.* [190] optimized the mixed WBG perovskite films by introducing FA^+ cations into the composition of $\text{MA}_{1.06}\text{PbI}_2\text{Br}(\text{SCN})_{0.12}$, which modulated the crystallization and phase stability of the perovskite films. For the organic BHJ active layer, PM6:CH1007 was adopted with absorption extended to 950 nm. By further integrating the WBG perovskite front cell, the perovskite/organic TSCs achieved a PCE of 21.2%. Chen *et al.* [191] chose all-inorganic perovskite ($\text{CsPbI}_{1.8}\text{Br}_{1.2}$) as the photoactive layer of the WBG front cell for its intrinsically high thermal stability and UV-filtering function for protecting the organic rear cell. To realize the monolithic integration, the ICL between the two subcells was improved by surface reconstruction of all-inorganic perovskite using trimethylammonium chloride (TACl) as shown in Figure 15e. As a result, the all-inorganic perovskite/organic TSC

delivered a PCE of 21.04%, and more importantly, the TSC simultaneously shows outstanding operational and UV stabilities. Qin *et al.* [184] introduced chloro-formamidinium into WBG perovskite $\text{FA}_{0.6}\text{MA}_{0.4}\text{Pb}(\text{I}_{0.6}\text{Br}_{0.4})_3$ to passivate the bulk defects in the perovskite film and the WBG PSCs displayed high V_{OC} of 1.25 V and high FF of 83.0%. For the NBG OSCs, an NIR-absorbing organic SMA BTPV-4Cl-eC9 was designed and synthesized by inserting another ethylene double bond π -bridge between the DA'D central fused ring core and the A-end groups of Y-series SMAs. The absorption spectrum of the organic rear cell was broadened to over 1,050 nm. Eventually, the perovskite/organic TSC demonstrated a high PCE up to 22.0% and showed good operating stability under UV light (Figure 15f).

At the same time, efforts have also been devoted to the design and optimization of the ICL in the perovskite/organic TSCs to minimize optical and electrical losses. Chen *et al.* [192] demonstrated a high-performance ICL consisting of a sputtered 4-nm-thick indium zinc oxide (IZO) layer sandwiched between the BCP layer and MoO_x layer, resulting in a dramatic performance improvement compared with the ICL using BCP/Ag/ MoO_x . The reported IZO-based ICLs showed excellent NIR transmittance and minimized the current losses of the organic rear cell (Figure 15g). The ICLs enabled the perovskite/organic TSCs with high efficiency of 23.60% (certified as 22.95%). The tandem cell also shows high stability, maintaining 90% initial efficiency after 500 h maximum power point tracking under continuous 1-sun illumination. Later on, Brinkmann *et al.* [193] developed an ICL based on an ultrathin ALD-grown InO_x layer with a thickness of about 1.5 nm, to avoid the usage of a thin metal layer that would usually cause optical losses. The insertion of InO_x between SnO_x and MoO_x outstandingly improved the performance of the perovskite/organic TSCs (Figure 15h, i). As a result, a champion tandem cell with a stabilized PCE of 24.0% is achieved (certified as 23.1% by the Fraunhofer ISE CalLab).

4 Modules

Up to now, several groups have reported small-size PSCs achieving efficiencies over 25.0% [194], which is expected to exceed 26.0% in near future. However, small-size PSCs have little significance for industrial manufacture and actual applications. Thus, developing high-efficient large-area perovskite solar modules (PSMs) is an indispensable part for commercialization, and the performances of PSMs would determine whether PSCs can eventually be launched on market or not. For perovskite-only devices, large-area modules should achieve a PCE of 18% with a total area $\geq 125 \text{ cm}^2$, according to a report by the U.S. Department of Energy Solar Energy Technologies Office [195].

Undoubtedly, the fabrication of large-area PSMs is much more challenging than that of small-size PSCs. Firstly, uniform and high-quality function layers including ETL, HTL and photoactive layer (perovskite) should be deposited over a large area. In particular, the formation of perovskite films involves an unpredictable crystallization process in uncontrolled conditions, so if the process is lack of regulation, diverse defects and pinholes will result in serious non-radiative recombination and even short-circuiting. Secondly, to reduce the negative influence of film inhomogeneity and electric resistance for a large-area device, a series or parallel circuit is always implemented by separating the large-area device to several interconnected sub-cells. Only when employing appropriate module configuration and etching technology, efficiency loss could be reduced to the minimum. Centering on the above two challenges, some attractive progress has been made in recent years, which greatly promoted the development of PSCs toward commercialization.

4.1 Large-area function layers deposition

4.1.1 Perovskite layers

The preparation of perovskite layers is always the decisive part in the fabrication of high-performance large area PSCs. Due to the flexibility of preparation, various depositing techniques have been introduced to deposit large-area perovskite films. Solution methods include slot-die coating, blading coating, spray coating, inkjet coating, gravure coating, soft-cover deposition, pressure processing deposition, and vapor methods include co-evaporation deposition, chemical vapor deposition [196]. Among scalable solution methods, slot-die coating, blading coating and bar coating form meniscus-shaped liquid edges to spread precursor films across the substrate, and are classified as meniscus coating [197]. A slot-die coater consists of a slot-die head and a solution reservoir, so the precursor solution can be pumped into the coating head for continuous deposition. On the contrary, blade coating and bar coating have simpler structures, abandoning the solution reservoir, so their feasibility on operation attracts more attention of lab-scale scalable fabrication. Considering notable merits of meniscus coating, many groups have implemented them to deposit large-area perovskite films. Spray coating, inkjet coating, and gravure coating are already mature techniques for printing thin films, so they have been employed to deposit perovskite films [198,199]. In inkjet coating, precursor solutions are dispersed into droplets by nozzles in the coating head, and the size and trajectory of droplets can be controlled in printing. Spraying coating cannot control the size and trajectory of droplets accurately, but has higher coating efficiency. Some attempts have been made by employing both techniques. Schackmar *et al.* [200] achieved all-inkjet-printed PSCs except electrodes and obtained an efficiency of over 17%.

Eggers *et al.* [201] used inkjet coating to prepare high-quality perovskite layers with exceptional thicknesses over 1 μm , enabling high PCEs over 21% and stabilized power output efficiencies over 18%. “coffee rings” effect usually occurs in spray coating and inkjet coating, which heavily influences the homogeneity of solute distribution, resulting in high surface roughness and poor deposition. Consequently, the formation of “coffee rings” morphology is detrimental to the performances of PSC. Yu *et al.* [198] proposed an evaporation/spray-coating two-step deposition method to fabricate $\text{Cs}_{0.19}\text{FA}_{0.81}\text{PbI}_{2.5}\text{Br}_{0.5}$ perovskite films. To inhibit “coffee rings” effect, the solvent for the organic halide solution was changed from isopropanol to *n*-butyl alcohol (NBA). The lower evaporation rate of the NBA solution suppressed the capillary flows and increased the reaction between metal halides (CsI/PbI_2) and organic halides (FAI/Br). An enlarged perovskite film (10 cm \times 10 cm) containing 40 sub-cells was prepared by this method. The average PCE of these devices was 18.33% \pm 0.56%.

Moreover, some unconventional deposition methods have also been invented. Han group presented a soft-cover deposition method. The precursor solutions were spread out by polyimide (PI) films that had a good wettability to perovskite precursor solution. PI films can not only eliminate solute accumulation, but also control the solvent evaporation rate [202]. Through some careful optimizations, the novel method produced perovskite films with better coverage and facet orientation than spin coating method. A large-area film of 51 cm^2 was prepared, and PCEs up to 17.6% were achieved on working areas of 1 cm^2 . The soft-cover deposition method was also applied to two-step deposition [203]. PI films were placed on substrates to form capillaries, which helped to spread PbI_2 precursor solution, and absorbed MAI sequentially. A PCE of 15.5% on an area of 5 cm^2 and a PCE of 15.3% on a flexible PSC were achieved by this means. Furthermore, Han *et al.* [204] proposed a pressure processing deposition, where vacuum and solvent were all abandoned. They applied a pressure to spread a synthesized precursor slurry under a polyimide (PI) film (Figure 16a). When the film was assembled, by peeling off the PI film under a constant speed, a dense and uniform perovskite film was formed by releasing CH_3NH_2 gas. Notably, the new method can be implemented in ambient condition with a low temperature of 50 $^\circ\text{C}$. A certified PCE of 12.1% with an aperture area of 36.1 cm^2 was obtained.

To prepare high-quality perovskite films, nucleation rates and crystal growth rates of perovskite must be adjusted to meet the ideal crystallization process. According to LaMer model, when the precursor solution reaches a state above the minimum supersaturation concentration, the nucleus will start to form rapidly, while the quantity of the nucleus will further determine the quality of final films [205]. However, when using non-volatile solvents, like DMF and DMSO,

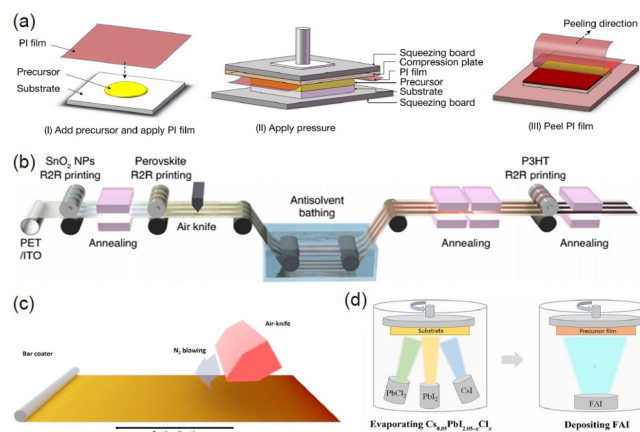


Figure 16 (a) Steps of the pressure processing method: (I) add amine complex precursors and cover with PI film; (II) apply pressure; and (III) heat and peel off the PI film [204]. (b) Diagram showing R2R processing for the fabrication of flexible PSCs [199]. (c) Diagram of an air-knife-assisted bar-coating [215]. (d) Diagram presenting the Cl-containing alloy-mediated sequential vacuum deposition approach [216] (color online).

natural evaporation of them is too slow to allow fast nucleation, thus hardly producing compact films. To handle the problem, several novel accessories are attached to original printing devices.

Anti-solvent bath extraction has been developed and could potentially be used in conjunction with roll-to-roll (R2R) coating fabrication techniques. Kim *et al.* [199] have developed a high-throughput R2R process, where an anti-solvent bath was employed to facilitate the nucleation and then convert precursor wet films to perovskite dry films. Different from commonly used anti-solvents, ethyl acetate (EA), chlorobenzene (CBZ), or *tert*-butyl alcohol (*t*BuOH) was introduced as an eco-friendly anti-solvent. Its lower miscibility with DMF and DMSO provides a wider processing window, which contributes to higher film quality and repeatability. With the advanced R2R-compatible processes, they demonstrated the manufacturing of printed pilot-scale PSCs (Figure 16b). R2R gravure-printing with *t*BuOH:EA bathing resulted in efficiencies of 16.7% for PSCs with R2R-processed SnO_2/FA -perovskite, and 13.8% for fully R2R-produced PSCs. Besides, Yang *et al.* [206] utilized *n*-hexane in an anti-solvent bath, and introduced a novel Lewis base additive, diphenyl sulfoxide (DPSO), into precursor solution. Benefiting from a well-balanced nucleation barrier, uniform large-area FACs perovskite films were blade coated, and the resultant PSM realized a certified efficiency of 16.63% with an active area of 20.77 cm^2 .

Blowing high-speed gas to accelerate solvent evaporation is another strategy to regulate large-area perovskite crystallization [207] (Figure 16c), and is becoming more and more popular because of its controllability and feasibility. Unlike the anti-solvent method, the gas-assisted strategy is more compatible with large-scale printing. Huang *et al.* [208] reported several work on blade coating large-area perovskite

films with the assistance of N_2 blowing. To reach a high supersaturation in a short time, they started to exchange DMF into volatile solvents, like 2-methoxyethanol (2-ME) and acetonitrile (ACN). By using 2-ME as solvent, and implementation of NH_4Cl in precursor solution, a record aperture efficiency of 15.86% on flexible modules with an area of 42.9 cm^2 was achieved by blade coating with N_2 blowing. Then, they found when using a mixture solvent composed of ACN and 2-ME, even by a high blading speed of 99 mm/s under ambient conditions high-quality large-area perovskite films can be produced [209], which is more suitable for high-throughout manufacturing. The corresponding PSM yielded a certified efficiency of 16.4%, with an aperture area of 63.7 cm^2 . It is considered that heterogeneous nucleation occurs during the gas-assisted drying process, thus the bottom interface property is extremely important. Huang *et al.* [86] tried to investigate the bottom interface morphology of perovskite film using a peeling technique that separated perovskite films from substrates. They found the change of bottom interface morphology was closely related to the amount of DMSO. Too less DMSO resulted in too many voids because of too quick crystallization, while too much DMSO also produced many interface voids. Therefore, even if an appropriate amount of DMSO was employed, it only got a PCE of 21.5%. When partially replacing DMSO with solid-state carbonylhydrazide that greatly reduced interfacial voids, through blade coating, mini-modules showed certified PCEs of 19.3% and 19.2%, with aperture areas of 18.1 and 50.0 cm^2 respectively.

On the other hand, vacuum pumping is also an effective method for regulating perovskite crystallization *via* accelerating solvent evaporation [210]. Ding *et al.* [211] and Gao *et al.* [212] employed pumping to prepare large-area perovskite films on flexible substrates. Dense and compact perovskite films were produced by promoting solvent removal. An attempt of fabricating large-area modules *via* gas pumping method has also been made. Cai *et al.* [213] successfully prepared $5\text{ cm}\times 5\text{ cm}$ perovskite film, which reached a PCE of 10.6%, and large modules of $45\text{ cm}\times 65\text{ cm}$ were also achieved.

As above mentioned, regulating the crystallization of precursor solution is one of the most critical parts in scalable fabrication. While Huang *et al.* [30] alternatively developed a ground-breaking printing method, in which NMP was added to perovskite ink to tune the type of nuclei. Due to the stronger interaction with PbI_2 , NMP prefers to form PbI_2 -NMP complex instead of perovskite-NMP complex. Thus, the nucleation is mastered by the PbI_2 -NMP. The fast nucleation of PbI_2 -NMP is apt to form dense films, and at the same time, FAI/CsI species are embedded surrounding PbI_2 -NMP, subsequently forming dense perovskite through an *in-situ* reaction. Thus, a certified 19.3% PCE mini-module with an aperture-area of 17.1 cm^2 was fabricated using slot-die

coating techniques.

Although solution methods have been overwhelmingly used to fabricate lab-scale devices and populate the NREL chart with highly-efficient PSCs, vapor methods are non-negligible because of their advantages in abandoning toxic solvents, offering good conformity to rough substrates and having mature manufacturing infrastructure. The PCE of the PSCs made *via* vapor methods has been significantly improved to 24.42% recently [216], which reveals great potential waiting to be tapped.

In single-source vapor deposition, Liang *et al.* [217] have prepared a large-area $MAPbI_3$ film with 100 cm^2 . Meanwhile, because of the high volatility of organic cations, the corresponding perovskite films commonly have poor morphology and optoelectronic properties, leading to low efficiencies. Borchert *et al.* [218] prepared uniform $FAPbI_3$ perovskite films over $8\text{ cm}\times 8\text{ cm}$ substrates by employing multi-source evaporation. Loading lead halides and organic halides in separated sources provided more accurate evaporation control, and the resultant PSC achieved a champion PCE of 14.2%. Furthermore, Yi *et al.* [216] employed sequential thermal evaporation deposition to perovskite films, firstly depositing PbX_2 precursor films and then FAI (Figure 16d). They found the addition of chlorine in the precursor film can promote the reaction between PbX_2 precursor and FAI, and produce the perovskite film with a stronger degree of preferential orientation and higher crystallinity. A champion PCE of 19.87% was gained by a mini-module with an aperture area of 14.4 cm^2 . The devices maintained 92% of the initial PCE after 450 h of aging under MPP tracking conditions.

Chemical vapor deposition (CVD) is also a scalable vapor method, with great potential in preparing large-area perovskite films. Qi *et al.* [219] have done plenty of research in this field and proved its scalability on a lab-scale. For instance, they co-evaporated $CsBr$ with PbI_2 in the first step, and Cs^+ and Br^- were demonstrated to accelerate the following reaction and improve phase stability. The module with a designated area of 91.8 cm^2 was prepared, obtaining a PCE approaching 10%.

4.1.2 ETL, HTL and electrodes

In n-i-p structures, metal oxide materials (e.g., TiO_2 , SnO_2 , ZnO , and Zn_2SnO_4) are usually used as ETL materials, which have great electrical and optical properties, and show high resistance to light, heat, and moisture. TiO_2 is a widely used electron transport material in PSCs. Various deposition methods have been used to prepare large-area TiO_2 , such as spray coating, screen printing and chemical bath deposition. Based on the TiO_2 ETL, the largest PSMs reached $3,600\text{ cm}^2$ [96], and a high efficiency of 17.1% was achieved on an area of 24.97 cm^2 by Jung *et al.* [55]. Moreover, some studies aimed to decrease annealing temperatures, so that TiO_2 can

be used in flexible substrates and also less energy consumption. For instance, Di Giacomo *et al.* [220] reported a large-area PSM which was based on an e-beam evaporated TiO_2 layer. With slot-die coating, a module with an active area of 151.875 cm^2 was realized and gained a PCE of 11.1%.

Recently, the SnO_2 ETL is becoming the mainstream choice for high-efficient PSCs. The SnO_2 ETL can be deposited by chemical bath deposition, and helps to achieve PCEs over 25% [214]. However, for scalable fabrication, integrating the printing process to the ETL fabrication is a rational strategy. Huang *et al.* [221] implemented a hot air blowing in slot-die coating SnO_2 nanocrystal film. With the advanced printing technology, a large-area ($5 \text{ cm} \times 6 \text{ cm}$) flexible PSM achieved an efficiency exceeding 15%. Kim *et al.* [222] used polyacrylic acid (PAA), a polymer binder, to optimize the arrangement of SnO_2 quantum dot (QD) on a textured surface (Figure 17a), with the corresponding large-area (64 cm^2) PSM reaching a PCE of 20.6%.

For HTL, spiro-OMeTAD is still the common choice, but considering the poor stability of conventional doping strategies with Li-TFSI and 4-*tert*-butylpyridine (*t*-BP), some novel small-molecule organic, organometallic materials and novel doping strategies have been utilized [223]. For instance, Hu *et al.* [224] simply replaced the usual chlorobenzene solvent with pentachloroethane, without any additional additives. An efficiency of 16.1% was achieved on an area of 1.00 cm^2 with improved stability. Xia *et al.* [225] reported a dopant (diphenyl iodide cation and pentafluorophenyl boric acid anion (DIC-PBA)) with diphenyl iodide cation and pentafluorophenyl boric acid anion was an alternative to Li-TFSI and *t*-BP. DIC-PBA can effectively dope PTAA and create a p-doping interface between perovskite film. Devices prepared with DIC-PBA yielded a high efficiency of 22.86%, and the modules reached an efficiency of 19.13% with an aperture area of 33.2 cm^2 (Figure 17b). Wu *et al.* [226] synthesized a small-molecule hole transport material, BTPA-7, which is almost half cheaper than spiro-OMeTAD. Meanwhile, it possessed higher hole mobility and higher glass transition temperature (T_g) than spiro-OMeTAD.

In p-i-n structures, HTL is deposited first. Wang *et al.* [227] proposed a strategy of depositing NiO_x nanocrystal films on flexible substrates by the R2R process. NiO_x nanocrystals were blade-coated on the substrate without obvious aggregation. Then a hydroiodic acid bath was employed to reduce Ni^{3+} to Ni^{2+} state, forming nickel iodide, which can strengthen interface charge transfer. A 15 cm^2 flexible perovskite solar module achieved a PCE of 16.15%. Du *et al.* [228] proposed a surface redox engineering to optimize vacuum-deposited NiO_x films. The surface redox engineering included an Ar-plasma-initiated oxidation process and a Brønsted acid-mediated reduction process, which promoted the origin surface to a more stable surface state,

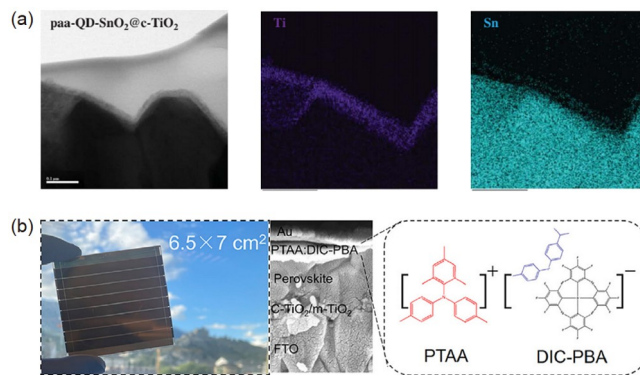


Figure 17 (a) The cross-sectional TEM images of paa-QD- SnO_2 @c- TiO_2 over the FTO substrates [222]. (b) A photograph of a sealed $6.5 \text{ cm} \times 7 \text{ cm}$ DIC-PBA-based solar module, and molecular structures of PTAA and DIC-PBA [225] (color online).

optimized conductivity, and better energy-band alignment. Then, they successfully implemented slot-die to deposit large-area perovskite films on the substrate. Perovskite sub-modules with an area of $156 \text{ mm} \times 156 \text{ mm}$ were successfully assembled, and achieved a remarkable PCE of 18.6% along with excellent stability.

Recently, more and more high-efficiency PSCs have used PTAA as HTLs but in a small size. The hydrophobic nature of PTAA results in poor wetting of the perovskite precursor, which is disadvantageous for eliminating pinhole defects at the PTAA/perovskite interface. To address this issue and aim for large-area devices, Deng *et al.* [229] introduced *l*- α -phosphatidylcholine into precursor solution, which enhanced the wettability of precursor solution on PTAA. Fabricated modules achieved efficiencies of 15.3% and 14.6% with aperture areas of 33.0 and 57.2 cm^2 , respectively.

As for ETLs, carbon materials (*e.g.*, carbon nanotubes, graphene, fullerene and its derivatives) provide continuous structure for charge transporting and are suitable for vapor deposition and solution deposition. As perovskite layers are susceptible to solvents present, C_{60} is generally deposited by thermal evaporation to construct p-i-n PSCs [86,208,209]. Deng *et al.* [229] thermally evaporated C_{60} on perovskite layers as ETLs in inverted planar PSCs, and the related module exhibited a certified PCE of 14.9% with an area of 57.2 cm^2 .

Au, Ag and Cu are usually thermally-evaporated to form metal electrodes of PSCs, as they have high conductivity, and related scalable deposition technologies are mature. Recent high-efficient PSMs still employed Au electrodes [214]. However, the high price and stability issues are not conducive to industrial development. According to an evaluation, Au electrodes will share 76.6% of material costs in PSCs [230]. In order to decrease the cost of metal electrodes, Ag and Cu are selected as cheaper substitutes. Chen *et al.* [86] evaporated Cu as electrodes of p-i-n PSCs and PSMs,

and efficiencies of 23.6% and 19.2% were achieved on a small-size device and a large-area PSM with 50.0 cm², respectively.

Meanwhile, poor stability caused by the metal diffusion still exists [231]. One strategy to eliminate the diffusion is to fabricate barrier layers. For instance, Agresti *et al.* [232] introduced a chemically functionalized MoS₂ interlayer between HTL and perovskite layer, which not only prevented atom diffusion but also optimized band alignment. Li *et al.* [233] deposited an organic corrosion inhibitor of benzotriazole (BTA) between ETL and Cu electrode in p-i-n PSCs. BTA molecules reacted with Cu of the electrode surface and formed an insoluble and polymeric film of [BTA-Cu], which can suppress ion diffusion and electrochemical corrosion. After 85 °C aging for over 1,000 h, over 90% of initial efficiency was retained, and after continuous maximum power point tracking for 1,000 h, 88.6%±2.6% of initial efficiency was retained. Moreover, in PSMs, a lateral atom diffusion at the interconnection between the sub-cells also needs high attention. Bi *et al.* [7] introduced three kinds of low-dimensional diffusion barriers, Al₂O₃ nanoparticles, polydimethylsiloxane (PDMS), and graphitic carbon nitride (g-C₃N₄), to compare their effects. They successfully reduced the diffusion coefficients to 10⁻³–10⁻⁷ times than that in perovskite films. With 2D blocking layers, modules maintained 95% of the initial PCE after damp heat test.

Another strategy is replacing metal electrodes by carbon materials that have low cost, better stability, and hydrophobic property [196]. Carbon electrodes are popular in the triple mesoscopic structure PSCs. Han *et al.* [95] fabricated mesoporous TiO₂/ZrO₂/carbon triple-layer PSMs, which showed a 10.4% PCE on an active area of 49 cm². In recent years, more attention has been put on using carbon electrodes on planar structure PSCs. Zhang *et al.* [234] achieved an efficiency of up to 19.2% on a small-size PSC. Zouhair *et al.* [108] reported that HTM-free PSCs reached efficiencies of 18.5% with a significantly improved device stability.

4.2 Modules design and process

The series connection is commonly performed by using three sets of scribe lines (P1, P2, and P3) to divide a large-area cell into several narrow sub-cells (Figure 18a). P1 is applied to cut off the charge transfer path on the bottom electrode. It should be noted that P1 makes the substrate uneven, so too close P1 scribe lines will lead to higher inhomogeneity. Meanwhile too few P1 scribe lines cannot effectively reduce the negative effect of sheet resistance of TCO. P2 aims to remove function layers, and intactly expose the covered TCO. Minimizing interconnect contact resistance between the top electrode and TCO is important for improving PCE. In P2, it should not damage the underneath TCO, but if leaving too many residues, series resistance will increase. P3

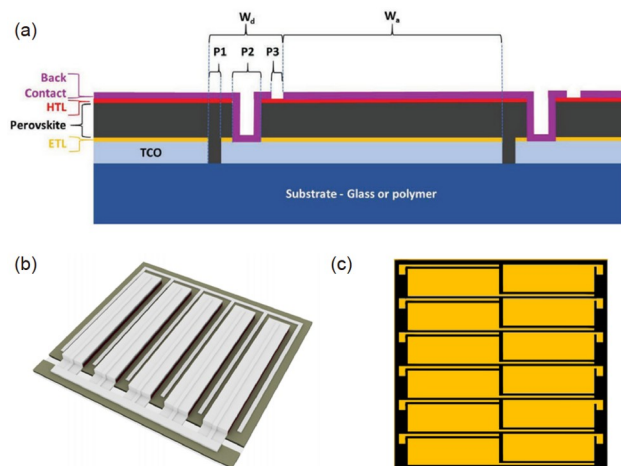


Figure 18 (a) Diagram of the series connection showing the P1-P2-P3 lines for a module. The “dead area” is indicated by W_d , and the active area by W_a [235]. (b) Diagram of the parallel connection [206]. (c) Diagram of combining series and parallel connections [227] (color online).

is employed to disconnect the horizontal charge transfer on the top [235]. Suitable P3 scribing results in no electrode fragments re-deposition in the scribe line, ensuring adequate top isolation.

Although the PSM connected in series can achieve an ideal voltage, it is still difficult to achieve a high current. Parallel connection, as a simpler connection structure, connecting the anode (cathode) of the sub-cell with the anode (cathode) of the adjacent sub-cell (Figure 18b), can sum the photo-generated current of all sub-cells. A successful strategy to make parallel connected modules is depositing metal grids directly on substrates, and then fabricating the functional layers. Yang *et al.* [206] fabricated PSMs with an advanced parallel configuration, where the width of Ag grids was 6 μm and a geometric fill factor (GFF) of 92.7% was achieved on an active area of 20.77 cm². Interestingly, some attempts on combining series and parallel connection together were proposed, as promising strategies for getting high and steady efficiency. Gao *et al.* [231] compared series and parallel connection, and found connecting series modules by the parallel connection was the best way for maximizing total output efficiency. Xu *et al.* [227] designed a new module configuration, where sub-cells in the same row were connected in series and all these rows were connected in parallel (Figure 18c). A PSM with a designated area of 21.06 cm² achieved a champion PCE of 18.81% with this new connection design.

In both series and parallel connections, the process of scribe lines is critical for obtaining high-efficiency modules. Various methods have been implemented in processing scribe lines, such as mask-guided methods, mechanical scribing, chemical scribing and laser scribing. However, with further research, laser scribing gradually replaces other scribing methods and is becoming the most popular one.

Firstly, laser scribing with high precision can produce thinner scribe lines, and produce PSMs with higher GFF. With less dead area, more active area can be used to convert solar energy under the same total area. For instance, Qi *et al.* [236] successfully produced a 5 cm×5 cm solar mini-module with a GFF of ~96% on an aperture area of 22.4 cm², achieving an efficiency of 20.5%. Rakocevic *et al.* [237] employed laser etching to achieve a point contact interconnection in series connection, and greatly improved the GFF up to 99%. Besides, laser scribing can produce smaller interconnection contact resistance, which is important for reducing the power loss in modules.

5 Stability

Lead halide PSCs are leading the revolution in photovoltaics thanks to their low cost and high efficiency. Although the certified PCE of PSCs is comparable to that of Si solar cells, the unsatisfactory stability hinders their further commercial applications [238]. Recently, the research community has focused on the stability of PSCs to achieve fruitful progress. In the following paragraphs, we briefly review the recent advances in three major aspects, namely, the device architecture, ion migration, and encapsulation. These cumulative understandings not only promote the technical development of perovskite PVs with commercially acceptable stability, but also shed light on the future research and design of hybrid crystalline materials for optoelectronic applications and beyond.

5.1 Functional layers

The most popular PSCs follow the basic configuration of thin film solar cells, wherein each functional layer is sequentially deposited to construct a full cell. The degradation in any single layer leads to the failure of the entire cell. To understand the stability of the entire cell, therefore, it is intuitive to probe the properties of individual components and their interaction. Here, we extend the following discussion to cover absorbers, passivators, carrier transport materials, and electrodes, with an emphasis on some key advances.

5.1.1 Absorbers

As ionic soft crystals [239] (Figure 19a), perovskite absorbers are susceptible to illumination, heat and electric bias, which will lead to deep-level defect formation, ion migration, phase segregation and chemical reactions. To mitigate the operational instability, significant efforts were witnessed to stabilize perovskite absorbers through various strategies, especially component engineering and additive engineering [240–243].

For lattice design and composition optimization, Gold-

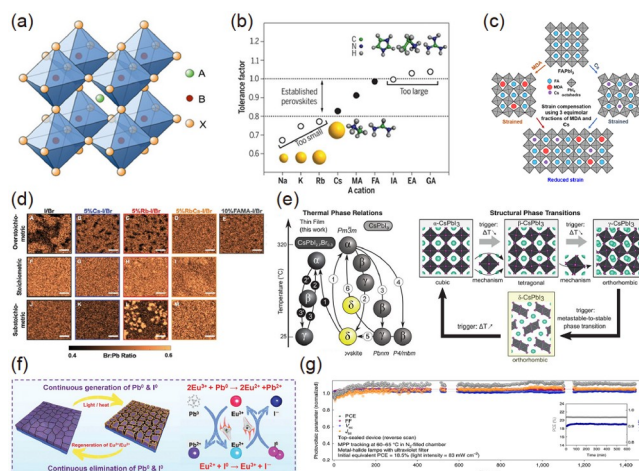


Figure 19 (a) Crystal structure of ABX₃-type metallic halide perovskites [257]. (b) Tolerance factor of APbI₃ perovskite with different A-site cations [258]. (c) Schematic illustration of the proposed distribution by incorporating the equimolar fraction of MDA and Cs cations within the perovskite crystal [248]. (d) X-ray fluorescence mapping indicates heterogeneous distribution of Br as a function of alkali metal incorporation and stoichiometric composition of the perovskite films [253]. (e) Polymorphic character and metastability of CsPbI₃ [259]. (f) Proposed mechanism diagram of cyclic elimination of Pb⁰ and I⁰ defects and regeneration of Eu³⁺-Eu²⁺ metal ion pair [32]. (g) The best long-term stability of the device tested at 60–65 °C under metal-halide lamps [251] (color online).

schmidt tolerance factor ($t = (R_A + R_X)/\sqrt{2}(R_B + R_X)$) is often used as an empirical index [244] (Figure 19b). The value in the range of 0.8–1 (*e.g.*, MAPbI₃) is favorable for perovskite structure; however MAPbI₃ suffers from thermal instability [244]. When t is larger than 1, (*e.g.*, FAPbI₃) or smaller than 0.8, (*e.g.*, CsPbI₃), corresponding perovskite structures are often unstable. Mixing cations with different radius to adjust t value is effective to stabilize photoactive perovskite phase. Cations with smaller radius such as Rb⁺ and Cs⁺ could be incorporated with larger FA⁺ to form stable alloyed perovskite [245–247]. Strain provides an alternative perspective to explain how mixing cations stabilized perovskite. For example, smaller radius Cs⁺ was used to release the strain induced by larger MDA²⁺ in FAPbI₃, and the resultant PSC can maintain over 90% of its initial efficiency after 600 h of MPP tracking [248] (Figure 19c). Similarly, large cations such as DMAI [249,250], were able to stabilize CsPbI₃ with smaller cations. Due to the complexity of alloy perovskite composition, a high-throughput screening platform was developed. It was found that FAMACs based perovskite alloy with specific ratio was thermodynamically stable. The corresponding devices retained 99% of its peak efficiency after 1,450 h of continuous operation at 65 °C (Figure 19g) [251].

Despite improved stability in alloyed perovskite [81,251,252], multiscale heterogeneity of composition might induce phase segregation and thus material degradation

[253–255] (Figure 19d). Strain engineering is also one important strategy to stabilize perovskite phase. For example, a rapid cooling process could induce interfacial clamping and strain in the absorber film, which stabilizes black phase of CsPbI_3 at room temperature (Figure 19e). Besides, strong coordination between additive and Pb^{2+} in perovskite also brings substantial lattice distortion. The resultant tetragonal phase of FAPbI_3 is photoactive and more stable than pure cubic FAPbI_3 [255].

In addition, it is popular to introduce additives during film growth to improve material stability. Ionic additives are widely investigated due to the ionic nature of perovskites. Commonly used MAI was incorporated to promote the intermediate α -phase FAPbI_3 , which suppressed detrimental δ -phase formation [11]. The introduction of ionic liquid BMIMBF_4 inhibits ion migration significantly [70], resulting in PSCs loss of only 5% PCE under full-spectrum sunlight for 1,800 h at over 70 °C. A piperidinium salt retarded compositional degradation and pinhole formation, and corresponding PSCs retain 95% of initial PCE under illumination at 85 °C for 1,200 h [69]. Formate (HCOO^-) was found to have a higher binding affinity towards iodide vacancy through coordination, compared with Cl^- , Br^- , I^- and BF_4^- [194]. In addition, fluorides were reported to form strong interaction with perovskite for phase stabilization [256]. PSCs with fluoride kept 90% of the initial PCE after 1,000 h MPP tracking. Moreover, perovskites also suffer from redox damage, where Pb^{2+} and I^- decomposed into Pb^0 and I^0 , respectively. A $\text{Eu}^{3+}/\text{Eu}^{2+}$ redox shuttle was introduced to continuously eliminate Pb^0 and I^0 , resulting in devices with improved operational stability [32] (Figure 19f).

5.1.2 Passivators

Due to their high reactivity, perovskite surfaces are prone to accommodate various types of defects. The pristine surface was reported to show high recombination rate, which is critical to device efficiency. Moreover, it is susceptible to water and oxygen erosion, which further triggers ion migration and phase segregation. Passivation layer that heals the surface defects, inhibits ion migration and protects perovskite against humidity and oxygen, is crucial for stabilizing PSCs. These passivation layers include ionic crystal salts with or without halide, and neutral molecules, which are intensively investigated in the following categories.

(1) Halide salts

Halide salts are widely used as surface passivator for efficient and stable PSCs. Quaternary ammonium halides were first used in organic-inorganic hybrid perovskites (OIHP) and improved the efficiency and stability of PSCs successfully [260]. The choices of halides and cations significantly influence their impact on device performance. Longer length of alkyl chain could increase the humidity resistance and thermal stability significantly [261]. Higher electrostatic

potentials (φ_{max}) at the $-\text{NH}_3^+$ side bring better surface adsorption of ammonium cations (Figure 20a), to achieve PSCs with high efficiency and stability [162].

The use of halide salts is generally considered to form 2D perovskite on the surface. A 2D perovskite layer could form with both $n=1$ and $n=2$ at room temperature and showed better energy level alignment than that with bare $n=1$ (Figure 7b), which enabled the remained 95% of the initial PCE after 1,200 h damp heat test [81]. The halide choice was also found to strongly affect the dimensionality of 2D perovskite as chloride forms 2D perovskite with both $n=1$ and $n=2$ but bromide or iodide only forms $n=1$ 2D perovskite [262]. In addition, 2D perovskites include not only Ruddlesden-Popper structures (RP) formed with monovalent cations, but also Dion-Jacobson (DJ) structures. Metastable DJ 2D perovskite surface layer with an asymmetric bulky organic molecule could enable sufficient hole transport and improve PCE as well as stability of the PSCs [263]. Some inorganic halides can also form two-dimensional structures. The use of cesium chloride (CsCl) is able to form 2D $\text{Cs}_2\text{PbI}_2\text{Cl}_2$ on the surface of inorganic perovskite CsPbI_3 . Based on degradation acceleration analysis, the $\text{Cs}_2\text{PbI}_2\text{Cl}_2$ capping device was predicted to be stable for over 5 years operating continuously at 35 °C (Figure 20b) [264]. In addition, without forming 2D structure, MgF_x also showed beneficial influence due to its hydrophobic nature and low metal ion diffusivity, resulting in the PSCs with retaining 95% of its PCE after 1,000 h damp heat test [144].

(2) Non-halide salts

Stronger bonding between passivation layer and the perovskite surface is essential to prevent film degradation. Yang et al. [54] reported PSCs with 96.8% PCE remaining after 1,200 h operation by using a chemically stable inorganic lead oxysalt (Figure 20c). PbS was also realized by a surface sulfidation treatment (SST) to construct stable heterojunctions, which effectively inhibits ion migration and improved device stability [82]. Tosylate (TsO^-) was found to induce a striking negative surface charge displacement, leading to positive work function change, bringing higher activation energy on ion migration, which retained 88.5% of its initial PCE after operating for 2,092 h [53].

(3) Neutral molecules

Other types of electron transport and the bonding interaction also played an important role in improving device stability. A sandwiched electrode buffer (SEB) was introduced by employing 2,3,5,6-tetrafluoro-7,7,8,8-tetracyanoquinodimethane (F4-TCNQ) at the two interfaces, perovskite and HTL, as well as HTL and electrode [265]. The SEB successfully improves carrier extraction, and restricts the escape of organic cations and halogen anions, thus improving device stability. Strong Pb-Cl and Pb-O bonds using a chlorinated graphene oxide (Cl-GO) layer achieved PSCs at larger scale, which were stable at continued oper-

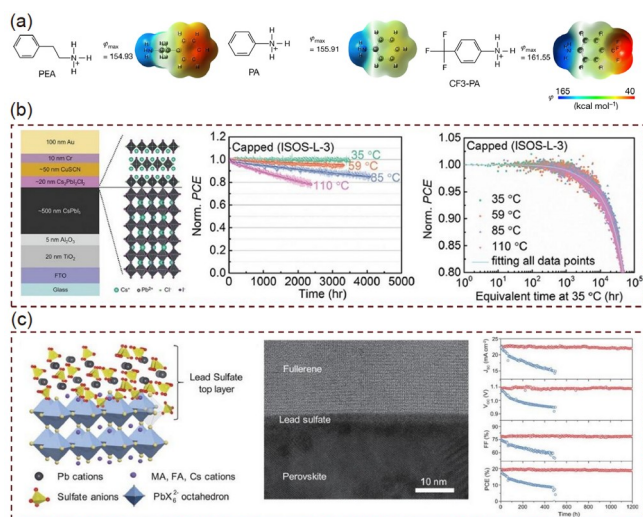


Figure 20 (a) Electrostatic potentials of different ammonium [162]. (b) Structure of Cs₂PbI₂Cl₂ capping layer and resulting device stability [264]. (c) Schematic illustration and distribution of inorganic lead oxysalt layer and resulting device stability [54] (color online).

ating for 1,000 h (90% of initial PCE was remained) [58].

5.1.3 Carrier transport materials

ETLs, as the electron extraction and the hole blocking materials, are important in high-performing PSCs. Early, people used TiO₂ in PSCs, which is a typical photocatalytic material [266]. Due to the photo-instability of TiO₂, another inorganic ETL SnO₂ is gradually adopted for highly efficient and stable PSCs [40,267]. Yoo *et al.* [214] developed an ETL of SnO₂ with ideal film coverage, thickness, and composition by chemical bath deposition (CBD-SnO₂, Figure 21a). Furthermore, Min *et al.* [44] reported the formation of an interlayer at ETL/perovskite interface by coupling Cl-bonded SnO₂ with a Cl-containing perovskite precursor, which successfully reduced interfacial defects. The devices maintained about 90% of their initial efficiency after continuous light exposure for 500 h without encapsulation. In inverted PSCs, inorganic ETLs have also been used to replace organic ETLs due to their inherent high stability [81,177]. Azmi *et al.* [81] deposited a ~10 nm layer of SnO₂ by atomic layer deposition to replace the BCP layer, and the inverted cells retained >95% of their initial PCE after >1,000 h at damp-heat test conditions (encapsulated cells exposed to 85 °C and 85% relative humidity in the dark). The stability of PSCs can be greatly improved by preparing uniform and dense ETL films with intrinsic high stability.

HTLs are responsible for efficient hole extraction at the perovskite/HTL interface. The devices employing spiro-OMeTAD are the most popular, which show the highest PCE currently. However, spiro-OMeTAD has been demonstrated to be unstable due to its low glass transition temperature and hygroscopic dopants inside [268]. To improve the stability of HTLs, Jeon *et al.* [269] introduced a fluorene unit as a new

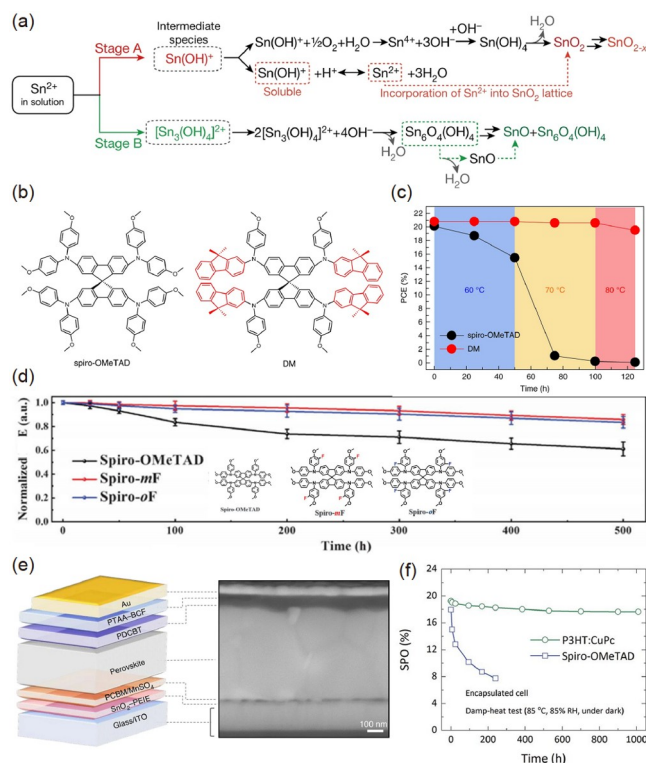


Figure 21 (a) Schematic illustration of the overall reaction mechanism for the formation of the SnO₂-based films [214]. (b) Chemical structures of spiro-OMeTAD and DM [269]. (c) Stability of the devices stressed at different temperatures of 60, 70 and 80 °C in air (~25% RH) with DM and spiro-OMeTAD [269]. (d) Long-term stability of spiro-OMeTAD, Spiro-mF, and Spiro-oF-based devices in air (~50% RH) without encapsulation [270]. (e) Schematic of the double HTL based PSCs and the corresponding cross-sectional backscattered electron imaging of the device [251]. (f) The stability of encapsulated cells based on P3HT:CuPc and spiro-OMeTAD HTL during damp heat tests [39] (color online).

peripheral group instead of *p*-anisole for spiro-OMeTAD, which tuned energy level and glass transition temperature to ensure highly efficient and thermally stable PSCs (Figure 21b, c). Jeong *et al.* [270] synthesized fluorinated isomeric analogs of spiro-OMeTAD, which improved the long-term stability in wet conditions due to the hydrophobicity through the C–F bond (Figure 21d).

In addition, polymer based HTLs have also made great progress in recent years, such as poly(triarylamine) (PTAA) and poly(3-hexylthiophene) (P3HT). Ultrathin and pinhole-free undoped PTAA film could be used to fabricate efficient and stable inverted PSCs [54,62]. However, the PTAA layer requires a larger thickness to fully cover the rough perovskite crystal film in regular PSCs. Therefore, in order to increase hole mobility, p-type doping of PTAA is required. Zhao *et al.* [251] developed a double HTL structure by superimposing Lewis acid tris(pentafluorophenyl)borane doped PTAA on undoped polymer poly[5,5'-bis(2-butyloctyl)-(2,2'-bithiophene)-4,4'-dicarboxylate-alt-5,5'-2,2'-bithiophene] (PDCBT, Figure 21e). PDCBT provided a barrier between the perovskite and Lewis acid doped polymer and improved

the device performance stability. The unencapsulated devices maintained 99% of the initial efficiency after continuous operation at 65 °C for 1,450 h (Figure 19g). Peng *et al.* [39] blended P3HT with another thermally stable HTL, copper phthalocyanine (CuPc), to prepare highly crystalline films with excellent hole transport properties. The P3HT:CuPc-based cell retained ~91.7% of its initial efficiency after 1,009 h at damp-heat test conditions (Figure 21f).

Inorganic HTMs such as nickel derivatives, copper derivatives, can also play a role in hole transport in PSCs. Azmi *et al.* [81] fabricated damp heat-stable PSCs using KCl-passivated NiO_x as HTL, and the inverted cells retained >95% of their initial efficiency after >1,000 h at damp-heat test conditions.

At present, polymer HTLs exhibit good intrinsic stability and hole transport properties, which can potentially enable long lifetime for high-performing PSCs. Further development may focus on the synthesis of new efficient and stable polymer HTLs or efficient and stable p-type doping for polymer HTLs. Moreover, the materials cost will be another potential issue when aiming at commercialization.

5.1.4 Electrodes

Electrodes are deposited on the carrier transport layers, as the current collectors of PSCs. They can be metals, TCO or carbon-based materials. Although common electrodes, such as Au, Ag, Cu and Al are feasible to produce high-efficiency devices, they are unstable due to the diffusion and reaction during device operation [241,271,272]. Even Au will corrode in the presence of reactive polyiodide melts [273]. Besides, the presence of metal in perovskites often leads to deep defect energy levels [274].

To address the stability issue of electrodes, one straightforward method is to directly replace unstable electrodes with stable ones. For example, Mo has been reported to have a diffusion barrier of 0.85–0.95 eV, much larger than that of Au (0.42 eV) or Ag (0.27 eV) [275]. Besides, the reaction between Mo and perovskite is thermodynamically unfavorable [276]. However, the stability improvement sacrificed device PCE (11.38%) due to the shallow work function (−4.6 eV) and/or the damage to the underlying layers during the sputtering process (Figure 22a) [277,278]. Alternatively, metal electrodes can also be replaced by carbon or TCO top electrodes to achieve decent device efficiency. However, both carbon (6–180 Ω sq^{−1}) and TCO (9.9–56 Ω sq^{−1}) have electric resistivity two orders of magnitude higher than metals [278–280]. In this aspect, single Ti adatoms anchored on reduced graphene oxide were reported. It resulted in the device with an efficiency of 20.6%, which retained 98% of the initial values after aging for 1,300 h under illumination [281]. Recently, bifacial devices with ITO top electrode achieved an efficiency of 16.1% and exhibited no degradation after being stored for over 2,000 h (Figure 22b) [282].

The other common method to protect the electrode is to introduce a robust barrier layer including some tough metals (Bi, Ti, Cr), metal oxides [276,283–285], carbon materials [286], TCO (not an independent electrode but a buffer layer) [287]. It is essential to control the thickness of the barrier layers, which guarantees a small series resistance within the contact. Moreover, self-assembled monolayers or *in-situ* deposited 2D materials were found to realize compact thin layer's coating. For example, electrodes of copper-nickel alloy stabilized by *in situ* grown bifacial graphene were reported (Figure 22d) [288]. The resulting devices achieved a power conversion efficiency of 24.34% and retained 97% of the initial efficiency after 1,440 h at 85 °C with 85% relative humidity. Actually, the suppression of the electrode diffusion does not necessarily need a compact barrier layer. Additives in the adjacent layers can also retard the inward electrode diffusion through strong chemical coordination (Figure 22c) [289].

The erosion of electrode materials under environmental factors can be substantially mitigated by encapsulation, which effectively blocks oxygen and water. For the B2C market, the designed life span of PSCs is 3 to 5 years. The commonly used metal electrodes have already met the stability requirements, as reported in the laboratory [62,290]. Anyway, the choice of electrode materials together with the design of matched device structures should never be neglected since it not only impacts the processing complexity and costs but also influences the devices performance (Table 1).

5.2 Ion migration

Ion migration is one significant challenge for the long-life-time devices (Figure 23a, b) [291]. Detailed understanding regarding ion migration has been summarized in some previous reviews [292–296]. This part mainly focuses on the influence of ion migration on device stability which is an intrinsic issue that cannot be simply addressed by device encapsulation.

5.2.1 Irreversible performance decay

Halide perovskites are soft ionic crystals, and the interaction between organic cations and inorganic frames are dominated by ionic and hydrogen bonds. Taking the MAPbI₃ as example, the binding energy between MA⁺ cations and inorganic frames is only ~260 meV [239]. The critical electrical-field for ions to migrate in MAPbI₃ is only ~0.3 V/μm, compared with the built-in electrical field which is in the order of 3.0 V/μm in a practical solar cell [297]. So, the ion migration effect is inevitable throughout the whole working lifetime of solar cells.

Huang *et al.* [298] reported that the decomposition of MAPbI₃ into PbI₂ is reversible once the MA⁺ and I[−] can be injected back to the PbI₂ phase (Figure 23c):

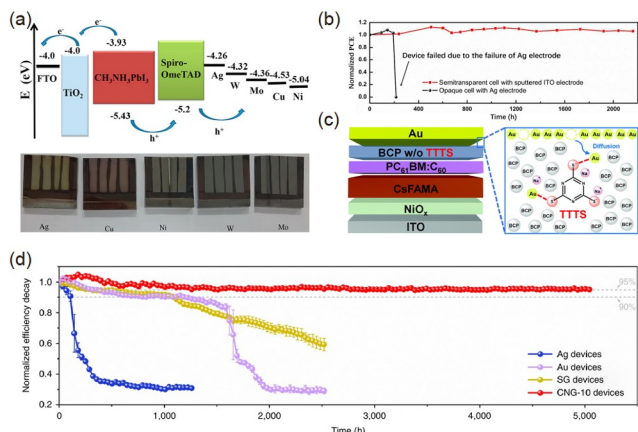
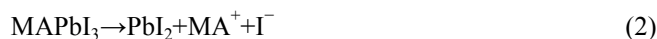


Figure 22 (a) Energy band diagram of PSCs with various electrodes and the corresponding photographs of devices after being exposed in the air for 2 h. The Ag and Cu electrodes of the solar cells are exposed in the air for several hours, and the edge of the metal blurred, while this phenomenon is not observed in devices with the Ni, W, and Mo electrodes. (b) The stability evaluation of semitransparent and opaque PSCs stored in a N_2 -filled glovebox [282]. (c) Device structure and schematic of the BCP layer with 1,3,5-triazine-2,4,6-trithiol trisodium salt [289]. (d) The operational stability of the encapsulated Ag, Au, Cu-Ni alloy with bifacial sprayed graphene as the electrode and graphene/Cu-Ni/graphene composite as the rear electrode devices at the MPP under 1-sun illumination [288] (color online).



The thermodynamic equilibrium between reaction (2) and (3) suggests that the ion migration effect is a double-edged sword. It promotes perovskite decomposition and also enables perovskite self-healing [34,299,300].

The permanent loss of mobile ions in the perovskite crystal can be caused by chemical reaction and outward escaping processes. For instance, I^- can suffer from redox reaction to form radical I^\bullet atoms and/or volatile I_2 according to the following electrochemical reactions [301]:



These excessive I_2 molecules can either evaporate [298] or bound with the negatively charged I^- to form I_3^- . It is detrimental to hybrid perovskite because it dehydrogenates MA^+ cations [302] to generate MA, I_2 , and HI. Meanwhile the migrating MA^+ ions can incorporate into the lattice to

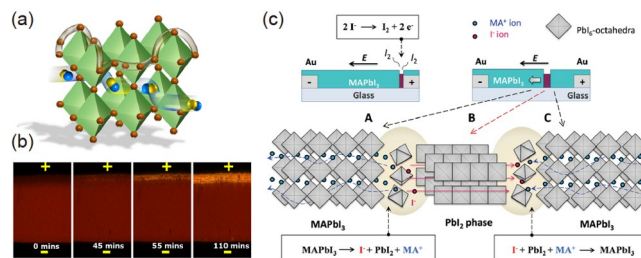


Figure 23 (a) Illustration of the A-site and X-site ions migrating in perovskite crystal [292]. (b) Photos of the ion migration induced decomposition of perovskite material during electrical poling [291]. (c) Reversible conversion between MAPbI_3 and PbI_2 phases due to mobile ions coming out of perovskite (reaction 1) or ions injected into PbI_2 (reaction 2). The formation of I_2 by the redox reaction of I^- (reaction 3) are also illustrated [298] (color online).

form solid solution. Once the accumulated MA^+ ions become over 30%, they will form volatile MA molecules.

The migration of mobile ions within the perovskite to the organic transport layer is another important source of ion loss. The mobile species (e.g., MA^+ , FA^+ , I^- , MA, FA, I_2) move to the organic transport layer (spiro-OMeTAD, PCBM) and even to the metal electrodes (Au, Ag, Cu). It can cause irreversible decomposition in the perovskite layer, which is also detrimental to electrodes and transporting layers. Using internal ionic blocking layers to suppress ions escaping is critical to improving the stability of PSCs. Successful blocking layers include: metal oxide (e.g., Cr_2O_3 [303], Al_2O_3 [304], SnO_2 [182]), 2D inorganic materials (e.g., graphene [286], graphitic carbon nitride [7]), 2D perovskites [6,305], compact lead salts (e.g., PbSO_4 [54], hexamethyldisilathiane-sulfurized pyridine-2-carboxylic lead [82]), inert metal (e.g., bismuth [276]), cross-linkable materials (e.g., silane derivatives [306], benzotriazole [233]) and ion-binding organic molecules (e.g., rubrene [307], boron chloride subphthalocyanine [308], ferrocenyl-bis-thiophene-2-carboxylate [62]).

5.2.2 Interplay between ion migration and other decay mechanisms

Various aging factors (illumination, electrical field, thermal stress, moisture, oxygen, etc.) play their roles simultaneously

Table 1 Stability results of perovskite solar cells with representative structures based on different electrodes

Device structure	PCE (%)	Testing Results	Reference
ITO/PTAA/perovskite/ C_{60} /BCP/Ag	25.0	T_{95} of >1,000 h under the damp heat test (85 °C and 85% RH)	[62]
ITO/ NiO_x /perovskite/ C_{60} / SnO_2 /IZO/Ag	20.3	T_{91} of 1,008 h under the damp heat test (85 °C and 85% RH)	[81]
FTO/ SnO_2 /perovskite/PTAA/Au	21.3	T_{93} of >1,050 h under the damp heat test (85 °C and 85% RH)	[51]
ITO/PTAA/perovskite/ PbSO_4 / C_{60} /BCP/Cu	19.44	T_{96} of > 1,200 h MPP tracking under 65 °C and ~60% RH	[54]
FTO/c- TiO_2 /mp- TiO_2 /perovskite/spiro-OMeTAD/Ti-rGO	20.6	T_{95} of 1,300 h MPP tracking at 60 °C in N_2	[281]
ITO/ SnO_2 /perovskite/spiro-OMeTAD/ITO	16.	No obvious decay stored in a N_2 under ambient light for over 2,000 h	[282]
FTO/ NiMgLiO /perovskite/PCBM/BCP/Bi/Ag	18.72	T_{96} of > 500 h MPP tracking at 45 °C in N_2	[276]
FTO/ SnO_2 /perovskite/PTAA/EVA/ graphene/Cu-Ni/ graphene	23.3	T_{97} of 1,440 h under the damp heat test (85 °C and 85% RH)	[288]

during device operation to impact the efficiency loss. It is important to understand how different decay mechanisms cooperate with each other and open up additional decay pathways. A key route to clarify this question is to track the formation, migration, and detrimental roles of point defects under different aging factors [309].

Incident light impact a lot on ion migration in the following aspects: (1) the rebuilding of the local electrical field causes a redistribution of mobile ions [310–312]; (2) the lattice is “softened” due to the reduced hydrogen bonding between organic cations and inorganic frame (*e.g.*, by 70 meV in MAPbI₃); (3) the photocarriers weaken the Coulomb attraction between mobile ions and lattices by screening effect [313], featured as reduced activation energy for ions to move under light [314,315]; (4) the photogenerated holes oxidize I[−] ions and promote I[•] or I₂ diffusion [316], which offers an explanation to the widely observed photo-induced phase separation in mixed halide perovskites [317].

Electric bias leads to the formation of thermally activated traps by triggering ion migration [318]. Consequently, perovskite materials show fatigue properties under alternate working conditions leading to the degradation of PSCs. Due to these concerns, in a consensus statement formed in 2020, additional bias stability (ISOS-V) and light cycling (ISOS-LC) were recommended to evaluate the intrinsic stability of PSCs [319].

It is known that most of the mobile ions (*e.g.*, MA_i, V_{MA}⁺, V_i, I_i[−]) in perovskites are shallow traps that do not affect the PCE of fresh devices [320]. Huang group [321] found that adding 0.25 mol% excessive CsI does not change the PCE, but the stability of device under illumination has been improved by 3–10 times due to a reduced initial V_i concentration. In the presence of O₂ impurities, V_i as the site of store O₂ molecule and trap electron, which significantly promotes the formation of detrimental O₂ under illumination [322], resulting in H₂O and volatile MA molecules. These results suggest that those mobile, inconspicuous shallow defects would play important roles during the long-term operation of PSCs.

Yet, insights to the cooperation among different degradation processes are insufficient. The accumulated I[−] or MA⁺ (or their vacancies) dissolved in the local perovskite lattice are impurities. It changes the Goldschmidt tolerance factor (*t*) of local crystal, the doping level of local perovskites [297,323], the electrochemical reaction activity of perovskites [322,324], and potentially weakens the hydrogen bonds between A-site cations and inorganic frameworks [325]. Tong *et al.* [326] proposed that the transient lattice distortion caused by I[−] ions movement can induce deep traps and increase local nonradiative recombination rate by one order of magnitude. Zhao *et al.* [327] reported that the energy barrier for ion migration to migrate in MAPbI₃ decreases (*e.g.*, from 0.39 to 0.29 eV) with tensile strain due to the lattice expansion, and increases (*e.g.*, from 0.39 to 0.53 eV) with

compressive strain.

Up to now, the advances to solve the problem of ion migration in PSCs are remarkable [292,293,295,296]. However, eliminating the mobile ions inside perovskites is still challenging. Insights and strategies to incorporate ion migration and other decay mechanisms are important to improve long-term working stability of solar cells.

5.3 Encapsulation

To improve the long-term stability of PSCs and extend their lifetime, encapsulations are generally recognized as an indispensable technique [328]. The encapsulations for PSCs can be roughly divided into internal and external encapsulation depending on the device configuration [329].

Conventional encapsulations for photovoltaics mainly focus on external encapsulation that obstructs the ingress of moisture and oxygen. However, due to their ionic nature, perovskites suffer from intrinsic instability such as chemical reactivity with adjacent layers, photodegradation, and ion migration. Therefore, internal encapsulations are developed for PSCs to extend their service time and boost their performance simultaneously.

UV curable adhesives were the firstly employed as the PSCs encapsulant, due to their merits of solvent-free processing and high transparency. For example, coating photocurable resins onto the PSCs could achieve relatively stable outdoor operation [330]. However, their inherent disadvantages [331–333] surged the emergence of novel encapsulation technologies. For instance, Lee *et al.* [334] deposited multilayers of functional barriers onto the PSCs as thin-film encapsulation and their corresponding device retains 97% of the initial PCE after being exposed to the condition of 50°C, 50%RH for 300 h.

Vacuum lamination encapsulation has also been considered as a promising technology (Figure 24a). It was revealed that the compatibility between lamination fillers and PSCs greatly affects the final effectiveness [335,336], which is as important as the waterproofing of encapsulation itself. In that case, polyisobutene (PIB) edge encapsulation appears to be the most effective for PSCs under harsh test conditions [337] and exceeds the requirement of the IEC61215:2016 standard for the first time [338]. Recently, Azmi *et al.* [81] integrated PIB edge seal vacuum lamination technology and 2D/3D heterojunction as an encapsulation system, resulting in 95% PCE retention (initial at 24.3%) after 1,000 h damp-heat test condition.

The internal encapsulation aims at improving the intrinsic stability of the perovskite active layer and relevant contacts, which is unique and inevitable for PSCs.

Grain boundaries are typical modification sites for internal encapsulations. Liu *et al.* [339] applied *in-situ* formed

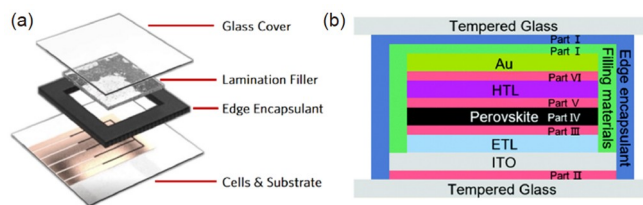


Figure 24 (a) Typical vacuum lamination encapsulation structure. (b) General schematic diagram of the PSCs encapsulation (color online).

amorphous silica to the grain boundaries of perovskites to delay the phase transformation from photoactive phase to non-photoactive phase, which results in 97% retention of its initial PCE after 1,000 h ambient atmosphere storage. In addition, it improves the charge-carriers dynamics of the perovskite active layers as well. Another common strategy is to construct a heterojunction at the grain boundaries of perovskites to reduce the defect density and suppress the ion migration [305].

Interface encapsulation is a frequently applied strategy too. McKenna *et al.* [340] investigated several common polymer encapsulants and their potential as functional interface barriers of MA-based PSCs and concluded that the improvements caused by coated polymers are highly related to their physical properties. Figure 24b displays the basic scheme of PSCs and all its potentially modifiable interfaces. Parts I and IV: physically isolate cells from the outside, part II: diminish the effects of UV light, and parts III and V: improve the structural stability of perovskite. Thereby the device could be systematically stabilized by the synergistic effect of interface encapsulations.

Electrode encapsulation has also attracted much attention recently due to its non-negligible erosion during device aging. Zai *et al.* [265] fabricated a sandwiched electrode buffer, which enhances the PCE to 23.4% (certificated), and only 3% PCE was lost during the 2,000 h maximum power point tracking.

Besides, it should be noted that the encapsulation of PSCs has extra value beyond protecting the device [341], *e.g.*, preventing lead leakage by slowing down the dissolution rate of perovskite composition [342] or deploying self-healing-based encapsulation [343].

In short, the quest for compiling with current PSCs leads to a complex variety of materials, processing, schemes and their combination when developing suitable encapsulation. What is more, the multifarious characterization also increases the difficulty in comparing and evaluating the validity of encapsulation strategies. The working mechanisms should be revealed in line with technical advances. Hence, we genuinely advocate establishing a unified encapsulation test standard for PSCs devices to obtain comparable data that can be circulated over the community for meaningful interpretation and analysis.

6 Application

PSCs have the advantages of low temperature processing, low cost, light weight, adjustable band gap from 1.2 to 2.6 eV and high resistance to the radiation in outer space. These advantages make PSCs have broad industrialization prospects in the indoor application, flexible electronics, and outer space application, which will be summarized in this chapter.

6.1 Indoor applications

Indoor photovoltaics (IPVs) have attracted major interest and developed rapidly in the context of the quick development of modernization due to a gap in the need for billions of self-powered electronic gadgets [344]. OSCs, DSSCs, GaAs, and a-Si-based IPVs have all seen significant development in recent years [345–348]. However, the drawbacks of these indoor photovoltaic systems include their high cost, incompatibility with outdoor light, difficulties in manufacturing flexible devices, and relatively low efficiency. The possibility of commercializing perovskite indoor photovoltaics (PIPVs) is increased by its benefits meeting the internet of things (IoT) requirements, which include low cost, fabrication of flexible PSCs, and easily adjustable band gaps [349–352].

6.1.1 Superiorities of PIPVs

To achieve a low level of the energy cost compared to conventional fossil fuel energy, PIPVs should combine the advantages of low cost, great performance, and long-term stability. Based on preliminary life cycle assessment results, PSC modules are projected to have a lower environmental impact and the merit of shorter energy payback time (EPBT) [353]. Future decreases in the production cost of PSCs are projected as a result of the rise in continuous operation length, which can drastically lower the maintenance and replacement costs of photovoltaic modules. Additionally, several research teams have examined the production costs of PSC modules and derived precise estimates of the levelized cost of power (LCOE). The PSCs' manufacturing costs, according to the calculations by Egan *et al.* [230], range from \$ 87 to 140 m⁻², with LCOE values of 9 to 19 cents per kWh.

The tunable band gap of perovskite materials makes them particularly desirable for use in IPV applications. Different indoor light sources have different indoor spectra as shown in Figure 25a [354], so choosing a perovskite with a matching band gap can maximize the indoor efficiency of the PSCs theoretically. Methylammonium lead iodide (MAPbI₃) served as the foundation for the first PSCs with the band gap of 1.55 eV, which evolved to replace various sites and extended to other perovskite compositions [1]. The band gap of perovskites can be changed from infrared (1.15 eV) to ul-

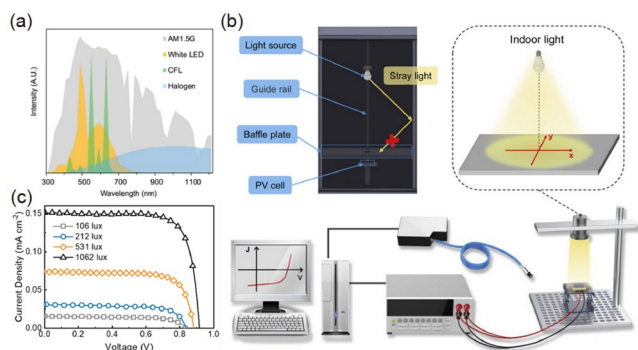


Figure 25 (a) Emission spectra of different light sources, where CFL is compact fluorescent. (b) A typical setup for PCE measurement and schematic illustrations of each component. (c) J - V curves measured under different illumination (color online).

traviolet (3 eV) through compositional engineering of mixed various cations or anions. Undoubtedly, as solar technology develops, more and more perovskite materials can be used in place of cations and anions to produce high-performance PIPVs. In addition, PIPVs need to be made using large-area flexible manufacturing processes since IoT devices are durable, wearable, and portable. Compared to other production methods, the continuous R2R process makes perovskite thin films much more quickly and efficiently. The low PCE of this approach, however, restricts further progress. Flexible large-area PIPV cells for the creation of cutting-edge methods improve the device's operation, which include engineering of the component, the interface, and the solvent atmosphere.

6.1.2 Precise measurement of IPVs

It is critical to accurately evaluate the photovoltaic performance of IPVs. In our daily lives, we use a variety of indoor lighting alternatives, including indirect sunlight, incandescent, halogen, fluorescent, light-emitting diode (LED), and other low-intensity (200–1,000 lux) light sources. To calibrate indoor light sources, Wong *et al.* [355] advised using a general-purpose LED light meter with National Institute of Standards and Technology (NIST)-traceable calibration. They also advised using the maximum power point P_{\max} and PCE values to precisely assess device performance. Hou *et al.* [356] recommended that the following components should be included in a precise IPV test as shown in Figure 25b in order to calibrate indoor light sources. (1) The stability of the indoor photovoltaic measurement light source should be less than 2%. The test must be conducted in a well-lit area with a spatial distribution of light intensity of less than 2%. (2) To test PCE, use a mask with the same or smaller size than the transparent substrate of the cells. (3) Spectrometers work better for calibrating interior light sources than illuminometers. (4) Comparing the integrated- J_{SC} and actual J_{SC} differences by no more than 5%

can be used to validate the test's correctness.

6.1.3 Developments and opportunities of PIPVs

The performance of perovskite photovoltaics in low light was originally reported by Chen *et al.* [357] in 2015 by optimizing the manufacturing process for the electron transport layer. Then, PCBM was modified using 1-butyl-3-methylimidazolium tetrafluoroborate ionic liquid in an inverted PSC in 2018 by Li *et al.* [358]. Under a fluorescent lamp with 1,000 lux, the generated PSCs displayed a record indoor PCE of 35.20%. The ground-breaking effectiveness directed subsequent PIPV research and development. Three years later, in 2021, He *et al.* [359] used micron-thick perovskite films to reach a record low-light PIPVs efficiency of over 40%.

High-performance PIPVs can be created using the all-inorganic perovskite material CsPbBr₂ (1.89 eV), given the accordance between its bandgap and the spectrum of indoor light sources (200–700 nm). Wang *et al.* [360] looked into the morphology, composition and defects of CsPbBr₂ films using the smelting multiple recrystallization approaches. The crystal structure was improved, producing perovskite films of excellent quality and with much lower trap densities of states. A greater indoor PCE of 33.50% (LED 2,956 K, P_{in} : 334.41 W/cm²) was obtained in the final optimized photovoltaic device. Compared with rigid devices, flexible PSCs can provide a more suitable surface for indoor small electronics, making them promising for indoor applications. Chen *et al.* [361] firstly studied indoor flexible PSC photovoltaics. To achieve full-dimensional stress release, they chose a 3D cross-linking chemical called borax to penetrate perovskite films' grain boundaries. The device exhibits an outstanding indoor PCE of 31.85% at 1,062 lux because of the low trap density of states under indoor illumination as shown in Figure 25c. The toxicity of photovoltaic devices is also a crucial factor for ultimate market selection because indoor photovoltaics are more likely to come into contact with humans. For the first time, lead-free tin-based perovskites were used in PIPVs by Yang *et al.* [362]. This work greatly boosted the prospect of lead-free PSCs for IPV applications.

6.2 Flexible applications

Flexible PSCs have great attractions for their much desired advantages in portability, compatibility, R2R continuous production for potentially much lower cost and the high power-to-weight ratio [46,363–366]. In just a few years, the highest efficiency of flexible PSCs has exceeded 22.44% [367] due to the good quality of the perovskite thin films achieved by various low-temperature fabrication methods and the great achievements in developing the suitable interface and electrodes materials. The big difference between

rigid and flexible PSCs originates from the conductive substrate. Therefore, this section mainly focuses on the recent impressive advances in flexible electrodes including (1) the demonstrated TCO electrodes in flexible PSCs, according to the following factors, such as high transmittance, good conductivity, suitable energy level and easy operation at low-temperature; (2) developed flexible opaque electrode materials to enhance the mechanical stability of flexible devices.

6.2.1 Flexible transparent conductive electrodes

There are two types of electrodes in flexible PSCs. One is a TCO, and the other is a flexible opaque electrode. Flexible TCOs not only have high optical transparency and good electrical conductivity for ensuring enough light absorption and smooth charge transport, but also need to be durable to keep the photoelectric properties during bending for their mechanical stability. The commonly used TCOs in PSCs are the metal oxide materials including ITO, FTO, aluminum doped zinc oxide (AZO) [368,369], and IZO [332,368]. The deposition temperature of FTO is more than 350 °C, which is too high to be coated on flexible polymer substrates such as polyethylene terephthalate (PET) and polyethylene naphthalate [370]. ITO, AZO and IZO are suitable as the flexible TCOs in flexible PSCs because they could be fabricated at low temperature. However, AZO easily reacts with perovskite absorber, leading to the reduced efficiency of flexible PSCs [368]. IZO shows a higher fill factor (FF) in flexible PSCs due to the lower resistance [371], and flexible devices based on ITO have better J_{SC} because of the higher optical transmittance [368]. Up to now, the most commonly used TCOs in flexible PSCs are ITO coated on polymer substrates owing to their excellent optoelectronic properties. The high efficiency over 20% and record efficiency of 22.44% for flexible PSCs are also based on ITO coated on polymer substrates [367,372–374]. However, ITO is brittle, resulting in cracks during bending at a small radius (<4 mm) [333,375,376], as shown in Figure 26a, b.

To overcome the fracture of brittle ITO film, other types of flexible TCOs have been developed, including high conductive polymer (PEDOT:PSS), graphene, metal nanowires (NW) and ultrathin metal film. In general, the pristine PEDOT:PSS has low electrical conductivity, and it often needs to be modified to improve its conductivity. Bauer *et al.* [283] used DMSO and Zonyl FS-300 doped PEDOT:PSS as an electrode on 1.4 μm thick PET substrates to fabricate flexible PSCs, and the stabilized efficiency was up to 12% with the remarkable endurance even under repeated compression. Song *et al.* [377] employed glycol and Zonyl FS-300 modified PEDOT:PSS to improve the conductivity of about 40 Ω/sq , yielding an efficiency of 12.32% for large-scale flexible PSCs with excellent flexural endurance, retaining about 90% of the initial efficiency after 1,000 cycles using a 2-mm-curvature radius. Choi *et al.* [378] adopted

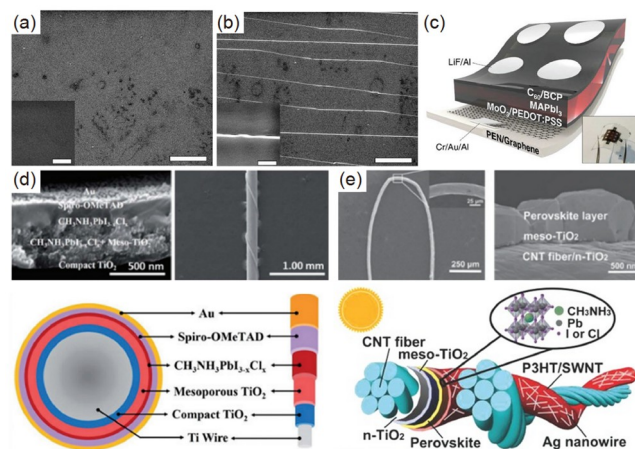


Figure 26 SEM images of PET/ITO substrate before (a) and after (b) bending for 2,200 times, and the scale bars are 50 μm (main) and 5 μm (inset), respectively [376]. (c) Structure of a flexible PSCs based on graphene electrode; an inset is the photograph of the device [378]. (d) Structure of flexible PSCs based on Ti wire [387]. (e) Structure of flexible PSCs using CNT fibers [388] (color online).

wet-transfer 2D graphene as a transparent electrode to fabricate flexible PSCs, and the structure is shown in Figure 26c. This transparent electrode showed a higher sheet resistance of 552 Ω/sq than that of ITO (13.3 Ω/sq), but its better-aligned energy level and higher transmittance led to the comparable efficiency of 16.8% with the device based on the ITO electrode (17.3%). The flexible device kept 85% of the original efficiency after 5,000 bending cycles at a radius of 2 mm. Hou *et al.* [379] sandwiched the Ag NWs between the monolayer graphene and the polymer matrix to attack degradation. The hybrid electrodes significantly decreased resistance to 8.06 Ω/sq , and the efficiency of MA-based flexible PSCs was 10.4%. Ultrathin metal films have been developed as flexible transparent electrodes due to the easy preparation process and their excellent electrical and mechanical properties. Priya *et al.* [380] fabricated electrode Cr (1 nm)/Au (7 nm)/MgF₂ (90 nm) with a transparency of 78.6% in 350 nm–1,200 nm and resistance of 16.3 Ω/sq . Bolink *et al.* [381] made electrodes by AZO (30 nm)/Ag (9 nm)/AZO (30 nm) with optical transparency of 81% in the visible region and resistance of 7.5 Ω/sq . Sun *et al.* [382] used MoO₃ (3 nm)/Au (7 nm) film with a resistance of 19 Ω/sq and light transmittance of about 70% to fabricate flexible PSCs, and the efficiency was 9.05% with good mechanical flexibility.

Compared to metal oxide flexible transparent electrodes, although above mentioned flexible electrodes show good mechanical stability, the efficiency is far away from the highest value of flexible PSCs based on ITO. The relatively large sheet resistance of PEDOT:PSS and graphene limits the performance of PSCs. Ag NWs are the potential candidate as a flexible transparent electrode due to the low cost and low-temperature solution-processed, but the chemical

interaction with perovskite materials, high resistance due to the node of Ag NWs, and the rough surface decreases the efficiency of flexible PSCs. The low transparency of ultrathin metal-based flexible bottom electrodes also limits the performance of flexible PSCs. Therefore, the record efficiency of flexible PSCs based on a transparent electrode is still dominated by ITO due to its high transmittance, good conductivity, matched energy level and chemical stability against perovskite materials.

6.2.2 Flexible opaque electrodes

The above section focuses on the flexible transparent electrode which are the conventional bottom electrodes in flexible PSCs. The flexible opaque electrodes are the unconventional but promising strategy in flexible PSCs. Metal foil and fabric electrodes can be employed as flexible opaque electrodes thanks to their excellent mechanical endurance.

Metal foils such as titanium foil (Ti-foil) and copper foil (Cu-foil) are the normally used flexible substrates. The most frequently used TiO_2 electron transport layer is very convenient to be obtained on Ti-foil. Lee *et al.* [383] reported a record efficiency of 14.9% based on the flexible device structure of Ti-foil/ TiO_2 /MAPbI₃/ultrathin Cu/Au. Compared to conventional polymer/ITO substrate, Ti-foil shows higher fatigue resistance, and outstanding mechanical stability. The flexible device based on TiO_2 -foil maintains 100% initial efficiency after bending 1,000 times at the bending radius of 4 mm. Cu-foil-based flexible PSCs also displayed good feasibility. Moshaii *et al.* [384] fabricated cuprous iodide as the hole transport layer by exposing the Cu-foil in iodide vapor, followed by deposition of perovskite, ZnO electron transport layer, and Ag NWs transparent top electrode, and the device shows the efficiency of 12.8%. The fiber-based flexible electrode has been applied to photoelectric field such as supercapacitors, sensors, batteries and solar cells, due to the potential of integration into wearable textiles [385]. Peng *et al.* [386] first used a stainless-steel fiber as the cathode to fabricate the fiber-based flexible perovskite solar cell. They adopted dip-coated method to deposit electron transport layer, perovskite, and hole transport layer, and then utilized the carbon nanotube (CNT) array as the transparent electrode. The efficiency was up to 3.3%, demonstrating the successful attempt for fiber-based flexible perovskite devices. Zou *et al.* [387] employed the Ti fiber as the flexible electrode to fabricate the perovskite device, as shown in Figure 26d. TiO_2 , perovskite, and spiro-OMeTAD were integrated into Ti fiber, and ultrathin Au nanoparticles were used as the transparent electrode. The device shows an efficiency of 5.3% under 1-sun illumination and 8.3%-efficiency in a diffuse model. Li *et al.* [388] used the flexible multi-twisted CNT as the electrode, and Ag NWs as the transparent electrode to fabricate the perovskite de-

vice, as shown in Figure 26e. The flexible device gives an efficiency of 3.03% without significant efficiency loss after 1,000 bending cycles.

Although both foil-based and fiber-based flexible PSCs show excellent mechanical stability, the challenges in these types of flexible PSCs are the cost and the top transparent electrode manufacturing, which inspires us to seek other types of flexible substrates and electrodes as the candidates.

6.3 Space applications

The outstanding PCE [74,389], high specific power (*i.e.*, power to weight ratio) [390], superior compatibility with flexible substrates [391], and excellent radiation resistance [392] of PSCs render them potential candidates for next-generation space photovoltaics. In this part, we will review the recent progress in the research of PSCs for space application. Firstly, the extreme environment in space and specific requirements for PSCs are discussed. Secondly, the radiation resistance of PSCs is reviewed. Thirdly, space flight experiments of PSCs are given.

6.3.1 Extreme environment in space and specific requirements for space photovoltaics

Compared with the terrestrial environment of human life, the space environment is very harsh. As shown in Figure 27a, the space environment features ultra-high vacuum and alternating temperature, and also contains strong radiation including gamma-rays, ultraviolet rays, X-rays, *beta*-rays, protons, neutrons, and electrons [393,394], particularly in the Van Allen radiation belt. Due to the existence of more ultraviolet rays in space, the AM0 solar spectrum exhibits higher total radiation of 136.7 mW cm^{-2} . These characteristics of the space environment directly affect the in-orbit service performance and stability of the materials and devices working in space. Specifically, the high-energy particle radiation could induce lattice defects in the semiconductors and ultimately cause a decrease in the performance of PSCs. Considering the high cost of space launching ranging between $\sim \$ 30,000$ and $\sim \$ 1,500 \text{ kg}^{-1}$, depending on the characteristics of the vehicles [395], space photovoltaics should meet specific requirements such as high PCEs, specific power and long-term stability.

6.3.2 Radiation resistance of PSCs

For space application, PSCs must have good radiation resistance to ensure long-term stability. As mentioned above, the space environment is characterized by high-energy charged particles and rays. In this part, we mainly introduce the proton radiation resistance and gamma-ray resistance of PSCs.

Protons are one of the most common high-energy particles in space, which have greater mass than electrons ($\sim 2,000$

times). Hence the proton radiation in the MeV range poses a greater threat to the materials and devices, and has shown a tremendous effect on the output performance of Si, GaAs, and InP solar cells. In 2016, the inverted-structure PSCs with the device architecture of ITO/PEDOT:PSS/MAPbI₃/PCBM/BCP/Ag were bombarded with protons with the energy of 68 MeV by Neitzert *et al.* [392] to investigate the proton radiation hardness, as shown in Figure 27b. PSCs were compared with the commercial Si solar cells in terms of V_{OC} , FF , J_{SC} and PCE (Figure 27c). When the dose of $\leq 2 \times 10^{11}$ p cm⁻² was applied, PSCs exhibited negligible degradation. However, a 30% decrease in the J_{SC} of Si solar cells was observed exposed to the same dose. Upon the proton radiation with the dose of more than 2×10^{11} p cm⁻², the J_{SC} and PCE of PSCs decreased, while the V_{OC} and FF remained constant. A decrease of around 10% and 40% in J_{SC} as well as PCE of PSCs was observed at higher proton dose levels of 10^{12} and 10^{13} p cm⁻², respectively. For Si solar cells, a 40% decrease in J_{SC} was observed at a proton dose of only $\phi = 7 \times 10^{11}$ p cm⁻². It is noteworthy that it normally takes about 3 years or less to accumulate a dose of 10^{12} p cm⁻² on a satellite-relevant orbit [396]. These results obtained by Neitzert *et al.* [392] confirm that PSCs have a great tolerance for proton bombardment, showing great potential as space photovoltaics.

Gamma-ray is a kind of common high-energy ray in space, which has the shortest wavelength and the highest frequency in the electromagnetic spectrum. Metal halide perovskites have been used in gamma-ray detection by directly converting ray radiation into electrical signals [397]. In 2019, the inverted-structure PSCs with the device architecture of ITO/PTAA/Cs_{0.05}FA_{0.81}MA_{0.14}PbI_{2.55}Br_{0.45}/C₆₀/BCP/Cu was placed under the radiation of both light illumination and gamma-ray to investigate the radiation resistance by Huang *et al.* [398] (Figure 27d, e). The J - V curves of PSCs before the radiation test show that PSCs exhibit an initial PCE of 18.8% with a V_{OC} of 1.06 V, a J_{SC} of 21.98 mA cm⁻², and an FF of 80.5%. After radiation, the J_{SC} decreased a lot. According to their report, the decrease in J_{SC} was mainly due to the obvious loss in the transmittance of the glass substrates under the gamma-ray radiation. The darkening of the glass substrates is mainly attributed to the production of impurity levels and new absorption bands in the glass upon the gamma-ray radiation [399]. What is more, they found that there was a self-healing behavior of PSCs to recover its efficiency at the early stage of degradation induced by gamma-ray radiation. The experimental results indicate the superior stability of perovskites to gamma-ray radiation compared with glass.

6.3.3 Space flight experiments of PSCs

To promote the space application of PSCs, a lot of studies have been done in the laboratory-simulated environment, and

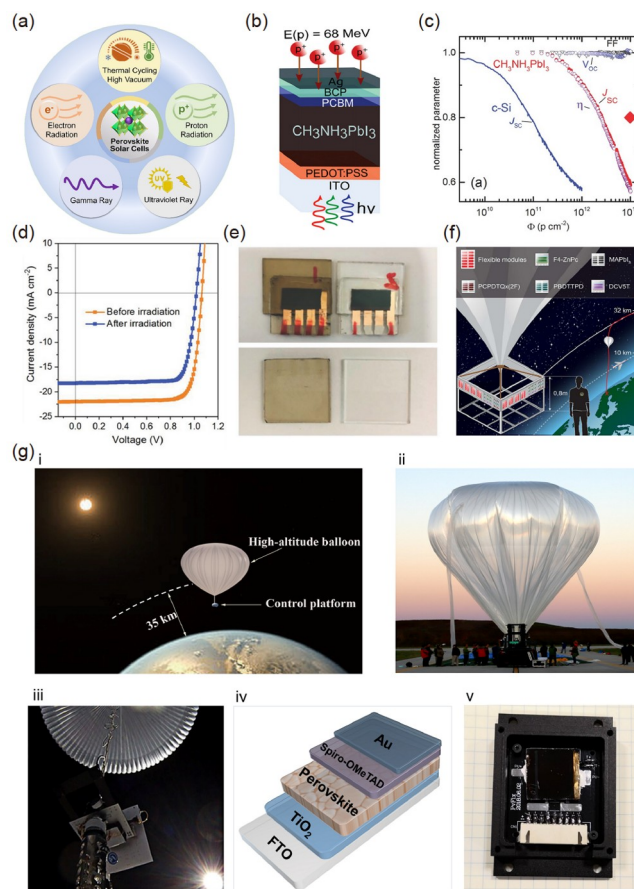


Figure 27 (a) Factors affecting the performance of PSCs in space [399]. (b) A sketch of the inverted-structure PSC (Proton radiation of 68 MeV) [392]. (c) Normalized photovoltaic parameters of a PSC as a function of the proton dose (ϕ). Symbols depict the evolution of J_{SC} , FF , η (PCE), and V_{OC} of a PSC. The red diamond depicts the normalized value of J_{SC} at the end of the proton irradiation experiment after correcting transmission losses due to color centres in the substrate. The blue curve shows the evolution of the J_{SC} of a c-Si photodiode [392]. (d) J - V curves of the PSC before and after irradiation test [398]. (e) Pictures of PSCs (top panel) and ITO substrates (bottom panel) before (right panel) and after (left panel) gamma-ray radiation. The radiation dose was 2.3 Mrad with a duration of 1,535 h [398]. (f) Mounting structure of solar cells, and the schematics of the flight altitude. The experiment counted 4 panels holding solar panels [400]. (g) i) Representative schematic showing the relative positions of the sun, the high-altitude balloon, and the earth; ii) photograph of the launch site; iii) photograph of the high-altitude balloon with a pod in near space; iv) device configuration of a PSC; v) unit module (the large-area PSC was soldered on the integrated circuit board) [401] (color online).

the real environment test is definitely indispensable. The space flight experiments of PSCs have been carried out through the high-altitude science balloon by Manca *et al.* [400] and Zhu *et al.* [401], respectively.

The first flight experiment reached an altitude of 32 km through the high-altitude balloon [400], as shown in Figure 27f. The power output at the maximum power point of PSCs with time was tracked to evaluate the performance change of devices. Another pioneering space flight experiment was carried out by Zhu and his collaborators [401]. They sent the

large-area regular mesoporous TiO_2 -based PSCs into near space at an altitude of 35 km through a high-altitude balloon (Figure 27g). The device based on $\text{FA}_{0.81}\text{MA}_{0.10}\text{Cs}_{0.04}\text{PbI}_{0.55}\text{Br}_{0.40}$ retained 95.19% of its initial PCE during the test under AM0 illumination after two hours. Following these two pioneering studies, more space flight experiments have been carried out. For example, an experiment with PSCs on board of a rocket flight was carried out by Müller-Buschbaum *et al.* [402] in 2020 and the rocket reached the apogee with an altitude of 239 km. In 2021, researchers at National Renewable Energy Laboratory, cooperating with teams from the National Aeronautics and Space Administration (NASA), sent eight PSCs to the International Space Station to evaluate the potential use of PSCs in space and assessed the durability of materials used in those cells [403]. Before that, NASA has verified that a MAPbI_3 film with encapsulation can work on the International Space Station in the space environment for a total of approximately 10 months on orbit with little to no chemical degradation [404].

PSCs currently show great potential for space application. However, it is still a long way from practical application. Scientists need to further carry out considerable research from the perspective of both mechanism exploration and stability in the real space environment to obtain highly robust PSCs.

7 Industrialization

Until now, the efficiency of small area PSCs is comparable to the Si solar cells, minimodule efficiency also exceeded 20.0%, and the stability is greatly improved. Moreover, the PSCs have a high potential to achieve lower manufacturing cost than Si solar cells because of low-temperature solution coating. Consequently, many companies in the world started to industrialize PSCs, and focused on developing large area modules and efficient manufacturing processes. Accompanied with mission-driven policies by governments, more and more investment has been attracted to enter this field. Several companies have now announced to build a 100 MW production line and first commercial scale module samples were delivered.

7.1 In Japan

The Japanese government has always paid attention to the development of PSCs since the PSCs were invented by Japanese researchers [1]. Recently, New Energy and Industrial Technology Development Organization (NEDO) started a national project (Green Innovation Project), and invested 20 billion Japanese Yen to develop PSCs [405]. Several famous companies such as Toshiba Corporation, Sekisui Chemical Co., Ltd., Aisin Corporation, Kaneka Corporation, were

joined in this project, in collaboration with the National Institute of Advanced Industrial Science and Technology, the University of Tokyo, and Kyoto University. They are committed to the obligation of commercializing PSCs by 2030 [405]. Up to now, Toshiba Corporation developed rigid and flexible PSCs submodules, with the PCE of 11.6% (802 cm^2) and 15.1% (703 cm^2) respectively [406,407]. Sekisui Chemical Co. reported flexible perovskite solar modules with PCE of 15% by the R2R process [408], which aims to be commercialized by 2025. In addition, Panasonic achieved a submodule PCE of 17.9% with designated illumination area of 804 cm^2 [2].

7.2 In China

The Chinese government also attaches great importance to the development of PSCs. In 2022, the National Energy Administration and the Ministry of Science and Technology issued a notice on the issuance of the “14th Five-Year Plan for Scientific and Technological Innovation in the Energy Sector”. The specific goals of wind and solar power technologies are focusing on the establishment of large-scale and high-proportion renewable energy supply, including encouraging the industrial production of highly efficient PSCs. Currently, several national projects are carrying on development of PSCs with various missions such as perovskite/Si tandem solar cells, submodule with 20% PCE on area over 400 cm^2 , illumination durability of 10,000 h. A flexible PSC project will start this year. On the other hand, several famous silicon solar companies such as LONGI, JinKO, Trina Solar have already started to research perovskite/Si TSCs. Beside, PSC start-ups are also developing fast. The GCL Photoelectric Materials Co., Ltd. achieved an active efficiency of 15.31% for perovskite module with area of $1,241.16\text{ cm}^2$, and is building a 100 MW production line with module size of $1\text{ m}\times 2\text{ m}$ [409]. MicroQuanta Semiconductor achieved a world record efficiency of 21.4% for 19.3 cm^2 minimodule [2]. Moreover, it has built a 100 MW production line and has delivered the first batch of 5,000 pieces modules ($1.245\text{ m}\times 0.635\text{ m}$) to their customers [410]. UtmoLight also achieved a 20.5% efficiency for 63.98 cm^2 mini-modules in 2021 [411] and invested over 3 billion RMB to the production line. Wonder Solar also installed a 110 m^2 pilot power plant with printable mesoscopic perovskite solar panels in 2018 [412]. After the carbon-neutral policy was announced by the governments, there are about 20 start-ups in the perovskite field.

7.3 In Europe

In Europe, Oxford PV was founded by one of the pioneers of PSCs, Henry Snaith, which focuses on the development of perovskite/Si tandem solar cells. It achieved a perovskite/Si

tandem solar cell with an efficiency of 29.52% [413], and built a 100 MW production line for the tandem solar cell in Germany last year [414]. Saule Technologies focuses on building integrated Photovoltaics (BIPV) and they launched a production line in Wroclaw, Poland in 2021 [415]. Solliance (Netherlands) achieved a stabilized efficiency of 17.8% for wide-bandgap (1.69 eV) PSCs in 2021. In combination with the Panasonic silicon bottom cell, they achieved an efficiency of 29.2% for 4 T perovskite/Si [416]. Moreover, they also achieved a 18.6% efficient highly NIR transparent PSCs and combined in 4T tandem configuration with an efficient Panasonic c-Si cell with a PCE of 28.7% [417]. Specific (U.K.) developed its pilot manufacturing lines to deliver building-scale products [418]. TubeSolar (Germany) achieved an efficiency of 14% for film-based PSCs by R2R process in 2022 [419], collaborating with the Centre for Solar Energy and Hydrogen Research Baden-Württemberg (ZSW). Evolar (Sweden) is preparing its manufacturing line, reporting the results of device durability tests [420].

7.4 Other countries

The United States Department of Energy (DOE) has selected 19 projects for a total of \$ 6 million to fund innovative solar cells, and these projects were selected through the Solar Energy Technology Office's (SETO) Small Innovative Projects in Solar (SIPS) 2022 funding program, three of which are based on PSCs [421]. Besides, there are also more and more companies working on the industrialization of PSCs, such as Swift Solar, Tandem PV, Cubic PV, and EMC (USA). The "GigaSpeed" production line of EMC has capacity to manufacture PV material equivalent to 4 GW per year, based on a R2R printing process [422]. Besides the United States, UniTest in Korea achieved a sub-module efficiency of 14.8% [423], and invested in large-scale facilities for PSCs in the Saemangeum Industrial Complex. Hanwha Q CELLS in Korea is heavily investing in R&D, including perovskite/Si tandem cells, seeking to invest 1.5 trillion KRW (\$ 1.2 billion) into research and manufacturing facilities by 2025 [424].

8 Perspectives

In summary, the PSCs are becoming more and more mature by device engineering of single and tandem configurations, upscaling-to-module technologies, and stabilization projects to meet real operating conditions. Now, PSCs are on the eve of industrialization. To accelerate the industrialization process, the following suggestions are proposed.

The structure of PSCs is mainly divided into normal and inverted structures. The normal ones attract much more attention since they show a higher PCE record of over 25%.

However, they also face stability issues, such as the instability of spiro-OMeTAD at high temperature and ambient environments. It is urgent to enhance the stability of normal PSCs. For the inverted PSCs, although the PCE is still lower than that of the normal ones, they show better operation stability and compatibility with tandem solar cells. It is important to further improve the PCE of inverted PSCs by optimizing perovskite and the interface layer.

For perovskite-based tandem solar cells, the 1-cm² perovskite/c-Si cells stand out with a promising PCE of over 30%, being closest to commercialization. The future target is to realize a PCE > 30% based on the commercialized-size silicon solar cells with stability of over 20 years. Hence, improvement of the light management and optimization of the interfacial layer in perovskite/c-Si cells should be also carried out by a combination of simulation and experiment. Moreover, developing new low-cost technologies to deposit PSCs on Si solar cells is in demand.

The efficiency of small-area single-junction PSCs (<0.1 cm²) is now comparable to those of the Si solar cells. However, enlarging the device area to modules will lead to a significant efficiency decrease. The efficiency of PSC modules with an area over 1,000 cm² still remains around 15%, as shown in Figure 28a. According to the previous analysis, to achieve a similar LCOE with Si solar cells of 3 US cents/kWh, the PCE of PSC modules should reach over 20% in the case of 20-years lifetime (Figure 28b) [425]. To reach this goal, continuous innovation should be devoted to the exploration of the new fabrication process of high-quality large-scale perovskite layers and other functional layers, so as to control the crystallinity and uniformity of all layers of modules in environmental conditions in industry. The development of new module structures to improve the stability of PSCs without compromising efficiency is also an important issue [7].

It is undeniable that stability is an immense obstacle for PSCs for commercialization. Although several groups reported that the PSCs have passed several requirements of the IEC61215:2016 standard, there is still a long way to go. Recently, a stand-alone solar farm infrastructure has been demonstrated for the outdoor field tests of PSCs, but the power output of the panel efficiency lost by 25% over 9

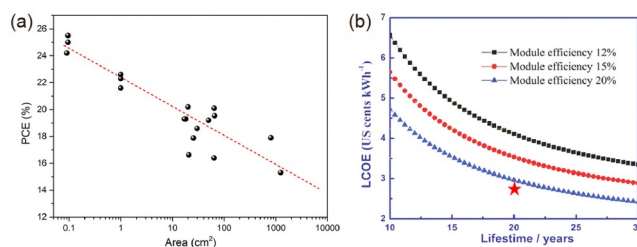


Figure 28 (a) The dependence of PCE on device areas. (b) The relationship between LCOE and lifetime [425] (color online).

months [426]. It is imperative to quantitatively understand the outdoor degradation modes, and accordingly, to improve materials and device configurations. Besides, establishment of new testing standards suitable for analyzing the decomposition mechanism of PSCs are also needed.

Finally, although a huge number of papers were published, the efficiencies of the modules improved slowly. Fortunately, more and more companies are entering industrialize the PSCs, which will help academic researchers to clarify their research targets. Therefore, to accelerate the commercialization, we suggest the industry should disclose the urgent problems they faced. For example, industry should converse with academia on which cell structure (normal structure or inverted structure) is more desirable for industrialization, and then academia can concentrate on one device structure to accelerate research progress. We believe that strengthening the relationship between academia and industry and timely feedback on technical routes from industry to academia will accelerate the speed of improvement of PSCs such as outdoor stability, and large-scale manufacturing. Hence, the perovskite photovoltaic will be brought to fruition in the near future.

Conflict of interest The authors declare no conflict of interest.

- Kojima A, Teshima K, Shirai Y, Miyasaka T. *J Am Chem Soc*, 2009, 131: 6050–6051
- Green MA, Dunlop ED, Hohl-Ebinger J, Yoshita M, Kopidakis N, Bothe K, Hinken D, Rauer M, Hao X. *Prog Photovoltaics*, 2022, 30: 687–701
- <https://www.nrel.gov/pv/cell-efficiency.html>
- Jeng JY, Chiang YF, Lee MH, Peng SR, Guo TF, Chen P, Wen TC. *Adv Mater*, 2013, 25: 3727–3732
- Ding Y, Ding B, Kanda H, Usiobo OJ, Gallet T, Yang Z, Liu Y, Huang H, Sheng J, Liu C, Yang Y, Queloz VIE, Zhang X, Audinot JN, Redinger A, Dang W, Mosconic E, Luo W, De Angelis F, Wang M, Dörflinger P, Armer M, Schmid V, Wang R, Brooks KG, Wu J, Dyakonov V, Yang G, Dai S, Dyson PJ, Nazeeruddin MK. *Nat Nanotechnol*, 2022, 17: 598–605
- Mei A, Sheng Y, Ming Y, Hu Y, Rong Y, Zhang W, Luo S, Na G, Tian C, Hou X, Xiong Y, Zhang Z, Liu S, Uchida S, Kim TW, Yuan Y, Zhang L, Zhou Y, Han H. *Joule*, 2020, 4: 2646–2660
- Bi E, Tang W, Chen H, Wang Y, Barbaud J, Wu T, Kong W, Tu P, Zhu H, Zeng X, He J, Kan S, Yang X, Grätzel M, Han L. *Joule*, 2019, 3: 2748–2760
- Chen Z, Dong Q, Liu Y, Bao C, Fang Y, Lin Y, Tang S, Wang Q, Xiao X, Bai Y, Deng Y, Huang J. *Nat Commun*, 2017, 8: 1890
- Han Y, Xie H, Lim EL, Bi D. *Sol RRL*, 2022, 6: 2101007
- Gao F, Zhao Y, Zhang X, You J. *Adv Energy Mater*, 2020, 10: 1902650
- Kim M, Kim GH, Lee TK, Choi IW, Choi HW, Jo Y, Yoon YJ, Kim JW, Lee J, Huh D, Lee H, Kwak SK, Kim JY, Kim DS. *Joule*, 2019, 3: 2179–2192
- Gao F, Luo C, Wang X, Zhao Q. *Small Methods*, 2021, 5: 2100856
- Li Q, Zhao Y, Fu R, Zhou W, Zhao Y, Liu X, Yu D, Zhao Q. *Adv Mater*, 2018, 30: 1803095
- Zhao Y, Tan H, Yuan H, Yang Z, Fan JZ, Kim J, Voznyy O, Gong X, Quan LN, Tan CS, Hofkens J, Yu D, Zhao Q, Sargent EH. *Nat Commun*, 2018, 9: 1607
- Li Q, Zhao Y, Zhou W, Han Z, Fu R, Lin F, Yu D, Zhao Q. *Adv Energy Mater*, 2019, 9: 1902239
- Wang S, Jin J, Qi Y, Liu P, Xia Y, Jiang Y, He R, Chen B, Liu Y, Zhao X. *Adv Funct Mater*, 2020, 30: 1908343
- Xie L, Lin K, Lu J, Feng W, Song P, Yan C, Liu K, Shen L, Tian C, Wei Z. *J Am Chem Soc*, 2019, 141: 20537–20546
- Alharbi EA, Baumeler TP, Krishna A, Alyamani AY, Eickemeyer FT, Ouellette O, Pan L, Alghamdi FS, Wang Z, Alotaibi MH, Yang B, Almalki M, Mensi MD, Albrithen H, Albadri A, Hagfeldt A, Zakeeruddin SM, Grätzel M. *Adv Energy Mater*, 2021, 11: 2003785
- Zhou W, Chen S, Zhao Y, Li Q, Zhao Y, Fu R, Yu D, Gao P, Zhao Q. *Adv Funct Mater*, 2019, 29: 1809180
- Shen Z, Han Q, Luo X, Shen Y, Wang T, Zhang C, Wang Y, Chen H, Yang X, Zhang Y, Han L. *Energy Environ Sci*, 2022, 15: 1078–1085
- Zhou T, Xu Z, Wang R, Dong X, Fu Q, Liu Y. *Adv Mater*, 2022, 34: 2200705
- Luo C, Zheng G, Gao F, Wang X, Zhao Y, Gao X, Zhao Q. *Joule*, 2022, 6: 240–257
- Hui W, Chao L, Lu H, Xia F, Wei Q, Su Z, Niu T, Tao L, Du B, Li D, Wang Y, Dong H, Zuo S, Li B, Shi W, Ran X, Li P, Zhang H, Wu Z, Ran C, Song L, Xing G, Gao X, Zhang J, Xia Y, Chen Y, Huang W. *Science*, 2021, 371: 1359–1364
- Xiang W, Zhang J, Liu SF, Albrecht S, Hagfeldt A, Wang Z. *Joule*, 2022, 6: 315–339
- Wei Q, Ye Z, Ren X, Fu F, Yang Z, Liu S, Yang D. *Sci China Chem*, 2020, 63: 818–826
- Chao L, Niu T, Xia Y, Chen Y, Huang W. *Acc Mater Res*, 2021, 2: 1059–1070
- Li N, Niu X, Li L, Wang H, Huang Z, Zhang Y, Chen Y, Zhang X, Zhu C, Zai H, Bai Y, Ma S, Liu H, Liu X, Guo Z, Liu G, Fan R, Chen H, Wang J, Lun Y, Wang X, Hong J, Xie H, Jakob DS, Xu XG, Chen Q, Zhou H. *Science*, 2021, 373: 561–567
- Wang X, Han Z, Gao F, Luo C, Zhao Q. *Sol RRL*, 2022, 6: 2100973
- Lu H, Liu Y, Ahlawat P, Mishra A, Tress WR, Eickemeyer FT, Yang Y, Fu F, Wang Z, Avalos CE, Carlsen BI, Agarwalla A, Zhang X, Li X, Zhan Y, Zakeeruddin SM, Emsley L, Rothlisberger U, Zheng L, Hagfeldt A, Grätzel M. *Science*, 2020, 370: eabb8985
- Bu T, Li J, Li H, Tian C, Su J, Tong G, Ono LK, Wang C, Lin Z, Chai N, Zhang XL, Chang J, Lu J, Zhong J, Huang W, Qi Y, Cheng YB, Huang F. *Science*, 2021, 372: 1327–1332
- Zhang F, Zhu K. *Adv Energy Mater*, 2020, 10: 1902579
- Wang L, Zhou H, Hu J, Huang B, Sun M, Dong B, Zheng G, Huang Y, Chen Y, Li L, Xu Z, Li N, Liu Z, Chen Q, Sun LD, Yan CH. *Science*, 2019, 363: 265–270
- Zhuang X, Zhou D, Liu S, Sun R, Shi Z, Liu L, Wang T, Liu B, Liu D, Song H. *Adv Energy Mater*, 2022, 12: 2200614
- Zhao Y, Wei J, Li H, Yan Y, Zhou W, Yu D, Zhao Q. *Nat Commun*, 2016, 7: 10228
- Li Y, Chen Z, Yu B, Tan S, Cui Y, Wu H, Luo Y, Shi J, Li D, Meng Q. *Joule*, 2022, 6: 676–689
- Pazos-Outón LM, Xiao TP, Yablonovitch E. *J Phys Chem Lett*, 2018, 9: 1703–1711
- Kim HS, Lee CR, Im JH, Lee KB, Moehl T, Marchioro A, Moon SJ, Humphry-Baker R, Yum JH, Moser JE, Grätzel M, Park NG. *Sci Rep*, 2012, 2: 591
- Tan H, Jain A, Voznyy O, Lan X, García de Arquer FP, Fan JZ, Quintero-Bermudez R, Yuan M, Zhang B, Zhao Y, Fan F, Li P, Quan LN, Zhao Y, Lu ZH, Yang Z, Hoogland S, Sargent EH. *Science*, 2017, 355: 722–726
- Peng J, Walter D, Ren Y, Tebyetekerwa M, Wu Y, Duong T, Lin Q, Li J, Lu T, Mahmud MA, Lem OLC, Zhao S, Liu W, Liu Y, Shen H, Li L, Kremer F, Nguyen HT, Choi DY, Weber KJ, Catchpole KR, White TP. *Science*, 2021, 371: 390–395
- Jiang Q, Zhang L, Wang H, Yang X, Meng J, Liu H, Yin Z, Wu J, Zhang X, You J. *Nat Energy*, 2017, 2: 1–7
- Jia J, Qian C, Dong Y, Li YF, Wang H, Ghoussoub M, Butler KT, Walsh A, Ozin GA. *Chem Soc Rev*, 2017, 46: 4631–4644
- Jung EH, Chen B, Bertens K, Vafaie M, Teale S, Proppe A, Hou Y,

- Zhu T, Zheng C, Sargent EH. *ACS Energy Lett*, 2020, 5: 2796–2801
- 43 Mosconi E, Ronca E, De Angelis F. *J Phys Chem Lett*, 2014, 5: 2619–2625
 - 44 Min H, Lee DY, Kim J, Kim G, Lee KS, Kim J, Paik MJ, Kim YK, Kim KS, Kim MG, Shin TJ, Seok S II. *Nature*, 2021, 598: 444–450
 - 45 Xiong Z, Chen X, Zhang B, Odunmbaku GO, Ou Z, Guo B, Yang K, Kan Z, Lu S, Chen S, Ouedraogo NAN, Cho Y, Yang C, Chen J, Sun K. *Adv Mater*, 2022, 34: 2106118
 - 46 Yang D, Yang R, Wang K, Wu C, Zhu X, Feng J, Ren X, Fang G, Priya S, Liu SF. *Nat Commun*, 2018, 9: 3239
 - 47 Qin Z, Chen Y, Wang X, Wei N, Liu X, Chen H, Miao Y, Zhao Y. *Adv Mater*, 2022, 34: 2203143
 - 48 Luo X, Shen Z, Shen Y, Su Z, Gao X, Wang Y, Han Q, Han L. *Adv Mater*, 2022, 34: 2202100
 - 49 Chen P, Bai Y, Wang S, Lyu M, Yun J, Wang L. *Adv Funct Mater*, 2018, 28: 1706923
 - 50 Cho Y, Soufiani AM, Yun JS, Kim J, Lee DS, Seidel J, Deng X, Green MA, Huang S, Ho-Baillie AWY. *Adv Energy Mater*, 2018, 8: 1703392
 - 51 Jang YW, Lee S, Yeom KM, Jeong K, Choi K, Choi M, Noh JH. *Nat Energy*, 2021, 6: 63–71
 - 52 Jiang Q, Zhao Y, Zhang X, Yang X, Chen Y, Chu Z, Ye Q, Li X, Yin Z, You J. *Nat Photon*, 2019, 13: 460–466
 - 53 Tan S, Huang T, Yavuz I, Wang R, Yoon TW, Xu M, Xing Q, Park K, Lee DK, Chen CH, Zheng R, Yoon T, Zhao Y, Wang HC, Meng D, Xue J, Song YJ, Pan X, Park NG, Lee JW, Yang Y. *Nature*, 2022, 605: 268–273
 - 54 Yang S, Chen S, Mosconi E, Fang Y, Xiao X, Wang C, Zhou Y, Yu Z, Zhao J, Gao Y, De Angelis F, Huang J. *Science*, 2019, 365: 473–478
 - 55 Jung EH, Jeon NJ, Park EY, Moon CS, Shin TJ, Yang TY, Noh JH, Seo J. *Nature*, 2019, 567: 511–515
 - 56 Wang R, Xue J, Wang KL, Wang ZK, Luo Y, Fenning D, Xu G, Nuryeva S, Huang T, Zhao Y, Yang JL, Zhu J, Wang M, Tan S, Yavuz I, Houk KN, Yang Y. *Science*, 2019, 366: 1509–1513
 - 57 Su H, Lin X, Wang Y, Liu X, Qin Z, Shi Q, Han Q, Zhang Y, Han L. *Sci China Chem*, 2022, 65: 1321–1329
 - 58 Wang Y, Wu T, Barbaud J, Kong W, Cui D, Chen H, Yang X, Han L. *Science*, 2019, 365: 687–691
 - 59 Lu C, Zhu C, Meng L, Sun C, Lai W, Qin S, Zhang J, Huang W, Du J, Wang Y, Li Y. *Sci China Chem*, 2021, 64: 2035–2044
 - 60 Chen W, Wu Y, Yue Y, Liu J, Zhang W, Yang X, Chen H, Bi E, Ashraful I, Grätzel M, Han L. *Science*, 2015, 350: 944–948
 - 61 Li X, Liu X, Wang X, Zhao L, Jiu T, Fang J. *J Mater Chem A*, 2015, 3: 15024–15029
 - 62 Li Z, Li B, Wu X, Sheppard SA, Zhang S, Gao D, Long NJ, Zhu Z. *Science*, 2022, 376: 416–420
 - 63 Chen S, Xiao X, Gu H, Huang J. *Sci Adv*, 2021, 7: eabe8130
 - 64 Wu Y, Xie F, Chen H, Yang X, Su H, Cai M, Zhou Z, Noda T, Han L. *Adv Mater*, 2017, 29: 1701073
 - 65 Li X, Zhang W, Wang YC, Zhang W, Wang HQ, Fang J. *Nat Commun*, 2018, 9: 3806
 - 66 Li X, Fu S, Liu S, Wu Y, Zhang W, Song W, Fang J. *Nano Energy*, 2019, 64: 103962
 - 67 Zheng X, Hou Y, Bao C, Yin J, Yuan F, Huang Z, Song K, Liu J, Troughton J, Gasparini N, Zhou C, Lin Y, Xue DJ, Chen B, Johnston AK, Wei N, Hedhili MN, Wei M, Alsalloum AY, Maity P, Turedi B, Yang C, Baran D, Anthopoulos TD, Han Y, Lu ZH, Mohammed OF, Gao F, Sargent EH, Bakr OM. *Nat Energy*, 2020, 5: 131–140
 - 68 Gharibzadeh S, Fassel P, Hossain IM, Rohrbeck P, Frericks M, Schmidt M, Duong T, Khan MR, Abzieher T, Nejand BA, Schackmar F, Almora O, Feeney T, Singh R, Fuchs D, Lemmer U, Hofmann JP, Weber SAL, Paetzold UW. *Energy Environ Sci*, 2021, 14: 5875–5893
 - 69 Lin YH, Sakai N, Da P, Wu J, Sansom HC, Ramadan AJ, Mahesh S, Liu J, Oliver RDJ, Lim J, Aspitarte L, Sharma K, Madhu PK, Morales-Vilches AB, Nayak PK, Bai S, Gao F, Grovenor CRM, Johnston MB, Labram JG, Durrant JR, Ball JM, Wenger B, Stanowski B, Snaith HJ. *Science*, 2020, 369: 96–102
 - 70 Bai S, Da P, Li C, Wang Z, Yuan Z, Fu F, Kawecki M, Liu X, Sakai N, Wang JTW, Huettner S, Buecheler S, Fahlman M, Gao F, Snaith HJ. *Nature*, 2019, 571: 245–250
 - 71 Ni Z, Bao C, Liu Y, Jiang Q, Wu WQ, Chen S, Dai X, Chen B, Hartweg B, Yu Z, Holman Z, Huang J. *Science*, 2020, 367: 1352–1358
 - 72 Stolterfoht M, Wolff CM, Márquez JA, Zhang S, Hages CJ, Rothhardt D, Albrecht S, Burn PL, Meredith P, Unold T, Neher D. *Nat Energy*, 2018, 3: 847–854
 - 73 Chen S, Liu Y, Xiao X, Yu Z, Deng Y, Dai X, Ni Z, Huang J. *Joule*, 2020, 4: 2661–2674
 - 74 Luo D, Yang W, Wang Z, Sadhanala A, Hu Q, Su R, Shivanna R, Trindade GF, Watts JF, Xu Z, Liu T, Chen K, Ye F, Wu P, Zhao L, Wu J, Tu Y, Zhang Y, Yang X, Zhang W, Friend RH, Gong Q, Snaith HJ, Zhu R. *Science*, 2018, 360: 1442–1446
 - 75 Zhang M, Chen Q, Xue R, Zhan Y, Wang C, Lai J, Yang J, Lin H, Yao J, Li Y, Chen L, Li Y. *Nat Commun*, 2019, 10: 4593
 - 76 Godding JSW, Ramadan AJ, Lin YH, Schutt K, Snaith HJ, Wenger B. *Joule*, 2019, 3: 2716–2731
 - 77 Li F, Deng X, Qi F, Li Z, Liu D, Shen D, Qin M, Wu S, Lin F, Jang SH, Zhang J, Lu X, Lei D, Lee CS, Zhu Z, Jen AKY. *J Am Chem Soc*, 2020, 142: 20134–20142
 - 78 Zheng X, Troughton J, Gasparini N, Lin Y, Wei M, Hou Y, Liu J, Song K, Chen Z, Yang C, Turedi B, Alsalloum AY, Pan J, Chen J, Zhumekenov AA, Anthopoulos TD, Han Y, Baran D, Mohammed OF, Sargent EH, Bakr OM. *Joule*, 2019, 3: 1963–1976
 - 79 Degani M, An Q, Albaladejo-Siguan M, Hofstetter YJ, Cho C, Paulus F, Grancini G, Vaynzof Y. *Sci Adv*, 2021, 7: eabj7930
 - 80 Chen H, Teale S, Chen B, Hou Y, Grater L, Zhu T, Bertens K, Park SM, Atapattu HR, Gao Y, Wei M, Johnston AK, Zhou Q, Xu K, Yu D, Han C, Cui T, Jung EH, Zhou C, Zhou W, Proppe AH, Hoogland S, Laquai F, Filleter T, Graham KR, Ning Z, Sargent EH. *Nat Photon*, 2022, 16: 352–358
 - 81 Azmi R, Ugur E, Seikhan A, Aljamaan F, Subbiah AS, Liu J, Harrison GT, Nugraha MI, Eswaran MK, Babics M, Chen Y, Xu F, Allen TG, Rehman AU, Wang CL, Anthopoulos TD, Schwingschlögl U, De Bastiani M, Aydin E, De Wolf S. *Science*, 2022, 376: 73–77
 - 82 Li X, Zhang W, Guo X, Lu C, Wei J, Fang J. *Science*, 2022, 375: 434–437
 - 83 Chen S, Xiao X, Chen B, Kelly LL, Zhao J, Lin Y, Toney MF, Huang J. *Sci Adv*, 2021, 7: eabb2412
 - 84 Xiao M, Lu T, Lin T, Andre JS, Chen Z. *Adv Energy Mater*, 2020, 10: 1903053
 - 85 Yang X, Luo D, Xiang Y, Zhao L, Anaya M, Shen Y, Wu J, Yang W, Chiang YH, Tu Y, Su R, Hu Q, Yu H, Shao G, Huang W, Russell TP, Gong Q, Stranks SD, Zhang W, Zhu R. *Adv Mater*, 2021, 33: 2006435
 - 86 Chen S, Dai X, Xu S, Jiao H, Zhao L, Huang J. *Science*, 2021, 373: 902–907
 - 87 Wu S, Zhang J, Li Z, Liu D, Qin M, Cheung SH, Lu X, Lei D, So SK, Zhu Z, Jen AKY. *Joule*, 2020, 4: 1248–1262
 - 88 Boyd CC, Shallcross RC, Moot T, Kerner R, Bertoluzzi L, Onno A, Kavadiya S, Chosy C, Wolf EJ, Werner J, Raiford JA, de Paula C, Palmstrom AF, Yu ZJ, Berry JJ, Bent SF, Holman ZC, Luther JM, Ratcliff EL, Armstrong NR, McGehee MD. *Joule*, 2020, 4: 1759–1775
 - 89 Chen B, Chen H, Hou Y, Xu J, Teale S, Bertens K, Chen H, Proppe A, Zhou Q, Yu D, Xu K, Vafaie M, Liu Y, Dong Y, Jung EH, Zheng C, Zhu T, Ning Z, Sargent EH. *Adv Mater*, 2021, 33: 2103394
 - 90 Zhang W, Li X, Fu S, Zhao X, Feng X, Fang J. *Joule*, 2021, 5: 2904–2914
 - 91 Li E, Liu C, Lin H, Xu X, Liu S, Zhang S, Yu M, Cao X, Wu Y, Zhu W. *Adv Funct Mater*, 2021, 31: 2103847
 - 92 Li E, Bi E, Wu Y, Zhang W, Li L, Chen H, Han L, Tian H, Zhu W.

- Adv Funct Mater*, 2020, 30: 1909509
- 93 Ku Z, Rong Y, Xu M, Liu T, Han H. *Sci Rep*, 2013, 3: 3132
 - 94 Mei A, Li X, Liu L, Ku Z, Liu T, Rong Y, Xu M, Hu M, Chen J, Yang Y, Grätzel M, Han H. *Science*, 2014, 345: 295–298
 - 95 Hu Y, Si S, Mei A, Rong Y, Liu H, Li X, Han H. *Sol RRL*, 2017, 1: 1600019
 - 96 Rong Y, Hu Y, Mei A, Tan H, Saidaminov MI, Seok SI, McGehee MD, Sargent EH, Han H. *Science*, 2018, 361: eaat8235
 - 97 Bogachuk D, Saddedine K, Martineau D, Narbey S, Verma A, Gebhardt P, Herterich JP, Glissmann N, Zouhair S, Markert J, Gould IE, McGehee MD, Würfel U, Hinsch A, Wagner L. *Sol RRL*, 2022, 6: 2100527
 - 98 Liu S, Zhang D, Sheng Y, Zhang W, Qin Z, Qin M, Li S, Wang Y, Gao C, Wang Q, Ming Y, Liu C, Yang K, Huang Q, Qi J, Gao Q, Chen K, Hu Y, Rong Y, Lu X, Mei A, Han H. *Fundamental Res*, 2022, 2: 276–283
 - 99 Hu Y, Zhang Z, Mei A, Jiang Y, Hou X, Wang Q, Du K, Rong Y, Zhou Y, Xu G, Han H. *Adv Mater*, 2018, 30: 1705786
 - 100 Xiao X, Chu Y, Zhang C, Zhang Z, Qiu Z, Qiu C, Wang H, Mei A, Rong Y, Xu G, Hu Y, Han H. *Fundamental Res*, 2021, 1: 385–392
 - 101 Yang J, Li S, Xiao X, Du J, Xia M, Xiao X, Wang W, Hu W, Mei A, Hu Y, Han H. *Chem Eng J*, 2022, 446: 136967
 - 102 Chen X, Xia Y, Huang Q, Li Z, Mei A, Hu Y, Wang T, Checharoen R, Rong Y, Han H. *Adv Energy Mater*, 2021, 11: 2100292
 - 103 Du J, Qiu C, Li S, Zhang W, Zhang W, Wang Y, Qiu Z, Wang Q, Yang K, Mei A, Rong Y, Hu Y, Han H. *Adv Energy Mater*, 2022, 12: 2102229
 - 104 Liu J, Li S, Liu S, Chu Y, Ye T, Qiu C, Qiu Z, Wang X, Wang Y, Su Y, Hu Y, Rong Y, Mei A, Han H. *Angew Chem Int Ed*, 2022, 61: e202202012
 - 105 Tian C, Mei A, Zhang S, Tian H, Liu S, Qin F, Xiong Y, Rong Y, Hu Y, Zhou Y, Xie S, Han H. *Nano Energy*, 2018, 53: 160–167
 - 106 Shi T, Lin S, Fang M, Kong D, Yuan Y, Gao Y, Yang B, Han H, Zhou C. *Appl Phys Lett*, 2020, 117: 163501
 - 107 Zouhair S, Luo B, Bogachuk D, Martineau D, Wagner L, Chahboun A, Glunz SW, Hinsch A. *Sol RRL*, 2022, 6: 2100745
 - 108 Zouhair S, Yoo S, Bogachuk D, Herterich JP, Lim J, Kanda H, Son B, Yun HJ, Würfel U, Chahboun A, Nazeeruddin MK, Hinsch A, Wagner L, Kim H. *Adv Energy Mater*, 2022, 12: 2200837
 - 109 Zhou C, Lin S. *Sol RRL*, 2020, 4: 1900190
 - 110 Rong Y, Hou X, Hu Y, Mei A, Liu L, Wang P, Han H. *Nat Commun*, 2017, 8: 14555
 - 111 Wang Q, Zhang W, Zhang Z, Liu S, Wu J, Guan Y, Mei A, Rong Y, Hu Y, Han H. *Adv Energy Mater*, 2020, 10: 1903092
 - 112 Polman A, Knight M, Garnett EC, Ehrler B, Sinke WC. *Science*, 2016, 352: aad4424
 - 113 Mailoa JP, Bailie CD, Johlin EC, Hoke ET, Akey AJ, Nguyen WH, McGehee MD, Buonassisi T. *Appl Phys Lett*, 2015, 106: 121105
 - 114 Sahli F, Kamino BA, Werner J, Bräuninger M, Paviet-Salomon B, Barraud L, Monnard R, Seif JP, Tomasi A, Jeangros Q, Hessler-Wyser A, De Wolf S, Despeisse M, Nicolay S, Niesen B, Ballif C. *Adv Energy Mater*, 2018, 8: 1701609
 - 115 Qiu Z, Xu Z, Li N, Zhou N, Chen Y, Wan X, Liu J, Li N, Hao X, Bi P, Chen Q, Cao B, Zhou H. *Nano Energy*, 2018, 53: 798–807
 - 116 Zhu S, Hou F, Huang W, Yao X, Shi B, Ren Q, Chen J, Yan L, An S, Zhou Z, Ren H, Wei C, Huang Q, Li Y, Hou G, Chen X, Ding Y, Wang G, Li B, Zhao Y, Zhang X. *Sol RRL*, 2018, 2: 1800176
 - 117 Zheng J, Lau CFJ, Mehrvarz H, Ma FJ, Jiang Y, Deng X, Soeriyadi A, Kim J, Zhang M, Hu L, Cui X, Lee DS, Bing J, Cho Y, Chen C, Green MA, Huang S, Ho-Baillie AWY. *Energy Environ Sci*, 2018, 11: 2432–2443
 - 118 Zheng J, Mehrvarz H, Ma FJ, Lau CFJ, Green MA, Huang S, Ho-Baillie AWY. *ACS Energy Lett*, 2018, 3: 2299–2300
 - 119 Shen H, Omelchenko ST, Jacobs DA, Yalamanchili S, Wan Y, Yan D, Phang P, Duong T, Wu Y, Yin Y, Samundsett C, Peng J, Wu N, White TP, Andersson GG, Lewis NS, Catchpole KR. *Sci Adv*, 2018, 4: eaau9711
 - 120 Hou F, Han C, Isabella O, Yan L, Shi B, Chen J, An S, Zhou Z, Huang W, Ren H, Huang Q, Hou G, Chen X, Li Y, Ding Y, Wang G, Wei C, Zhang D, Zeman M, Zhao Y, Zhang X. *Nano Energy*, 2019, 56: 234–240
 - 121 Hou F, Yan L, Shi B, Chen J, Zhu S, Ren Q, An S, Zhou Z, Ren H, Wei C, Huang Q, Hou G, Chen X, Li Y, Ding Y, Wang G, Zhang D, Zhao Y, Zhang X. *ACS Appl Energy Mater*, 2019, 2: 243–249
 - 122 Bett AJ, Schulze PSC, Winkler KM, Kabakli ÖS, Ketterer I, Mundt LE, Reichmuth SK, Siefert G, Cojocar L, Tutsch L, Bivour M, Hermle M, Glunz SW, Goldschmidt JC. *Prog Photovolt Res Appl*, 2019, 28: 99–110
 - 123 Zheng J, Mehrvarz H, Liao C, Bing J, Cui X, Li Y, Gonçalves VR, Lau CFJ, Lee DS, Li Y, Zhang M, Kim J, Cho Y, Caro LG, Tang S, Chen C, Huang S, Ho-Baillie AWY. *ACS Energy Lett*, 2019, 4: 2623–2631
 - 124 Chen B, Wang P, Li R, Ren N, Chen Y, Han W, Yan L, Huang Q, Zhang D, Zhao Y, Zhang X. *J Energy Chem*, 2021, 63: 461–467
 - 125 Aydin E, Liu J, Ugur E, Azmi R, Harrison GT, Hou Y, Chen B, Zhumagali S, De Bastiani M, Wang M, Raja W, Allen TG, Rehman A, Subbiah AS, Babics M, Babayigit A, Isikgor FH, Wang K, Van Kerschaver E, Tsetseris L, Sargent EH, Laquai F, De Wolf S. *Energy Environ Sci*, 2021, 14: 4377–4390
 - 126 Wang L, Song Q, Pei F, Chen Y, Dou J, Wang H, Shi C, Zhang X, Fan R, Zhou W, Qiu Z, Kang J, Wang X, Lambert A, Sun M, Niu X, Ma Y, Zhu C, Zhou H, Hong J, Bai Y, Duan W, Ding K, Chen Q. *Adv Mater*, 2022, 34: 2201315
 - 127 Jošt M, Köhnen E, Morales-Vilches AB, Lipovšek B, Jäger K, Maccio B, Al-Ashouri A, Krč J, Korte L, Rech B, Schlattmann R, Topić M, Stannowski B, Albrecht S. *Energy Environ Sci*, 2018, 11: 3511–3523
 - 128 Bush KA, Manzoor S, Frohna K, Yu ZJ, Raiford JA, Palmstrom AF, Wang HP, Prasanna R, Bent SF, Holman ZC, McGehee MD. *ACS Energy Lett*, 2018, 3: 2173–2180
 - 129 Kim CU, Yu JC, Jung ED, Choi IY, Park W, Lee H, Kim I, Lee DK, Hong KK, Song MH, Choi KJ. *Nano Energy*, 2019, 60: 213–221
 - 130 Chen B, Yu Z, Liu K, Zheng X, Liu Y, Shi J, Spronk D, Rudd PN, Holman Z, Huang J. *Joule*, 2019, 3: 177–190
 - 131 Köhnen E, Jošt M, Morales-Vilches AB, Tockhorn P, Al-Ashouri A, Maccio B, Kegelmann L, Korte L, Rech B, Schlattmann R, Stannowski B, Albrecht S. *Sustain Energy Fuels*, 2019, 3: 1995–2005
 - 132 Mazzarella L, Lin Y, Kirner S, Morales-Vilches AB, Korte L, Albrecht S, Crossland E, Stannowski B, Case C, Snaith HJ, Schlattmann R. *Adv Energy Mater*, 2019, 9: 1803241
 - 133 Al-Ashouri A, Köhnen E, Li B, Magomedov A, Hempel H, Caprioglio P, Márquez JA, Morales Vilches AB, Kasparavicius E, Smith JA, Phung N, Menzel D, Grischek M, Kegelmann L, Skroblin D, Gollwitzer C, Malinauskas T, Jošt M, Matič G, Rech B, Schlattmann R, Topić M, Korte L, Abate A, Stannowski B, Neher D, Stollerfoht M, Unold T, Getautis V, Albrecht S. *Science*, 2020, 370: 1300–1309
 - 134 Köhnen E, Wagner P, Lang F, Cruz A, Li B, Roß M, Jošt M, Morales-Vilches AB, Topić M, Stollerfoht M, Neher D, Korte L, Rech B, Schlattmann R, Stannowski B, Albrecht S. *Sol RRL*, 2021, 5: 2100244
 - 135 Wu Y, Zheng P, Peng J, Xu M, Chen Y, Surve S, Lu T, Bui AD, Li N, Liang W, Duan L, Li B, Shen H, Duong T, Yang J, Zhang X, Liu Y, Jin H, Chen Q, White T, Catchpole K, Zhou H, Weber K. *Adv Energy Mater*, 2022, 12: 2200821
 - 136 Schulze PSC, Bett AJ, Bivour M, Caprioglio P, Gerspacher FM, Kabakli ÖS, Richter A, Stollerfoht M, Zhang Q, Neher D, Hermle M, Hillebrecht H, Glunz SW, Goldschmidt JC. *Sol RRL*, 2020, 4: 2000152
 - 137 Kim D, Jung HJ, Park IJ, Larson BW, Dunfield SP, Xiao C, Kim J, Tong J, Boonmongkolras P, Ji SG, Zhang F, Pae SR, Kim M, Kang SB, Dravid V, Berry JJ, Kim JY, Zhu K, Kim DH, Shin B. *Science*, 2020, 368: 155–160
 - 138 Xu J, Boyd CC, Yu ZJ, Palmstrom AF, Witter DJ, Larson BW, France RM, Werner J, Harvey SP, Wolf EJ, Weigand W, Manzoor S, van Hest MFAM, Berry JJ, Luther JM, Holman ZC, McGehee MD.

- Science*, 2020, 367: 1097–1104
- 139 Li R, Chen B, Ren N, Wang P, Shi B, Xu Q, Zhao H, Han W, Zhu Z, Liu J, Huang Q, Zhang D, Zhao Y, Zhang X. *Adv Mater*, 2022, 34: 2201451
 - 140 Hou Y, Aydin E, De Bastiani M, Xiao C, Isikgor FH, Xue DJ, Chen B, Chen H, Bahrami B, Chowdhury AH, Johnston A, Baek SW, Huang Z, Wei M, Dong Y, Troughton J, Jalmood R, Mirabelli AJ, Allen TG, Van Kerschaver E, Saidaminov MI, Baran D, Qiao Q, Zhu K, De Wolf S, Sargent EH. *Science*, 2020, 367: 1135–1140
 - 141 Isikgor FH, Furlan F, Liu J, Ugur E, Eswaran MK, Subbiah AS, Yengel E, De Bastiani M, Harrison GT, Zhumagali S, Howells CT, Aydin E, Wang M, Gasparini N, Allen TG, Rehman A, Van Kerschaver E, Baran D, McCulloch I, Anthopoulos TD, Schwingschlögl U, Laquai F, De Wolf S. *Joule*, 2021, 5: 1566–1586
 - 142 Zhumagali S, Isikgor FH, Maity P, Yin J, Ugur E, De Bastiani M, Subbiah AS, Mirabelli AJ, Azmi R, Harrison GT, Troughton J, Aydin E, Liu J, Allen T, Rehman A, Baran D, Mohammed OF, De Wolf S. *Adv Energy Mater*, 2021, 11: 2101662
 - 143 Zheng X, Liu J, Liu T, Aydin E, Chen M, Yan W, De Bastiani M, Allen TG, Yuan S, Kirmani AR, Baustert KN, Salvador MF, Turedi B, Alsalloum AY, Almasabi K, Kotsovos K, Gereige I, Liao LS, Luther JM, Graham KR, Mohammed OF, De Wolf S, Bakr OM. *ACS Energy Lett*, 2022, 7: 1987–1993
 - 144 Liu J, De Bastiani M, Aydin E, Harrison GT, Gao Y, Pradhan RR, Eswaran MK, Mandal M, Yan W, Seithkan A, Babics M, Subbiah AS, Ugur E, Xu F, Xu L, Wang M, Rehman AU, Razzaq A, Kang J, Azmi R, Said AA, Isikgor FH, Allen TG, Andrienko D, Schwingschlögl U, Laquai F, De Wolf S. *Science*, 2022, 377: 302–306
 - 145 Tockhorn P, Sutter J, Cruz A, Wagner P, Jäger K, Yoo D, Lang F, Griseck M, Li B, Al-Ashouri A, Köhnen E, Stollerfoht M, Neher D, Schlattmann R, Rech B, Stannowski B, Albrecht S, Becker C. *Res Square*, 2022, doi: 10.21203/rs.3.rs-1439562/v1
 - 146 Liu J, Aydin E, Yin J, De Bastiani M, Isikgor FH, Rehman AU, Yengel E, Ugur E, Harrison GT, Wang M, Gao Y, Khan JI, Babics M, Allen TG, Subbiah AS, Zhu K, Zheng X, Yan W, Xu F, Salvador MF, Bakr OM, Anthopoulos TD, Lanza M, Mohammed OF, Laquai F, De Wolf S. *Joule*, 2021, 5: 3169–3186
 - 147 De Bastiani M, Van Kerschaver E, Jeangros Q, Ur Rehman A, Aydin E, Isikgor FH, Mirabelli AJ, Babics M, Liu J, Zhumagali S, Ugur E, Harrison GT, Allen TG, Chen B, Hou Y, Shikin S, Sargent EH, Ballif C, Salvador M, De Wolf S. *ACS Energy Lett*, 2021, 6: 2944–2951
 - 148 Nogay G, Sahli F, Werner J, Monnard R, Boccard M, Despeisse M, Haug FJ, Jeangros Q, Ingenito A, Ballif C. *ACS Energy Lett*, 2019, 4: 844–845
 - 149 Sahli F, Werner J, Kamino BA, Bräuninger M, Monnard R, Paviet-Salomon B, Barraud L, Ding L, Diaz Leon JJ, Sacchetto D, Cattaneo G, Despeisse M, Boccard M, Nicolay S, Jeangros Q, Niesen B, Ballif C. *Nat Mater*, 2018, 17: 820–826
 - 150 Aydin E, Allen TG, De Bastiani M, Xu L, Ávila J, Salvador M, Van Kerschaver E, De Wolf S. *Nat Energy*, 2020, 5: 851–859
 - 151 Li Y, Shi B, Xu Q, Yan L, Ren N, Chen Y, Han W, Huang Q, Zhao Y, Zhang X. *Adv Energy Mater*, 2021, 11: 2102046
 - 152 Mao L, Yang T, Zhang H, Shi J, Hu Y, Zeng P, Li F, Gong J, Fang X, Sun Y, Liu X, Du J, Han A, Zhang L, Liu W, Meng F, Cui X, Liu Z, Liu M. *Adv Mater*, 2022, 34: 2206193
 - 153 Roß M, Severin S, Stutz MB, Wagner P, Köbler H, Favin-Lévêque M, Al-Ashouri A, Korb P, Tockhorn P, Abate A, Stannowski B, Rech B, Albrecht S. *Adv Energy Mater*, 2021, 11: 2101460
 - 154 Subbiah AS, Isikgor FH, Howells CT, De Bastiani M, Liu J, Aydin E, Furlan F, Allen TG, Xu F, Zhumagali S, Hoogland S, Sargent EH, McCulloch I, De Wolf S. *ACS Energy Lett*, 2020, 5: 3034–3040
 - 155 Chen B, Yu ZJ, Manzoor S, Wang S, Weigand W, Yu Z, Yang G, Ni Z, Dai X, Holman ZC, Huang J. *Joule*, 2020, 4: 850–864
 - 156 Yang G, Ni Z, Yu ZJ, Larson BW, Yu Z, Chen B, Alasfour A, Xiao X, Luther JM, Holman ZC, Huang J. *Nat Photon*, 2022, 16: 588–594
 - 157 Todorov T, Gershon T, Gunawan O, Lee YS, Sturdevant C, Chang LY, Guha S. *Adv Energy Mater*, 2015, 5: 1500799
 - 158 Han Q, Hsieh YT, Meng L, Wu JL, Sun P, Yao EP, Chang SY, Bae SH, Kato T, Bermudez V, Yang Y. *Science*, 2018, 361: 904–908
 - 159 Jošt M, Bertram T, Koushik D, Marquez JA, Verheijen MA, Heinemann MD, Köhnen E, Al-Ashouri A, Braunger S, Lang F, Rech B, Unold T, Creatore M, Lauermann I, Kaufmann CA, Schlattmann R, Albrecht S. *ACS Energy Lett*, 2019, 4: 583–590
 - 160 Al-Ashouri A, Magomedov A, Roß M, Jošt M, Talaikis M, Chistiakova G, Bertram T, Márquez JA, Köhnen E, Kasparavičius E, Levenco S, Gil-Escrig L, Hages CJ, Schlattmann R, Rech B, Malinauskas T, Unold T, Kaufmann CA, Korte L, Niaura G, Getautis V, Albrecht S. *Energy Environ Sci*, 2019, 12: 3356–3369
 - 161 Jošt M, Köhnen E, Al-Ashouri A, Bertram T, Tomšič Š, Magomedov A, Kasparavičius E, Kodalle T, Lipovšek B, Getautis V, Schlattmann R, Kaufmann CA, Albrecht S, Topič M. *ACS Energy Lett*, 2022, 7: 1298–1307
 - 162 Lin R, Xu J, Wei M, Wang Y, Qin Z, Liu Z, Wu J, Xiao K, Chen B, Park SM, Chen G, Atapattu HR, Graham KR, Xu J, Zhu J, Li L, Zhang C, Sargent EH, Tan H. *Nature*, 2022, 603: 73–78
 - 163 Luo X, Wu T, Wang Y, Lin X, Su H, Han Q, Han L. *Sci China Chem*, 2021, 64: 218–227
 - 164 Zhang W, Huang L, Zheng W, Zhou S, Hu X, Zhou J, Li J, Liang J, Ke W, Fang G. *Nano Energy*, 2022, 96: 107078
 - 165 Gharibzadeh S, Abdollahi Nejad B, Jakoby M, Abzieher T, Hauschild D, Moghadamzadeh S, Schwenzer JA, Brenner P, Schmager R, Haghighirad AA, Weinhardt L, Lemmer U, Richards BS, Howard IA, Paetzold UW. *Adv Energy Mater*, 2019, 9: 1803699
 - 166 Chen C, Song Z, Xiao C, Zhao D, Shrestha N, Li C, Yang G, Yao F, Zheng X, Ellingson RJ, Jiang CS, Al-Jassim M, Zhu K, Fang G, Yan Y. *Nano Energy*, 2019, 61: 141–147
 - 167 Wang Y, Gu S, Liu G, Zhang L, Liu Z, Lin R, Xiao K, Luo X, Shi J, Du J, Meng F, Li L, Liu Z, Tan H. *Sci China Chem*, 2021, 64: 2025–2034
 - 168 Li L, Wang Y, Wang X, Lin R, Luo X, Liu Z, Zhou K, Xiong S, Bao Q, Chen G, Tian Y, Deng Y, Xiao K, Wu J, Saidaminov MI, Lin H, Ma CQ, Zhao Z, Wu Y, Zhang L, Tan H. *Nat Energy*, 2022, 7: 708–717
 - 169 Wen J, Zhao Y, Liu Z, Gao H, Lin R, Wan S, Ji C, Xiao K, Gao Y, Tian Y, Xie J, Brabec CJ, Tan H. *Adv Mater*, 2022, 34: 2110356
 - 170 Zhao D, Chen C, Wang C, Junda MM, Song Z, Grice CR, Yu Y, Li C, Subedi B, Podraza NJ, Zhao X, Fang G, Xiong RG, Zhu K, Yan Y. *Nat Energy*, 2018, 3: 1093–1100
 - 171 Tong J, Song Z, Kim DH, Chen X, Chen C, Palmstrom AF, Ndione PF, Reese MO, Dunfield SP, Reid OG, Liu J, Zhang F, Harvey SP, Li Z, Christensen ST, Teeter G, Zhao D, Al-Jassim MM, van Hest MFAM, Beard MC, Shaheen SE, Berry JJ, Yan Y, Zhu K. *Science*, 2019, 364: 475–479
 - 172 Lin R, Xiao K, Qin Z, Han Q, Zhang C, Wei M, Saidaminov MI, Gao Y, Xu J, Xiao M, Li A, Zhu J, Sargent EH, Tan H. *Nat Energy*, 2019, 4: 864–873
 - 173 Xiao K, Lin R, Han Q, Hou Y, Qin Z, Nguyen HT, Wen J, Wei M, Yeddu V, Saidaminov MI, Gao Y, Luo X, Wang Y, Gao H, Zhang C, Xu J, Zhu J, Sargent EH, Tan H. *Nat Energy*, 2020, 5: 870–880
 - 174 Im J, Stoumpos CC, Jin H, Freeman AJ, Kanatzidis MG. *J Phys Chem Lett*, 2015, 6: 3503–3509
 - 175 Tong J, Jiang Q, Ferguson AJ, Palmstrom AF, Wang X, Hao J, Dunfield SP, Louks AE, Harvey SP, Li C, Lu H, France RM, Johnson SA, Zhang F, Yang M, Geisz JF, McGehee MD, Beard MC, Yan Y, Kuciauskas D, Berry JJ, Zhu K. *Nat Energy*, 2022, 7: 642–651
 - 176 Wang C, Zhao Y, Ma T, An Y, He R, Zhu J, Chen C, Ren S, Fu F, Zhao D, Li X. *Nat Energy*, 2022, 7: 744–753
 - 177 Yu Z, Yang Z, Ni Z, Shao Y, Chen B, Lin Y, Wei H, Yu ZJ, Holman Z, Huang J. *Nat Energy*, 2020, 5: 657–665
 - 178 Gao H, Lu Q, Xiao K, Han Q, Lin R, Liu Z, Li H, Li L, Luo X, Gao Y, Wang Y, Wen J, Zou Z, Zhou Y, Tan H. *Sol RRL*, 2021, 5: 2100814
 - 179 Zhao D, Wang C, Song Z, Yu Y, Chen C, Zhao X, Zhu K, Yan Y.

- ACS Energy Lett*, 2018, 3: 305–306
- 180 Zhao D, Yu Y, Wang C, Liao W, Shrestha N, Grice CR, Cimaroli AJ, Guan L, Ellingson RJ, Zhu K, Zhao X, Xiong RG, Yan Y. *Nat Energy*, 2017, 2: 17018
 - 181 Leijtens T, Bush KA, Prasanna R, McGehee MD. *Nat Energy*, 2018, 3: 828–838
 - 182 Xiao K, Lin YH, Zhang M, Oliver RDJ, Wang X, Liu Z, Luo X, Li J, Lai D, Luo H, Lin R, Xu J, Hou Y, Snaith HJ, Tan H. *Science*, 2022, 376: 762–767
 - 183 Palmstrom AF, Eperon GE, Leijtens T, Prasanna R, Habisreutinger SN, Nemeth W, Gaubling EA, Dunfield SP, Reese M, Nanayakkara S, Moot T, Werner J, Liu J, To B, Christensen ST, McGehee MD, van Hest MFAM, Luther JM, Berry JJ, Moore DT. *Joule*, 2019, 3: 2193–2204
 - 184 Qin S, Lu C, Jia Z, Wang Y, Li S, Lai W, Shi P, Wang R, Zhu C, Du J, Zhang J, Meng L, Li Y. *Adv Mater*, 2022, 34: 2108829
 - 185 Liu Y, Renna LA, Bag M, Page ZA, Kim P, Choi J, Emrick T, Venkataraman D, Russell TP. *ACS Appl Mater Interfaces*, 2016, 8: 7070–7076
 - 186 Aqoma H, Imran IF, Wibowo FTA, Krishna NV, Lee W, Sarker AK, Ryu DY, Jang S. *Adv Energy Mater*, 2020, 10: 2001188
 - 187 Li Z, Wu S, Zhang J, Lee KC, Lei H, Lin F, Wang Z, Zhu Z, Jen AKY. *Adv Energy Mater*, 2020, 10: 2000361
 - 188 Xie S, Xia R, Chen Z, Tian J, Yan L, Ren M, Li Z, Zhang G, Xue Q, Yip HL, Cao Y. *Nano Energy*, 2020, 78: 105238
 - 189 Chen X, Jia Z, Chen Z, Jiang T, Bai L, Tao F, Chen J, Chen X, Liu T, Xu X, Yang C, Shen W, Sha WEI, Zhu H, Yang YM. *Joule*, 2020, 4: 1594–1606
 - 190 Xie Y, Yao Q, Zeng Z, Xue Q, Niu T, Xia R, Cheng Y, Lin F, Tsang S, Jen AK, Yip H, Cao Y. *Adv Funct Mater*, 2022, 32: 2112126
 - 191 Chen W, Li D, Chen X, Chen H, Liu S, Yang H, Li X, Shen Y, Ou X, Yang YM, Jiang L, Li Y, Li Y. *Adv Funct Mater*, 2021, 32: 2109321
 - 192 Chen W, Zhu Y, Xiu J, Chen G, Liang H, Liu S, Xue H, Birgersson E, Ho JW, Qin X, Lin J, Ma R, Liu T, He Y, Ng AMC, Guo X, He Z, Yan H, Djurišić AB, Hou Y. *Nat Energy*, 2022, 7: 229–237
 - 193 Brinkmann KO, Becker T, Zimmermann F, Kreusel C, Gahlmann T, Theisen M, Haeger T, Olthof S, Tüchtmann C, Günster M, Maschwitz T, Göbelsmann F, Koch C, Hertel D, Caprioglio P, Peña-Camargo F, Perdigón-Toro L, Al-Ashouri A, Merten L, Hinderhofer A, Gomell L, Zhang S, Schreiber F, Albrecht S, Meerholz K, Neher D, Stollerfoht M, Riedl T. *Nature*, 2022, 604: 280–286
 - 194 Jeong J, Kim M, Seo J, Lu H, Ahlawat P, Mishra A, Yang Y, Hope MA, Eickemeyer FT, Kim M, Yoon YJ, Choi IW, Darwich BP, Choi SJ, Jo Y, Lee JH, Walker B, Zakeeruddin SM, Emsley L, Rothlisberger U, Hagfeldt A, Kim DS, Grätzel M, Kim JY. *Nature*, 2021, 592: 381–385
 - 195 Siegler TD, Dawson A, Lobaccaro P, Ung D, Beck ME, Nilsen G, Tinker LL. *ACS Energy Lett*, 2022, 7: 1728–1734
 - 196 Li D, Zhang D, Lim K, Hu Y, Rong Y, Mei A, Park N, Han H. *Adv Funct Mater*, 2020, 31: 2008621
 - 197 Li Z, Klein TR, Kim DH, Yang M, Berry JJ, van Hest MFAM, Zhu K. *Nat Rev Mater*, 2018, 3: 18017
 - 198 Yu X, Li J, Mo Y, Xiang T, Ku Z, Huang F, Long F, Peng Y, Cheng YB. *J Energy Chem*, 2022, 67: 201–208
 - 199 Kim YY, Yang TY, Suhonen R, Kempainen A, Hwang K, Jeon NJ, Seo J. *Nat Commun*, 2020, 11: 5146
 - 200 Schackmar F, Eggers H, Frericks M, Richards BS, Lemmer U, Hernandez-Sosa G, Paetzold UW. *Adv Mater Technol*, 2020, 6: 2000271
 - 201 Eggers H, Schackmar F, Abzieher T, Sun Q, Lemmer U, Vaynzof Y, Richards BS, Hernandez-Sosa G, Paetzold UW. *Adv Energy Mater*, 2019, 10: 1903184
 - 202 Ye F, Chen H, Xie F, Tang W, Yin M, He J, Bi E, Wang Y, Yang X, Han L. *Energy Environ Sci*, 2016, 9: 2295–2301
 - 203 Ye F, Tang W, Xie F, Yin M, He J, Wang Y, Chen H, Qiang Y, Yang X, Han L. *Adv Mater*, 2017, 29: 1701440
 - 204 Chen H, Ye F, Tang W, He J, Yin M, Wang Y, Xie F, Bi E, Yang X, Grätzel M, Han L. *Nature*, 2017, 550: 92–95
 - 205 Huang F, Pascoe AR, Wu WQ, Ku Z, Peng Y, Zhong J, Caruso RA, Cheng YB. *Adv Mater*, 2017, 29: 1601715
 - 206 Yang Z, Zhang W, Wu S, Zhu H, Liu Z, Liu Z, Jiang Z, Chen R, Zhou J, Lu Q, Xiao Z, Shi L, Chen H, Ono LK, Zhang S, Zhang Y, Qi Y, Han L, Chen W. *Sci Adv*, 2021, 7: eabg3749
 - 207 Huang F, Dkhissi Y, Huang W, Xiao M, Benesperi I, Rubanov S, Zhu Y, Lin X, Jiang L, Zhou Y, Gray-Weale A, Etheridge J, McNeill CR, Caruso RA, Bach U, Spiccia L, Cheng YB. *Nano Energy*, 2014, 10: 10–18
 - 208 Dai X, Deng Y, Van Brackel CH, Chen S, Rudd PN, Xiao X, Lin Y, Chen B, Huang J. *Adv Energy Mater*, 2019, 10: 1903108
 - 209 Deng Y, Van Brackel CH, Dai X, Zhao J, Chen B, Huang J. *Sci Adv*, 2019, 5: eaax7537
 - 210 Li X, Bi D, Yi C, Décoppet JD, Luo J, Zakeeruddin SM, Hagfeldt A, Grätzel M. *Science*, 2016, 353: 58–62
 - 211 Gao LL, Liang LS, Song XX, Ding B, Yang GJ, Fan B, Li CX, Li CJ. *J Mater Chem A*, 2016, 4: 3704–3710
 - 212 Ding B, Gao L, Liang L, Chu Q, Song X, Li Y, Yang G, Fan B, Wang M, Li C, Li C. *ACS Appl Mater Interfaces*, 2016, 8: 20067–20073
 - 213 Cai L, Liang L, Wu J, Ding B, Gao L, Fan B. *J Semicond*, 2017, 38: 014006
 - 214 Yoo JJ, Seo G, Chua MR, Park TG, Lu Y, Rotermund F, Kim YK, Moon CS, Jeon NJ, Correa-Baena JP, Bulović V, Shin SS, Bawendi MG, Seo J. *Nature*, 2021, 590: 587–593
 - 215 Yoo JW, Jang J, Kim U, Lee Y, Ji SG, Noh E, Hong S, Choi M, Seok SI. *Joule*, 2021, 5: 2420–2436
 - 216 Li H, Zhou J, Tan L, Li M, Jiang C, Wang S, Zhao X, Liu Y, Zhang Y, Ye Y, Tress W, Yi C. *Sci Adv*, 2022, 8: eabo7422
 - 217 Liang G, Lan H, Fan P, Lan C, Zheng Z, Peng H, Luo J. *Coatings*, 2018, 8: 256
 - 218 Borchert J, Milot RL, Patel JB, Davies CL, Wright AD, Martínez Maestro L, Snaith HJ, Herz LM, Johnston MB. *ACS Energy Lett*, 2017, 2: 2799–2804
 - 219 Qiu L, He S, Jiang Y, Son DY, Ono LK, Liu Z, Kim T, Bouloumis T, Kazaoui S, Qi Y. *J Mater Chem A*, 2019, 7: 6920–6929
 - 220 Di Giacomo F, Shanmugam S, Fledderus H, Bruijinaers BJ, Verhees WJH, Dorenkamper MS, Veenstra SC, Qiu W, Gehlhaar R, Merckx T, Aernouts T, Andriessen R, Galagan Y. *Sol Energy Mater Sol Cells*, 2018, 181: 53–59
 - 221 Bu T, Li J, Zheng F, Chen W, Wen X, Ku Z, Peng Y, Zhong J, Cheng YB, Huang F. *Nat Commun*, 2018, 9: 4609
 - 222 Kim M, Jeong J, Lu H, Lee TK, Eickemeyer FT, Liu Y, Choi IW, Choi SJ, Jo Y, Kim HB, Mo SI, Kim YK, Lee H, An NG, Cho S, Tress WR, Zakeeruddin SM, Hagfeldt A, Kim JY, Grätzel M, Kim DS. *Science*, 2022, 375: 302–306
 - 223 Kim H, Lee KS, Paik MJ, Lee DY, Lee S, Choi E, Yun JS, Seok SI. *Adv Funct Mater*, 2021, 32: 2110473
 - 224 Hu M, Wu X, Tan WL, Tan B, Scully AD, Ding L, Zhou C, Xiong Y, Huang F, Simonov AN, Bach U, Cheng YB, Wang S, Lu J. *ACS Appl Mater Interfaces*, 2020, 12: 8260–8270
 - 225 Xia J, Zhang Y, Xiao C, Brooks KG, Chen M, Luo J, Yang H, Klipfel NID, Zou J, Shi Y, Yao X, Chen J, Luther JM, Lin H, Asiri AM, Jia C, Nazeeruddin MK. *Joule*, 2022, 6: 1689–1709
 - 226 Wu G, Zhang Y, Kaneko R, Kojima Y, Islam A, Sugawa K, Otsuki J, Liu S. *J Energy Chem*, 2020, 48: 293–298
 - 227 Xu Y, Wang S, Gu L, Yuan N, Ding J. *Sol RRL*, 2021, 5: 2000733
 - 228 Du M, Zhao S, Duan L, Cao Y, Wang H, Sun Y, Wang L, Zhu X, Feng J, Liu L, Jiang X, Dong Q, Shi Y, Wang K, Liu SF. *Joule*, 2022, 6: 1931–1943
 - 229 Deng Y, Zheng X, Bai Y, Wang Q, Zhao J, Huang J. *Nat Energy*, 2018, 3: 560–566
 - 230 Chang NL, Yi Ho-Baillie AW, Basore PA, Young TL, Evans R, Egan RJ. *Prog Photovolt-Res Appl*, 2017, 25: 390–405
 - 231 Gao L, Chen L, Huang S, Li X, Yang G. *ACS Appl Energy Mater*, 2019, 2: 3851–3859
 - 232 Agresti A, Pescetelli S, Palma AL, Martín-García B, Najafi L, Bel-

- lani S, Moreels I, Prato M, Bonaccorso F, Di Carlo A. *ACS Energy Lett*, 2019, 4: 1862–1871
- 233 Li X, Fu S, Zhang W, Ke S, Song W, Fang J. *Sci Adv*, 2020, 6: eabd1580
- 234 Zhang H, Xiao J, Shi J, Su H, Luo Y, Li D, Wu H, Cheng YB, Meng Q. *Adv Funct Mater*, 2018, 28: 1802985
- 235 Brooks KG, Nazeeruddin MK. *Adv Energy Mater*, 2021, 11: 2101149
- 236 Bu T, Ono LK, Li J, Su J, Tong G, Zhang W, Liu Y, Zhang J, Chang J, Kazaoui S, Huang F, Cheng YB, Qi Y. *Nat Energy*, 2022, 7: 528–536
- 237 Rakocovic L, Schöpe G, Turan B, Genoe J, Aernouts T, Haas S, Gehlhaar R, Poortmans J. *Prog Photovolt Res Appl*, 2020, 28: 1120–1127
- 238 Wang R, Mujahid M, Duan Y, Wang Z, Xue J, Yang Y. *Adv Funct Mater*, 2019, 29: 1808843
- 239 Svane KL, Forse AC, Grey CP, Kieslich G, Cheetham AK, Walsh A, Butler KT. *J Phys Chem Lett*, 2017, 8: 6154–6159
- 240 Li N, Niu X, Chen Q, Zhou H. *Chem Soc Rev*, 2020, 49: 8235–8286
- 241 Cheng Y, Ding L. *Energy Environ Sci*, 2021, 14: 3233–3255
- 242 Niu T, Chao L, Dong X, Fu L, Chen Y. *J Phys Chem Lett*, 2022, 13: 1845–1854
- 243 Zhang S, Liu Z, Zhang W, Jiang Z, Chen W, Chen R, Huang Y, Yang Z, Zhang Y, Han L, Chen W. *Adv Energy Mater*, 2020, 10: 2001610
- 244 Li Z, Yang M, Park JS, Wei SH, Berry JJ, Zhu K. *Chem Mater*, 2016, 28: 284–292
- 245 Turren-Cruz SH, Hagfeldt A, Saliba M. *Science*, 2018, 362: 449–453
- 246 Bush KA, Palmstrom AF, Yu ZJ, Boccard M, Cheacharoen R, Mailoa JP, McMeekin DP, Hoyer RLZ, Bailie CD, Leijtens T, Peters IM, Minichetti MC, Rolston N, Prasanna R, Sofia S, Harwood D, Ma W, Moghadam F, Snaith HJ, Buonassisi T, Holman ZC, Bent SF, McGehee MD. *Nat Energy*, 2017, 2: 17009
- 247 Zhou N, Shen Y, Zhang Y, Xu Z, Zheng G, Li L, Chen Q, Zhou H. *Small*, 2017, 13: 1700484
- 248 Kim G, Min H, Lee KS, Lee DY, Yoon SM, Seok SI. *Science*, 2020, 370: 108–112
- 249 Liu C, Yang Y, Syzgantseva OA, Ding Y, Syzgantseva MA, Zhang X, Asiri AM, Dai S, Nazeeruddin MK. *Adv Mater*, 2020, 32: 2002632
- 250 Wang Y, Dar MI, Ono LK, Zhang T, Kan M, Li Y, Zhang L, Wang X, Yang Y, Gao X, Qi Y, Grätzel M, Zhao Y. *Science*, 2019, 365: 591–595
- 251 Zhao Y, Heumueller T, Zhang J, Luo J, Kasian O, Langner S, Kupfer C, Liu B, Zhong Y, Elia J, Osvet A, Wu J, Liu C, Wan Z, Jia C, Li N, Hauch J, Brabec CJ. *Nat Energy*, 2022, 7: 144–152
- 252 Christians JA, Schulz P, Tinkham JS, Schloemer TH, Harvey SP, Tremolet de Villers BJ, Sellinger A, Berry JJ, Luther JM. *Nat Energy*, 2018, 3: 68–74
- 253 Correa-Baena JP, Luo Y, Brenner TM, Snaider J, Sun S, Li X, Jensen MA, Hartono NTP, Nienhaus L, Wieghold S, Poindexter JR, Wang S, Meng YS, Wang T, Lai B, Holt MV, Cai Z, Bawendi MG, Huang L, Buonassisi T, Fenning DP. *Science*, 2019, 363: 627–631
- 254 Doherty TAS, Winchester AJ, Macpherson S, Johnstone DN, Pareek V, Tennyson EM, Kosar S, Kosasih FU, Anaya M, Abdi-Jalebi M, Andaji-Garmaroudi Z, Wong EL, Madéo J, Chiang YH, Park JS, Jung YK, Petoukhoff CE, Divitini G, Man MKL, Ducati C, Walsh A, Midgley PA, Dani KM, Stranks SD. *Nature*, 2020, 580: 360–366
- 255 Macpherson S, Doherty TAS, Winchester AJ, Kosar S, Johnstone DN, Chiang YH, Galkowski K, Anaya M, Frohna K, Iqbal AN, Nagane S, Roose B, Andaji-Garmaroudi Z, Orr KWP, Parker JE, Midgley PA, Dani KM, Stranks SD. *Nature*, 2022, 607: 294–300
- 256 Li N, Tao S, Chen Y, Niu X, Onwudinanti CK, Hu C, Qiu Z, Xu Z, Zheng G, Wang L, Zhang Y, Li L, Liu H, Lun Y, Hong J, Wang X, Liu Y, Xie H, Gao Y, Bai Y, Yang S, Brocks G, Chen Q, Zhou H. *Nat Energy*, 2019, 4: 408–415
- 257 Hoeffler SF, Trimmel G, Rath T. *Monatsh Chem*, 2017, 148: 795–826
- 258 Correa-Baena JP, Saliba M, Buonassisi T, Grätzel M, Abate A, Tress W, Hagfeldt A. *Science*, 2017, 358: 739–744
- 259 Steele JA, Jin H, Dovgaliuk I, Berger RF, Braeckvelt T, Yuan H, Martin C, Solano E, Lejaeghere K, Rogge SMJ, Notebaert C, Vandezande W, Janssen KPF, Goderis B, Debroye E, Wang YK, Dong Y, Ma D, Saidaminov M, Tan H, Lu Z, Dyadkin V, Chernyshov D, Van Speybroeck V, Sargent EH, Hofkens J, Roelofs MJB. *Science*, 2019, 365: 679–684
- 260 Zheng X, Chen B, Dai J, Fang Y, Bai Y, Lin Y, Wei H, Zeng XC, Huang J. *Nat Energy*, 2017, 2: 17102
- 261 Kim H, Lee S, Lee DY, Paik MJ, Na H, Lee J, Seok SI. *Adv Energy Mater*, 2019, 9: 1902740
- 262 Liu X, Webb T, Dai L, Ji K, Smith JA, Kilbride RC, Yavari M, Bi J, Ren A, Huang Y, Wang Z, Shen Y, Shao G, Sweeney SJ, Hinder S, Li H, Lidzey DG, Stranks SD, Greenham NC, Silva SRP, Zhang W. *Energy Environ Mater*, 2022, 5: 670–682
- 263 Zhang F, Park SY, Yao C, Lu H, Dunfield SP, Xiao C, Uličná S, Zhao X, Du Hill L, Chen X, Wang X, Mundt LE, Stone KH, Schelhas LT, Teeter G, Parkin S, Ratcliff EL, Loo YL, Berry JJ, Beard MC, Yan Y, Larson BW, Zhu K. *Science*, 2022, 375: 71–76
- 264 Zhao X, Liu T, Burlingame QC, Liu T, Holley Iii R, Cheng G, Yao N, Gao F, Loo YL. *Science*, 2022, 377: 307–310
- 265 Zai H, Su J, Zhu C, Chen Y, Ma Y, Zhang P, Ma S, Zhang X, Xie H, Fan R, Huang Z, Li N, Zhang Y, Li Y, Bai Y, Gao Z, Wang X, Hong J, Sun K, Chang J, Zhou H, Chen Q. *Joule*, 2021, 5: 2148–2163
- 266 Leijtens T, Eperon GE, Pathak S, Abate A, Lee MM, Snaith HJ. *Nat Commun*, 2013, 4: 2885
- 267 Li N, Niu X, Pei F, Liu H, Cao Y, Liu Y, Xie H, Gao Y, Chen Q, Mo F, Zhou H. *Sol RRL*, 2020, 4: 1900217
- 268 Rombach FM, Haque SA, Macdonald TJ. *Energy Environ Sci*, 2021, 14: 5161–5190
- 269 Jeon NJ, Na H, Jung EH, Yang TY, Lee YG, Kim G, Shin HW, Il Seok S, Lee J, Seo J. *Nat Energy*, 2018, 3: 682–689
- 270 Jeong M, Choi IW, Go EM, Cho Y, Kim M, Lee B, Jeong S, Jo Y, Choi HW, Lee J, Bae JH, Kwak SK, Kim DS, Yang C. *Science*, 2020, 369: 1615–1620
- 271 Wang J, Chen X, Jiang F, Luo Q, Zhang L, Tan M, Xie M, Li YQ, Zhou Y, Su W, Li Y, Ma CQ. *Sol RRL*, 2018, 2: 1800118
- 272 Lim J, Choi E, Kim M, Lee M, Chen D, Green MA, Seidel J, Kim C, Park J, Hao X, Yun JS. *ACS Appl Mater Interfaces*, 2022, 14: 20866–20874
- 273 Boyd CC, Cheacharoen R, Leijtens T, McGehee MD. *Chem Rev*, 2019, 119: 3418–3451
- 274 Fan R, Wang L, Chen Y, Zheng G, Li L, Li Z, Zhou H. *J Mater Chem A*, 2017, 5: 12034–12042
- 275 Ming W, Yang D, Li T, Zhang L, Du MH. *Adv Sci*, 2018, 5: 1700662
- 276 Wu S, Chen R, Zhang S, Babu BH, Yue Y, Zhu H, Yang Z, Chen C, Chen W, Huang Y, Fang S, Liu T, Han L, Chen W. *Nat Commun*, 2019, 10: 1161
- 277 Wang L, Li GR, Zhao Q, Gao XP. *Energy Storage Mater*, 2017, 7: 40–47
- 278 Chen R, Zhang W, Guan X, Raza H, Zhang S, Zhang Y, Troshin PA, Kuklin SA, Liu Z, Chen W. *Adv Funct Mater*, 2022, 32: 2200651
- 279 Gordon RG. *MRS Bull*, 2000, 25: 52–57
- 280 Wu Z, Chen Z, Du X, Logan JM, Sippel J, Nikolou M, Kamaras K, Reynolds JR, Tanner DB, Hebard AF, Rinzler AG. *Science*, 2004, 305: 1273–1276
- 281 Zhang C, Liang S, Liu W, Eickemeyer FT, Cai X, Zhou K, Bian J, Zhu H, Zhu C, Wang N, Wang Z, Zhang J, Wang Y, Hu J, Ma H, Xin C, Zakeeruddin SM, Grätzel M, Shi Y. *Nat Energy*, 2021, 6: 1154–1163
- 282 Cheng Y, Xie C, Liu X, Zhu G, Li HW, Venkataraj S, Tan ZK, Ding L, Aberle AG, Lin F. *Sci Bull*, 2020, 65: 607–610
- 283 Kaltenbrunner M, Adam G, Glowacki ED, Drack M, Schwödiauer R, Leonat L, Apaydin DH, Groiss H, Scharber MC, White MS, Sariciftci NS, Bauer S. *Nat Mater*, 2015, 14: 1032–1039
- 284 Hu T, Becker T, Pourdavoud N, Zhao J, Brinkmann KO, Heiderhoff R, Gahlmann T, Huang Z, Olthof S, Meerholz K, Többsen D, Cheng B, Chen Y, Riedl T. *Adv Mater*, 2017, 29: 1606656

- 285 Jiang J, Mavrić A, Pastukhova N, Valant M, Zeng Q, Fan Z, Zhang B, Li Y. *Sol RRL*, 2022, 6: 2200091
- 286 Bi E, Chen H, Xie F, Wu Y, Chen W, Su Y, Islam A, Grätzel M, Yang X, Han L. *Nat Commun*, 2017, 8: 15330
- 287 Boyd CC, Cheacharoen R, Bush KA, Prasanna R, Leijtens T, McGehee MD. *ACS Energy Lett*, 2018, 3: 1772–1778
- 288 Lin X, Su H, He S, Song Y, Wang Y, Qin Z, Wu Y, Yang X, Han Q, Fang J, Zhang Y, Segawa H, Grätzel M, Han L. *Nat Energy*, 2022, 7: 520–527
- 289 Yang J, Cao Q, Wang T, Yang B, Pu X, Zhang Y, Chen H, Tojiboyev I, Li Y, Etgar L, Li X, Hagfeldt A. *Energy Environ Sci*, 2022, 15: 2154–2163
- 290 Zhao J, Zheng X, Deng Y, Li T, Shao Y, Gruverman A, Shield J, Huang J. *Energy Environ Sci*, 2016, 9: 3650–3656
- 291 Xiao Z, Yuan Y, Shao Y, Wang Q, Dong Q, Bi C, Sharma P, Gruverman A, Huang J. *Nat Mater*, 2015, 14: 193–198
- 292 Yuan Y, Huang J. *Acc Chem Res*, 2016, 49: 286–293
- 293 Zai H, Ma Y, Chen Q, Zhou H. *J Energy Chem*, 2021, 63: 528–549
- 294 Li N, Jia Y, Guo Y, Zhao N. *Adv Mater*, 2022, 34: 2108102
- 295 Zhang T, Hu C, Yang S. *Small Methods*, 2020, 4: 1900552
- 296 Zhao Y, Zhou WK, Han Z, Yu D, Zhao Q. *Phys Chem Chem Phys*, 2021, 23: 94–106
- 297 Yuan Y, Chae J, Shao Y, Wang Q, Xiao Z, Centrone A, Huang J. *Adv Energy Mater*, 2015, 5: 1500615
- 298 Yuan Y, Wang Q, Shao Y, Lu H, Li T, Gruverman A, Huang J. *Adv Energy Mater*, 2016, 6: 1501803
- 299 Nie W, Blancon JC, Neukirch AJ, Appavoo K, Tsai H, Chhowalla M, Alam MA, Sfeir MY, Katan C, Even J, Tretiak S, Crochet JJ, Gupta G, Mohite AD. *Nat Commun*, 2016, 7: 11574
- 300 Huang F, Jiang L, Pascoe AR, Yan Y, Bach U, Spiccia L, Cheng YB. *Nano Energy*, 2016, 27: 509–514
- 301 Ni Z, Jiao H, Fei C, Gu H, Xu S, Yu Z, Yang G, Deng Y, Jiang Q, Liu Y, Yan Y, Huang J. *Nat Energy*, 2022, 7: 65–73
- 302 Wang S, Jiang Y, Juarez-Perez EJ, Ono LK, Qi Y. *Nat Energy*, 2017, 2: 16195
- 303 Guerrero A, You J, Aranda C, Kang YS, Garcia-Belmonte G, Zhou H, Bisquert J, Yang Y. *ACS Nano*, 2016, 10: 218–224
- 304 Koushik D, Verhees WJH, Kuang Y, Veenstra S, Zhang D, Verheijen MA, Creatore M, Schropp REI. *Energy Environ Sci*, 2017, 10: 91–100
- 305 Lin Y, Bai Y, Fang Y, Chen Z, Yang S, Zheng X, Tang S, Liu Y, Zhao J, Huang J. *J Phys Chem Lett*, 2018, 9: 654–658
- 306 Bai Y, Dong Q, Shao Y, Deng Y, Wang Q, Shen L, Wang D, Wei W, Huang J. *Nat Commun*, 2016, 7: 12806
- 307 Wei D, Ma F, Wang R, Dou S, Cui P, Huang H, Ji J, Jia E, Jia X, Sajid S, Elseman AM, Chu L, Li Y, Jiang B, Qiao J, Yuan Y, Li M. *Adv Mater*, 2018, 30: 1707583
- 308 Chen W, Han B, Hu Q, Gu M, Zhu Y, Yang W, Zhou Y, Luo D, Liu FZ, Cheng R, Zhu R, Feng SP, Djurišić AB, Russell TP, He Z. *Sci Bull*, 2021, 66: 991–1002
- 309 Dunfield SP, Bliss L, Zhang F, Luther JM, Zhu K, Hest MFAM, Reese MO, Berry JJ. *Adv Energy Mater*, 2020, 10: 1904054
- 310 Deng Y, Xiao Z, Huang J. *Adv Energy Mater*, 2015, 5: 1500721
- 311 deQuilettes DW, Zhang W, Burlakov VM, Graham DJ, Leijtens T, Osherov A, Bulović V, Snaith HJ, Ginger DS, Stranks SD. *Nat Commun*, 2016, 7: 11683
- 312 Zhang H, Fu X, Tang Y, Wang H, Zhang C, Yu WW, Wang X, Zhang Y, Xiao M. *Nat Commun*, 2019, 10: 1088
- 313 Lin Y, Chen B, Fang Y, Zhao J, Bao C, Yu Z, Deng Y, Rudd PN, Yan Y, Yuan Y, Huang J. *Nat Commun*, 2018, 9: 4981
- 314 Zhao YC, Zhou WK, Zhou X, Liu KH, Yu DP, Zhao Q. *Light Sci Appl*, 2017, 6: e16243
- 315 Xing J, Wang Q, Dong Q, Yuan Y, Fang Y, Huang J. *Phys Chem Chem Phys*, 2016, 18: 30484–30490
- 316 Kerner RA, Xu Z, Larson BW, Rand BP. *Joule*, 2021, 5: 2273–2295
- 317 Hoke ET, Slotcavage DJ, Dohner ER, Bowring AR, Karunadasa HI, McGehee MD. *Chem Sci*, 2015, 6: 613–617
- 318 Chen B, Song J, Dai X, Liu Y, Rudd PN, Hong X, Huang J. *Adv Mater*, 2019, 31: 1902413
- 319 Khenkin MV, Katz EA, Abate A, Bardizza G, Berry JJ, Brabec C, Brunetti F, Bulović V, Burlingame Q, Di Carlo A, Cheacharoen R, Cheng YB, Colmann A, Cros S, Domanski K, Duszka M, Fell CJ, Forrest SR, Galagan Y, Di Girolamo D, Grätzel M, Hagfeldt A, von Hauff E, Hoppe H, Kettle J, Köbler H, Leite MS, Liu S, Loo YL, Luther JM, Ma CQ, Madsen M, Manceau M, Matheron M, McGehee M, Meitzner R, Nazeeruddin MK, Nogueira AF, Odabasi Ç, Osherov A, Park NG, Reese MO, De Rossi F, Saliba M, Schubert US, Snaith HJ, Stranks SD, Tress W, Troshin PA, Turkovic V, Veenstra S, Visoly-Fisher I, Walsh A, Watson T, Xie H, Yıldırım R, Zakeeruddin SM, Zhu K, Lira-Cantu M. *Nat Energy*, 2020, 5: 35–49
- 320 Yin WJ, Shi T, Yan Y. *Appl Phys Lett*, 2014, 104: 063903
- 321 Deng Y, Xu S, Chen S, Xiao X, Zhao J, Huang J. *Nat Energy*, 2021, 6: 633–641
- 322 Aristidou N, Eames C, Sanchez-Molina I, Bu X, Kosco J, Islam MS, Haque SA. *Nat Commun*, 2017, 8: 15218
- 323 Yuan Y, Li T, Wang Q, Xing J, Gruverman A, Huang J. *Sci Adv*, 2017, 3: e1602164
- 324 Lin D, Shi T, Xie H, Wan F, Ren X, Liu K, Zhao Y, Ke L, Lin Y, Gao Y, Xu X, Xie W, Liu P, Yuan Y. *Adv Energy Mater*, 2021, 11: 2002552
- 325 Mosconi E, De Angelis F. *ACS Energy Lett*, 2016, 1: 182–188
- 326 Tong CJ, Li L, Liu LM, Prezhdo OV. *J Am Chem Soc*, 2020, 142: 3060–3068
- 327 Zhao J, Deng Y, Wei H, Zheng X, Yu Z, Shao Y, Shield JE, Huang J. *Sci Adv*, 2017, 3: eaao5616
- 328 Uddin A, Upama M, Yi H, Duan L. *Coatings*, 2019, 9: 65
- 329 Ma S, Yuan G, Zhang Y, Yang N, Li Y, Chen Q. *Energy Environ Sci*, 2022, 15: 13–55
- 330 Bella F, Griffini G, Correa-Baena JP, Saracco G, Grätzel M, Hagfeldt A, Turri S, Gerbaldi C. *Science*, 2016, 354: 203–206
- 331 Han Y, Meyer S, Dkhissi Y, Weber K, Pringle JM, Bach U, Spiccia L, Cheng YB. *J Mater Chem A*, 2015, 3: 8139–8147
- 332 Weerasinghe HC, Dkhissi Y, Scully AD, Caruso RA, Cheng YB. *Nano Energy*, 2015, 18: 118–125
- 333 Ramasamy E, Karthikeyan V, Rameshkumar K, Veerappan G. *Mater Lett*, 2019, 250: 51–54
- 334 Lee YI, Jeon NJ, Kim BJ, Shim H, Yang TY, Seok SI, Seo J, Im SG. *Adv Energy Mater*, 2018, 8: 1701928
- 335 Fu Z, Xu M, Sheng Y, Yan Z, Meng J, Tong C, Li D, Wan Z, Ming Y, Mei A, Hu Y, Rong Y, Han H. *Adv Funct Mater*, 2019, 29: 1809129
- 336 Cheacharoen R, Rolston N, Harwood D, Bush KA, Dauskardt RH, McGehee MD. *Energy Environ Sci*, 2018, 11: 144–150
- 337 Shi L, Young TL, Kim J, Sheng Y, Wang L, Chen Y, Feng Z, Keevers MJ, Hao X, Verlinden PJ, Green MA, Ho-Baillie AWY. *ACS Appl Mater Interfaces*, 2017, 9: 25073–25081
- 338 Shi L, Bucknall MP, Young TL, Zhang M, Hu L, Bing J, Lee DS, Kim J, Wu T, Takamure N, McKenzie DR, Huang S, Green MA, Ho-Baillie AWY. *Science*, 2020, 368: eaba2412
- 339 Liu T, Zhou Y, Li Z, Zhang L, Ju M, Luo D, Yang Y, Yang M, Kim DH, Yang W, Padture NP, Beard MC, Zeng XC, Zhu K, Gong Q, Zhu R. *Adv Energy Mater*, 2018, 8: 1800232
- 340 McKenna B, Troughton JR, Watson TM, Evans RC. *RSC Adv*, 2017, 7: 32942–32951
- 341 Lyu M, Yun J, Chen P, Hao M, Wang L. *Adv Energy Mater*, 2017, 7: 1602512
- 342 Wei X, Xiao M, Wang B, Wang C, Li Y, Dou J, Cui Z, Dou J, Wang H, Ma S, Zhu C, Yuan G, Yang N, Song T, Zhou H, Chen H, Bai Y, Chen Q. *Angew Chem Int Ed*, 2022, 61:
- 343 Jiang Y, Qiu L, Juarez-Perez EJ, Ono LK, Hu Z, Liu Z, Wu Z, Meng L, Wang Q, Qi Y. *Nat Energy*, 2019, 4: 585–593
- 344 Li S, Xu LD, Zhao S. *Inf Syst Front*, 2014, 17: 243–259
- 345 Gasparini N, Salleo A, McCulloch I, Baran D. *Nat Rev Mater*, 2019,

- 4: 229–242
- 346 Song D, Li M, Li Y, Zhao X, Jiang B, Jiang Y. *ACS Appl Mater Interfaces*, 2014, 6: 7126–7132
- 347 Yang C, Qu JR, Wu ZY. *Sol Energy*, 2021, 214: 542–550
- 348 Kao MH, Shen CH, Yu PC, Huang WH, Chueh YL, Shieh JM. *Sci Rep*, 2017, 7: 12706
- 349 Chung J, Shin SS, Hwang K, Kim G, Kim KW, Lee DS, Kim W, Ma BS, Kim YK, Kim TS, Seo J. *Energy Environ Sci*, 2020, 13: 4854–4861
- 350 Meng X, Hu X, Zhang Y, Huang Z, Xing Z, Gong C, Rao L, Wang H, Wang F, Hu T, Tan L, Song Y, Chen Y. *Adv Funct Mater*, 2021, 31: 2106460
- 351 Xing Z, Lin S, Meng X, Hu T, Li D, Fan B, Cui Y, Li F, Hu X, Chen Y. *Adv Funct Mater*, 2021, 31: 2107726
- 352 Dong Q, Chen M, Liu Y, Eickemeyer FT, Zhao W, Dai Z, Yin Y, Jiang C, Feng J, Jin S, Liu SF, Zakeeruddin SM, Grätzel M, Padture NP, Shi Y. *Joule*, 2021, 5: 1587–1601
- 353 Cappel UB, Svanström S, Lanzilotto V, Johansson FOL, Aitola K, Philippe B, Giangrisostomi E, Ovsyannikov R, Leitner T, Föhlisch A, Svensson S, Mårtensson N, Boschloo G, Lindblad A, Rensmo H. *ACS Appl Mater Interfaces*, 2017, 9: 34970–34978
- 354 Mathews I, Kantareddy SN, Buonassisi T, Peters IM. *Joule*, 2019, 3: 1415–1426
- 355 Venkateswararao A, Ho JKW, So SK, Liu SW, Wong KT. *Mater Sci Eng-R-Rep*, 2020, 139: 100517
- 356 Cui Y, Hong L, Zhang T, Meng H, Yan H, Gao F, Hou J. *Joule*, 2021, 5: 1016–1023
- 357 Chen CY, Chang JH, Chiang KM, Lin HL, Hsiao SY, Lin HW. *Adv Funct Mater*, 2015, 25: 7064–7070
- 358 Li M, Zhao C, Wang Z, Zhang C, Lee HKH, Pockett A, Barbé J, Tsoi WC, Yang Y, Carnie MJ, Gao X, Yang W, Durrant JR, Liao L, Jain SM. *Adv Energy Mater*, 2018, 8: 1801509
- 359 He X, Chen J, Ren X, Zhang L, Liu Y, Feng J, Fang J, Zhao K, Liu SF. *Adv Mater*, 2021, 33: 2100770
- 360 Wang KL, Yang YG, Lou YH, Li M, Igbari F, Cao JJ, Chen J, Yang WF, Dong C, Li L, Tai RZ, Wang ZK. *eScience*, 2021, 1: 53–59
- 361 Chen CH, Su ZH, Lou YH, Yu YJ, Wang KL, Liu GL, Shi YR, Chen J, Cao JJ, Zhang L, Gao XY, Wang ZK. *Adv Mater*, 2022, 34: 2200320
- 362 Yang WF, Cao JJ, Dong C, Li M, Tian QS, Wang ZK, Liao LS. *Appl Phys Lett*, 2021, 118: 023501
- 363 Yang D, Yang R, Priya S, Liu SF. *Angew Chem Int Ed*, 2019, 58: 4466–4483
- 364 Yang D, Yang R, Zhang J, Yang Z, (Frank) Liu S, Li C. *Energy Environ Sci*, 2015, 8: 3208–3214
- 365 Yang D, Yang R, Ren X, Zhu X, Yang Z, Li C, Liu SF. *Adv Mater*, 2016, 28: 5206–5213
- 366 Feng J, Zhu X, Yang Z, Zhang X, Niu J, Wang Z, Zuo S, Priya S, Liu SF, Yang D. *Adv Mater*, 2018, 30: 1801418
- 367 Yang L, Feng J, Liu Z, Duan Y, Zhan S, Yang S, He K, Li Y, Zhou Y, Yuan N, Ding J, Liu SF. *Adv Mater*, 2022, 34: 2201681
- 368 Dou B, Miller EM, Christians JA, Sanehira EM, Klein TR, Barnes FS, Shaheen SE, Garner SM, Ghosh S, Mallick A, Basak D, van Hest MFAM. *J Phys Chem Lett*, 2017, 8: 4960–4966
- 369 Pisoni S, Fu F, Widmer R, Carron R, Moser T, Groening O, Tiwari AN, Buecheler S. *Nano Energy*, 2018, 49: 300–307
- 370 Bae JW, Lee SW, Yeom GY. *J Electrochem Soc*, 2007, 154: D34
- 371 Xu Y, Lin Z, Wei W, Hao Y, Liu S, Ouyang J, Chang J. *Nano-Micro Lett*, 2022, 14: 117
- 372 Yang L, Xiong Q, Li Y, Gao P, Xu B, Lin H, Li X, Miyasaka T. *J Mater Chem A*, 2021, 9: 1574–1582
- 373 Yang L, Li Y, Wang L, Pei Y, Wang Z, Zhang Y, Lin H, Li X. *ACS Appl Mater Interfaces*, 2020, 12: 22992–23001
- 374 Cho E, Kim YY, Ham DS, Lee JH, Park JS, Seo J, Lee SJ. *Nano Energy*, 2021, 82: 105737
- 375 Dkhissi Y, Huang F, Rubanov S, Xiao M, Bach U, Spiccia L, Caruso RA, Cheng YB. *J Power Sources*, 2015, 278: 325–331
- 376 Poorkazem K, Liu D, Kelly TL. *J Mater Chem A*, 2015, 3: 9241–9248
- 377 Hu X, Huang Z, Zhou X, Li P, Wang Y, Huang Z, Su M, Ren W, Li F, Li M, Chen Y, Song Y. *Adv Mater*, 2017, 29: 1703236
- 378 Yoon J, Sung H, Lee G, Cho W, Ahn N, Jung HS, Choi M. *Energy Environ Sci*, 2017, 10: 337–345
- 379 Dong H, Wu Z, Jiang Y, Liu W, Li X, Jiao B, Abbas W, Hou X. *ACS Appl Mater Interfaces*, 2016, 8: 31212–31221
- 380 Yang D, Zhang X, Hou Y, Wang K, Ye T, Yoon J, Wu C, Sanghadasa M, Liu SF, Priya S. *Nano Energy*, 2021, 84: 105934
- 381 Roldán-Carmona C, Malinkiewicz O, Soriano A, Mínguez Espallargas G, Garcia A, Reinecke P, Kroyer T, Dar MI, Nazeeruddin MK, Bolink HJ. *Energy Environ Sci*, 2014, 7: 994
- 382 Xu M, Feng J, Fan ZJ, Ou XL, Zhang ZY, Wang HY, Sun HB. *Sol Energy Mater Sol Cells*, 2017, 169: 8–12
- 383 Han GS, Lee S, Duff ML, Qin F, Lee JK. *ACS Appl Mater Interfaces*, 2018, 10: 4697–4704
- 384 Abdollahi Nejand B, Nazari P, Gharibzadeh S, Ahmadi V, Moshaii A. *Chem Commun*, 2017, 53: 747–750
- 385 Yoon J, Hou Y, Knoepfel AM, Yang D, Ye T, Zheng L, Yennawar N, Sanghadasa M, Priya S, Wang K. *Chem Soc Rev*, 2021, 50: 12915–12984
- 386 Qiu L, Deng J, Lu X, Yang Z, Peng H. *Angew Chem Int Ed*, 2014, 53: 10425–10428
- 387 Hu H, Yan K, Peng M, Yu X, Chen S, Chen B, Dong B, Gao X, Zou D. *J Mater Chem A*, 2016, 4: 3901–3906
- 388 Li R, Xiang X, Tong X, Zou J, Li Q. *Adv Mater*, 2015, 27: 3831–3835
- 389 Luo D, Su R, Zhang W, Gong Q, Zhu R. *Nat Rev Mater*, 2019, 5: 44–60
- 390 Wu J, Chen P, Xu H, Yu M, Li L, Yan H, Huangfu Y, Xiao Y, Yang X, Zhao L, Wang W, Gong Q, Zhu R. *Sci China Mater*, 2022, 65: 2319–2324
- 391 Zhang J, Zhang W, Cheng HM, Silva SRP. *Mater Today*, 2020, 39: 66–88
- 392 Lang F, Nickel NH, Bundesmann J, Seidel S, Denker A, Albrecht S, Brus VV, Rappich J, Rech B, Landi G, Neitzert HC. *Adv Mater*, 2016, 28: 8726–8731
- 393 Mukherjee B, Wu X, Maczka T, Kwan T, Huang Y, Mares V. *Radiat Measurements*, 2016, 94: 65–72
- 394 Miyazawa Y, Ikegami M, Chen HW, Ohshima T, Imaizumi M, Hirose K, Miyasaka T. *iScience*, 2018, 2: 148–155
- 395 Romano V, Agresti A, Verduci R, D'Angelo G. *ACS Energy Lett*, 2022, 7: 2490–2514
- 396 Markvart T. *J Mater Sci-Mater Electron*, 1990, 1: 1–12
- 397 Wei H, DeSantis D, Wei W, Deng Y, Guo D, Savenije TJ, Cao L, Huang J. *Nat Mater*, 2017, 16: 826–833
- 398 Yang S, Xu Z, Xue S, Kandlakunta P, Cao L, Huang J. *Adv Mater*, 2019, 31: 1805547
- 399 Tu Y, Wu J, Xu G, Yang X, Cai R, Gong Q, Zhu R, Huang W. *Adv Mater*, 2021, 33: 2006545
- 400 Cardinaletti I, Vangerven T, Nagels S, Cornelissen R, Schreurs D, Hruby J, Vodnik J, Devisscher D, Kesters J, D'Haen J, Franquet A, Spampinato V, Conard T, Maes W, Deferme W, Manca JV. *Sol Energy Mater Sol Cells*, 2018, 182: 121–127
- 401 Tu YG, Xu GN, Yang XY, Zhang YF, Li ZJ, Su R, Luo DY, Yang WQ, Miao Y, Cai R, Jiang LH, Du XW, Yang YC, Liu QS, Gao Y, Zhao S, Huang W, Gong QH, Zhu R. *Sci China-Phys Mech Astron*, 2019, 62: 974221
- 402 Reb LK, Böhmer M, Predeschly B, Grott S, Weindl CL, Ivandekic GI, Guo R, Dreißigacker C, Gernhäuser R, Meyer A, Müller-Buschbaum P. *Joule*, 2020, 4: 1880–1892
- 403 <https://www.nrel.gov/news/features/2021/space-mission-tests-nrel-perovskite-solar-cells.html>
- 404 Peshek TJ, Crowley KM, Delmas W. On the Performance of MAPbI₃ in the Space Environment. In: *2021 IEEE 48th Photovoltaic Specialists Conference (PVSC)*, 2021. 2611–2613

- 405 <https://green-innovation.nedo.go.jp/en/project/next-generation-solar-cells/>
- 406 Green MA, Hishikawa Y, Dunlop ED, Levi DH, Hohl-Ebinger J, Ho-Baillie AWY. *Prog Photovolt Res Appl*, 2018, 26: 427–436
- 407 <https://www.global.toshiba/ww/technology/corporate/rdc/rd/topics/21/2109-01.html>
- 408 https://www.sekisuichemical.com/news/2022/1378100_38754.html
- 409 <http://www.gcl-perovskite.com/wm/>
- 410 <http://www.microquanta.com/newsinfo/49C5473D122A12B7/>
- 411 <http://utmolight.com/20492/117028.html>
- 412 http://www.wondersolar.cn/cn/nd.jsp?id=13#_np=175_2492
- 413 <https://www.oxfordpv.com/news/oxford-pv-hits-new-world-record-solar-cell>
- 414 <https://www.pv-magazine.com/2021/07/23/oxford-pv-completes-100-mw-factory-build-out/>
- 415 <https://sauletech.com/launching-production-line/>
- 416 <https://www.solliance.eu/2021/two-world-records-for-4t-perovskite-tandem/>
- 417 <https://www.solliance.eu/2021/tandem-breakthrough-by-solliance-partners/>
- 418 <https://www.specific.eu.com/>
- 419 <https://www.pv-magazine.com/2022/07/19/zsw-tubesolar-achieve-14-efficiency-for-thin-film-agrivoltaic-solar-tubes/>
- 420 <https://www.evolarab.se/>
- 421 <https://businessfacilities.com/2022/06/solar-rd-projects-part-of-u-s-investment-in-clean-energy-industry/>
- 422 <https://enmatcorp.com/high-speed-inline-roll-to-roll-module-production/>
- 423 <https://www.uni-test.com/en/energy/perovskite.php>
- 424 https://www.hanwha.com/en/news_and_media/stories/sustainability/plugging-into-the-sun-how-hanwha-is-leading-with-innovations-in-solar-energy.html
- 425 Cai M, Wu Y, Chen H, Yang X, Qiang Y, Han L. *Adv Sci*, 2017, 4: 1600269
- 426 Pescetelli S, Agresti A, Viskadourous G, Razza S, Rogdakis K, Kallogerakis I, Spiliarotis E, Leonardi E, Mariani P, Sorbello L, Pierro M, Cornaro C, Bellani S, Najafi L, Martín-García B, Del Río Castillo AE, Oropesa-Núñez R, Prato M, Maranghi S, Parisi ML, Sinicropi A, Basosi R, Bonaccorso F, Kymakis E, Di Carlo A. *Nat Energy*, 2022, 7: 597–607